

**PROCESS PARAMETERS AND MECHANICAL
PROPERTIES OF GEOPOLYMER GLASS FOAM
STRUCTURES**

**A Thesis Submitted to the
Graduate School of
İzmir Institute of Technology
in Partial Fulfilment of the Requirements for the Degree of**

MASTER OF SCIENCE

in Mechanical Engineering

**by
Dilan POLAT**

**December 2020
İZMİR**

ACKNOWLEDGMENTS

I would like to thank my thesis advisor, Prof. Mustafa GÜDEN, for his useful comments, constant support, patience and guidance through the learning and writing process of my master thesis.

I would like to thank to members of DTM-Lab and IYTE-MAM for their helps. In addition, I wish to express my thankfulness to my friend Res. Assist. Seçkin MARTİN for his help, support and patience during my studies.

Finally, I must express my very profound gratitude to my mother Özlem TOSUN and sister Öykü İrem POLAT for providing me with unfailing support and continuous encouragement through the process of researching and writing this thesis. This accomplishment would not have been possible without them.

ABSTRACT

PROCESS PARAMETERS AND MECHANICAL PROPERTIES OF GEOPOLYMER GLASS FOAM STRUCTURES

The effects of waste-glass powder particle size (23 and 72 μm), solid/liquid ratio (S/L=1, 1.5 and 2) and aluminum foaming agent content (2-20 wt%) on the expansion behaviour of geopolymer slurries were investigated experimentally. Geopolymer slurries were prepared using an activation solution of NaOH (8M) and sodium silicate (10% NaOH, 27% SiO_2). The expansions and temperatures of the slurries were measured in-situ using a laser distance meter and a thermocouple, respectively. Few geopolymer foams were sintered at 600, 700, 725 and 750 $^\circ\text{C}$. The compression strengths and thermal conductivities of foam samples were also determined. The expansion of slurries continued until the temperature increased to 85-90 $^\circ\text{C}$. At this temperature, the slurry evaporation; hence, increased S/L ratio limited both the hydrogen release rate and geopolymerization reaction. As the content of Al increased, the final foam density decreased, while the coarse powder slurries resulted in lower densities (240-530 kg m^{-3}) than the fine powder slurries (280-530 kg m^{-3}). Three crystal phases, muscovite, sodium aluminum silicate hydrate and thermonitrite, were determined after the geopolymerization. The muscovite formation was noted to be favoured at higher S/L ratios. The partial melting of glass particles started after ~ 700 $^\circ\text{C}$, while sintering above this temperature decreased the final density. The reduced density above 700 $^\circ\text{C}$ was ascribed to the release of carbon dioxide by the decomposition of thermonitrite. Both the compressive strength and thermal conductivity of geopolymer and sintered foams increased at increasing densities and were shown to be comparable with those of previously investigated geopolymer and glass foams. The geopolymer foams sintered at 750 $^\circ\text{C}$ exhibited the lowest density and the highest compressive strength.

ÖZET

GEOPOLİMER CAM KÖPÜKLERİN PROSES PARAMETRELERİ VE MEKANİK ÖZELLİKLERİ

Atık cam toz parçacık boyutunun (23-72 μm), katı/sıvı oranının (K/S=1, 1.5, 2) ve alüminyum köpükleştirici madde miktarının (ağırlıkça %2-20), jeopolimer harçların genişleme davranışına etkisi deneysel olarak incelenmiştir. Jeopolimer harçlar, NaOH (8M) ve sodyum silikat çözeltisini (%10 NaOH, %27 SiO₂) içeren aktifleştirme çözeltisi kullanılarak hazırlandı. Harçların doğrusal genişmeleri ve sıcaklıkları, sırasıyla lazer mesafe ölçer ve termokupl kullanılarak anlık olarak ölçüldü. Bazı jeopolimer köpükler 600, 700, 725 ve 750 °C'de sinterlendi. Ayrıca köpük numunelerin basma dayanımları ve ısı iletkenlikleri belirlendi. Harçların doğrusal genişmesi, sıcaklık 85-90 °C'ye yükselene kadar devam etti. Bu sıcaklıkta gerçekleşen harçtaki buharlaşma ve artan K/S oranı, hem hidrojen gaz salım oranını hem de jeopolimerizasyon reaksiyonunu sınırlamıştır. Al toz miktarı arttıkça, jeopolimer köpüklerin nihai yoğunluğu azalırken, iri toz içeren harçlar (240 ve 530 kg m⁻³), ince toz içeren harçlardan (280 ve 530 kg m⁻³) daha düşük nihai yoğunluklara sahip oldu. Jeopolimerizasyon reaksiyonundan sonra üç kristal faz ki onlar muskovit, sodyum alüminyum silikat hidrat ve termonitrit yapı içinde belirlenmiştir. Yüksek K/S oranlarının muskovit fazının oluşumunun lehine bir etkisi olduğu tespit edildi. Cam parçacıklarının kısmi erimesi, yaklaşık 700 °C'den sonra başlarken, bu sıcaklığın üzerinde gerçekleştirilen sinterleme nihai yoğunluğu düşürmüştür. 700 °C'nin üzerinde görülen yoğunluk azalması, termonitritin ayrışmasıyla meydana gelen karbondioksit gazının salınmasına yorulmuştur. Jeopolimer ve sinterlenmiş köpüklerin hem basma dayanımı hem de ısı iletkenliği, yoğunluğun artmasıyla artmıştır bunun yanı sıra daha önce araştırılan jeopolimer ve cam köpükler ile kıyaslanabilir değerde olduğu gösterilmiştir. 750 °C'de sinterlenen jeopolimer köpükler, en düşük yoğunluğu ve en yüksek basma dayanımını göstermiştir.

TABLE OF CONTENTS

LIST OF FIGURES	vi
LIST OF TABLES	x
CHAPTER 1 INTRODUCTION	1
CHAPTER 2 LITERATURE REVIEW	3
2.1. Glass Foam	3
2.2. Geopolymer	6
2.3. Geopolymer Cement and Concrete	8
2.4. Geopolymer Foam	10
2.5. Mechanism of Al-based Geopolymer Foaming	11
2.6. Motivation of Thesis	16
CHAPTER 3 EXPERIMENTAL DETAILS	17
3.1. Materials	17
3.2. Preparation of Slurry and Foaming	19
3.3. Microstructure Characterization	22
3.4. Thermal Conductivity Tests	22
3.5. Compression Tests	23
CHAPTER 4 RESULTS	25
4.1. Powder Characterization	25
4.2. Slurry Expansions	27
4.3. Compression Tests	34
4.4. Thermal Conductivity	42
4.5. XRD and FTIR Analysis	43
4.6. Microscopic Analysis	48
CHAPTER 5 DISCUSSIONS	55
5.1. The Expansion of Slurries	55
5.2. Compressive Strength	61
5.3. Thermal Conductivity	65
5.4. XRD and FTIR Analysis	66
CHAPTER 6 CONCLUSIONS	69
9.1 Recommendations of Future Studies	70
REFERENCES	72

LIST OF FIGURES

<u>Figure</u>	<u>Page</u>
Figure 2.1. The applications of glass foams: (a) plates for insulation and (b) aggregates for road filling	3
Figure 2.2. The schematics of the glass foam production methods (a) vacuum method with molten glass, (b) vacuum method with SiC powder and molten glass, (c) heating glass and SiC powder, and (d) heating glass, diatom and CaCO ₃ powder.....	5
Figure 2.3. Three network forms of geopolymer.....	7
Figure 2.4. Schematic representation of geopolymerization process	7
Figure 2.5. Hydrogen evolution rate of a 0.2 g Al powder (atomized aluminum powder) 200 ml 1M NaOH solution at 25 °C and powder coding used in.....	13
Figure 2.6. Time evolution of the temperature and pH of the NaOH aqueous solution, the accumulated volume and the generation rate of hydrogen	14
Figure 2.7. Time dependent hydrogen generation giving with different NaOH/Al molar ratio	14
Figure 3.1. The pictures of the filtrates of NaOH and Al powder solution	18
Figure 3.2. The schematic of experimental methods used to prepare geopolymer glass foams	19
Figure 3.3. The expansion and temperature measurement set-up.....	21
Figure 3.4. The picture of a foam sample for thermal conductivity measurement.....	23
Figure 3.5. The top and side pictures of a foamed cylinder and foam compression test samples prepared using coarse powder with a S/L ratio of 2 at different aluminum contents.....	24
Figure 4.1 (a) SEM picture of glass powder and (b) optical micrograph of the mounted and polished cross-section of Al powder.....	26
Figure 4.2. The XRD pattern of (a) waste glass and (b) aluminum powder.....	26
Figure 4.3. The representative expansion-time and temperature-time curves of slurries and the pictures of expanding slurries at various times.....	27

<u>Figure</u>	<u>Page</u>
Figure 4.4. The representative expansion-time and temperature-time curves of fine glass powder slurries with the S/L=1 at increasing wt% of Al	29
Figure 4.5. The representative expansion-time and temperature-time curves of coarse glass powder slurries with the S/L=1 at increasing wt% of Al	29
Figure 4.6. The representative expansion-time and temperature-time curves of coarse glass powder slurries with the S/L=1.5 at increasing wt% of Al	30
Figure 4.7. The representative expansion-time and temperature-time curves of coarse glass powder slurries with the S/L=2 at increasing wt% of Al	30
Figure 4.8. The variation of (a) the maximum expansion and temperature and (b) the foam density with wt% of Al in the fine and coarse powder slurries with the S/L ratio of 1	32
Figure 4.9. The variation of (a) the maximum expansion, (b) temperature and (c) density with wt% of Al in the coarse powder slurries with the S/L ratios of 1, 1.5 and 2	34
Figure 4.10. The compressive stress-strain curves of the foam samples of fine powder slurries with the S/L=2 at (a) 2 wt% Al and S/L=1 at (b)12, (b) 16 and (d)20 wt% Al.....	36
Figure 4.11. The compressive stress-strain curves of foam samples of fine powder slurries with 2 wt% Al and S/L ratio (a) 1, (b) 2 and (c) 1.5.....	38
Figure 4.12. The compressive stress-strain curves of foam samples of fine powder slurries with 8 wt% Al and S/L ratio (a) 1, (b) 2 and (c) 1.5.....	39
Figure 4.13. The representative compressive stress-strain curves of geopolymers glass foam samples sintered at different temperatures	40
Figure 4.14. Compressive strength versus density of foams	41
Figure 4.15. The pictures of deformed foam samples of coarse powder slurry at 2 wt% Al and the S/L of (a) 2, (b) 1.5 and (c) 1 and (d) the fine powder slurry at 12 wt% Al and the S/L=1	42
Figure 4.16. The XRD pattern of geopolymers glass foam samples (a) S/L=1, (b) S/L=1.5 and (c) S/L=2 and (d) sintered geopolymers foams.....	46
Figure 4.17. The FTIR of geopolymers glass foam samples (a) S/L=1, (b) S/L=1.5 and (c) S/L=2	47

<u>Figure</u>	<u>Page</u>
Figure 4.18. The FTIR of sintered geopolymer glass foam samples	48
Figure 4.19. The SEM micrographs of the polished geopolymer glass foam samples with 2 wt% Al addition and the S/L ratio of (a) and (b) 1 and (c) and (d) 2 at different magnifications.	49
Figure 4.20. The SEM images of polished geopolymer glass foam samples with 2 wt% Al and S/L ratio (a) 1 and (b) 2	50
Figure 4.21. The results of EDX Line Scan Analysis of the foams samples with 2 wt% Al and the S/L ratio of (a) 1 and (b) 2.....	51
Figure 4.22. The SEM images of geopolymer glass foams' fracture surface with 2 wt% Al and S/L ratio 1.5: the magnification (a) 100x, (b)1000x, (c)5000x and (d)10000X and S/L ratio 2 at e)100x, (f) 1000x, (g) 5000x and (h) 10000x.....	52
Figure 4.23. The SEM image of fracture surface of geopolymer glass foams sintered at (a) and (b) 600, (c) and (d) 700, (e) and (f) 725, and (g) and (h) 750 °C in 100x and 1000x magnification, respectively.	53
Figure 4.24. The SEM images of the fracture surfaces of geopolymer glass foams sintered at (a) 600, (b) 700, (c) 725, and (d) 750 °C in 10000x magnification.....	54
Figure 5.1. (a) Typical expansion-time and temperature-time curves of geopolymer slurries and (b) time to maximum temperature and maximum temperature	58
Figure 5.2. The image of geopolymer foam cells after sintering.....	60
Figure 5.3. The images of sintered geopolymer foams at different temperature (a) top, (b) side, (c) bottom and (d) magnified image showing cell structure	61
Figure 5.4. The cubic closed cell foam structure showing the fracture sides on the cell edge and the geometry of the cross-section of a tetrakaidecahedral cell edge with plateau borders.	62
Figure 5.5. The variations of the compressive strength with the density for (a) present study and (b) the previous glass foam study and present study.....	64

<u>Figure</u>	<u>Page</u>
Figure 5.6. The variations of the compressive strengths of geopolymer and sintered foams and the compressive strength of previously investigated glass foams	65
Figure 5.7. The variations of the thermal conductivity with the density of the geopolymer glass foams of previous and present study	66



LIST OF TABLES

<u>Table</u>	<u>Page</u>
Table 2.1. Foaming agents for geopolymerization and their decomposition reactions	11
Table 3.1. Al powders investigated for the reaction in NaOH solution and the resulting reaction time and weight of residue	17
Table 3.2. The mixture proportion of geopolymer slurries.....	20
Table 4.1. The composition of glass powder	25
Table 4.2 The mean compressive strength for the groups all produced geopolymer and sintered geopolymer foams according to density.....	41
Table 4.3. The thermal conductivities and the corresponding densities of foam and sintered foams samples with 2 wt% Al addition.....	43

CHAPTER 1

INTRODUCTION

The world's energy need is increasing in each year proportional to the population growth. The energy need is estimated to grow by 40% until 2030. A significant proportion of the current energy supply is from non-renewable fossils, causing large amounts of CO₂ emission¹. This naturally poses a big pressure and threat on the planet. A substantial portion of the world's total energy, about 30-40%, is further consumed by a single sector, the construction industry. Furthermore, the proportion of energy demand in the construction industry is expected to raise 58% by 2050².

Portland cement-based concrete has been among the most produced materials since 1900^{3,4}. Limestone is used as a raw material in the Ordinary Portland Cement (OPC)⁵ and limestone itself causes large amount of CO₂ emission during the concrete production⁴. Within 25-50 years, limestone is likely to be totally consumed⁵. To reduce both energy consumption and CO₂ emission, the uses of raw materials requiring less energy and environmentally friendly production routes are of great importance. Furthermore, the covering the buildings with thermal insulation materials can be an effective solution to minimize heating and cooling energy, not only in terms of the energy used during production but also in terms of the efficiency of the energy currently consumed^{1,2}.

Geopolymer foams are considered as an alternative for the traditional insulating materials². The properties of geopolymer foams can be listed as high thermal and fire resistance⁶, low shrinkage, low permeability coefficient⁷, high compressive strength, durability, low thermal conductivity, good chemical resistance, and good aging feature⁸. They are conventionally processed using silica and alumina containing cheap, abundant raw materials. The geopolymer reaction that bounds the granular raw materials by a solid, strong network of bonding takes place between alumina and silica at room temperature, eliminating any need for a high-temperature treatment step for consolidation. Waste and secondary sources of silica like waste glass (WG) and alumina or fly ash (FA) are appropriate raw materials for the geopolymerization reaction. As WG contains a large amount of cheap and disposable silica, it is a suitable starting material in geopolymer foam processing.

The aim of this thesis is to investigate this possibility of processing geopolymer glass foams using WG powder. An Al powder was used as a foaming agent and the oxide skin layer on the surface of Al powder was considered as an additional alumina source for the geopolymerization. The effects of the glass powder particle size, solid/liquid ratio, and Al powder content on the expansion behaviour of geopolymer slurries and the compression mechanical behaviour and thermal conductivities of foamed slurries were studied. Geopolymer foams were further sintered between 600 and 750 °C in order to investigate the possibility of forming a glass foam structure at temperatures lower than the foaming temperatures of conventional glass foams (750-950 °C). The compressive strengths and thermal conductivities of the geopolymer and sintered geopolymer foams were also compared with those published in the literature.



CHAPTER 2

LITERATURE REVIEW

2.1. Glass Foam

Glass foams are a group of low-density cellular structures, mainly made of silica. They have comparable compression strength, low thermal conductivity, high sound absorption and low moisture-holding capacity, high heat and freeze resistance, and long service life. Glass foams are non-flammable as opposite to polymer foams. The properties of glass foams make them very much suitable structures for the heat and sound insulations of buildings⁹. Currently, two forms are used widely. The plate form is for the heat and sound insulations of buildings and the aggregate form is preferred in filling roads or floors (Figures 2.1(a-b)).

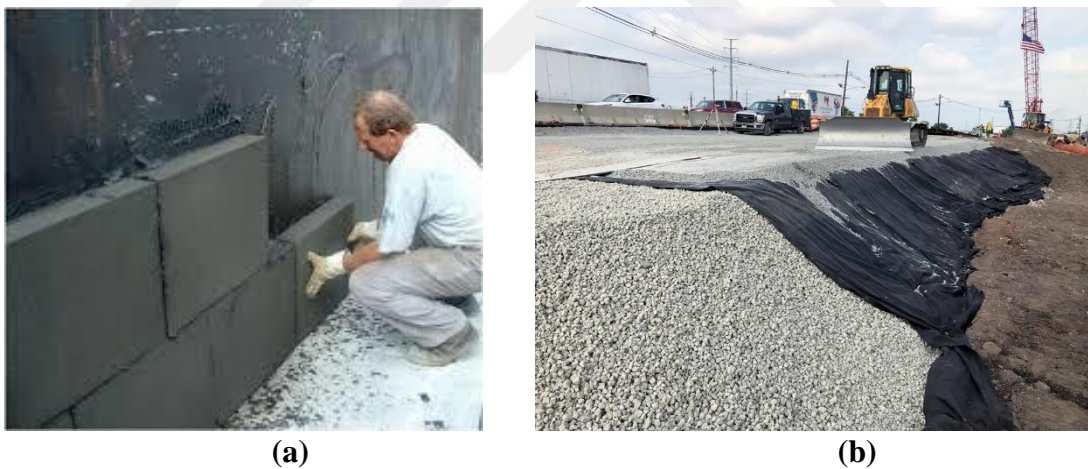


Figure 2.1. The applications of glass foams: (a) plates for insulation and (b) aggregates for road filling

The studies on the production of glass foams started in the 1930s. A glass foam product was patented by Long in 1934 along with a production method¹⁰. In this method, a mixture of raw materials containing alkali metal salts, silica and metal compounds was melted in a furnace, then quickly cooled down to 500-700 °C and kept at this temperature range for a certain period of time. The reduced gas solubility of the melt at a lower

temperature resulted in the evolution of gas that forms a cellular structure. However, the resultant cells were reported heterogeneous in size and distribution. Several different methods have been proposed and developed over the years in order to obtain glass foams with homogeneous cell size and distribution. Figures 2.2 (a-d) show the schematic presentations of various methods used for glass foam processing. In a method shown in Figure 2.2 (a), a molten glass containing dissolved air/gas is vacuumed to form gas bubbles ¹¹. The method results in heterogeneous cell size and distribution like the one patented by Long in 1934 ¹⁰. Adding and mixing a gas-forming powder (foaming agent) into molten glass e.g. SiC induces more homogeneous cell structure ¹². The reaction of SiC with the oxygen in the melt or oxygen in the air releases CO₂ gas, which expands the glass melt (Figure 2.2(b)). In another method, glass and foaming agent powders are mixed and pressed mechanically inside a mold. The pre-shaped mixture is then heated just above the softening temperature of the glass. Then, the partially molten glass body expands as CO₂ is released by the reaction of SiC with oxygen (Figure 2.2(c)). The glass foam is then annealed at an intermediate temperature followed by a cooling to room temperature ¹³. In a method shown in Figure 2.2(d), a silica-based powder having a porous structure itself such as vermiculite is mixed with glass powder and with a CaCO₃-foaming agent (Figure 2.2 (d)) ¹⁴. By the release of CO₂, the partially melt powder mixture expands to the final densities between 350 and 400 kg m⁻³. The porous powder remains intact and located at cell walls, providing additional porosity to glass foam. In this way, the final foam densities are further decreased. It was stated that when the diatomaceous earth powder (1-8 wt%) was mixed with a glass powder and a foaming agent (0.5-2 wt% CaCO₃), the final density of glass foam was reduced significantly ¹⁵.

Considering very large amount of bottles, windows, fluorescent and cathode-ray screens are recycled each year, the use of WG in glass foam production looks beneficial for the environment and also economical in terms of raw material cost. Therefore, the current glass foam production is largely based on the use of WG, WG and a foaming agent powder mixture is heated to a high temperature to form a cellular structure ¹⁶. The glass composition is generally made up of ~14% Na₂O and ~70% SiO₂. The glass foam are also produced using waste cathode-ray tubes having ~50-85 wt% of glass ^{17, 18} and fly ash ¹⁹⁻²¹.

Foaming glass power mixtures can be achieved by using two groups of foaming agents: neutralizers (e.g. CaCO₃ ^{17, 22, 23}, CaMg(CO₃)₂ ¹⁹, Na₂CO₃ ^{18, 24}, and MnO₂ ^{25, 26})

and redox agents (e.g. C²⁷, SiC²², Si₃N₄²⁸, AlN²⁸ and TiN²⁹). A neutralizer releases CO₂ and a redox agent releases either N₂ and CO₂ or N₂, when it is heated to an elevated temperature.

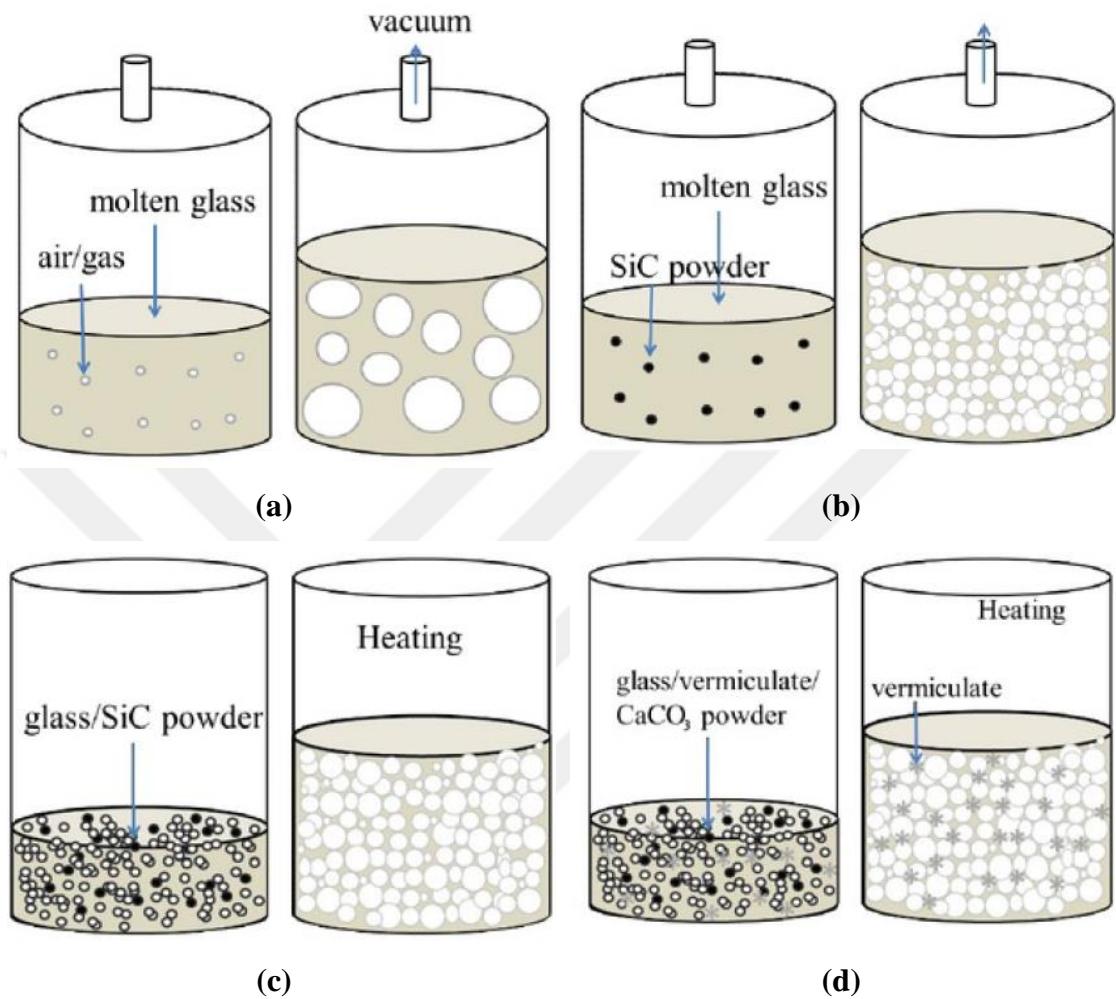


Figure 2.2. The schematics of the glass foam production methods (a) vacuum method with molten glass, (b) vacuum method with SiC powder and molten glass, (c) heating glass and SiC powder, and (d) heating glass, diatom and CaCO₃ powder.

(Source: Zeren, D., 2019)

The production cost of glass foams is higher than that of polymer foams and glass and stone wools²⁶. The major factor affecting the higher cost is the need for melting glass powder mixture at a relatively high temperature¹⁹. Soda-lime-silicate and cathode-ray-tube glasses are foamed at 750-950 °C using CaCO₃^{14, 19} and 950 °C using SiC as a foaming agent³¹. The use of CaCO₃ as a foaming agent is problematic as it reacts with glass melt at the surface, making the foaming process difficult to control^{17, 32, 33}. Glass foams are however environmentally friendly in the production and utilization³⁴; therefore, their market size has been steadily growing in all countries over the past two

decades ²⁶. According to the authors' investigation, there appeared approximately 170 scientific articles in Web of Science on glass foams; however, the total number of patents related to manufacturing was 390 until 2015, which implied the importance of the need for new methods.

2.2. Geopolymer

Geopolymer was discovered by the French scientist Joseph Davidovits in the 1970s ³⁵. It is a covalently bonded alumina-silicate compound, having an amorphous or semi-crystalline crystal structure, as similar to polymer chains and acts as a cement (binding the constituents) in concrete. Geopolymer is also referred as to inorganic polymer, inorganic polymer glass, alkali-bonded ceramic and hydro-ceramic ³⁶. Sialate (Si-O-Al) is the abbreviation name given to alumina-silicate geopolymer structure, formed by sharing of oxygen atoms by the tetrahedral structures of SiO_4 and AlO_4 ³⁵, whereas siloxo bond is composed of silicon to oxygen (Si-O-Si). Sialate may be in the poly(sialate), poly(sialate-siloxo), and poly(sialate-disiloxo) form depending on the Al/Si ratio as shown in Figure 2.3 ³⁷. Since the tetrahedral structures of SiO_4 and AlO_4 are negatively charged, positive ions such as Na^+ , K^+ , or H_3O^+ must be present in the structure for the electrical charge balance ³⁸. The formation of the 3D network of aluminosilicate oligomers by the polycondensation reaction is called geopolymerization, shown in Figure 2.4 ³⁹. The geopolymerization reaction binds the alkali activated raw materials having alumina and silica precursor ³⁵. Geopolymer can also be used as a resin in carbon fiber composites, monolithic refractory and thermal protection for wooden structures ³⁶. Geopolymer materials are alternative to thermoset polymers in various applications with their fire-resistant properties.

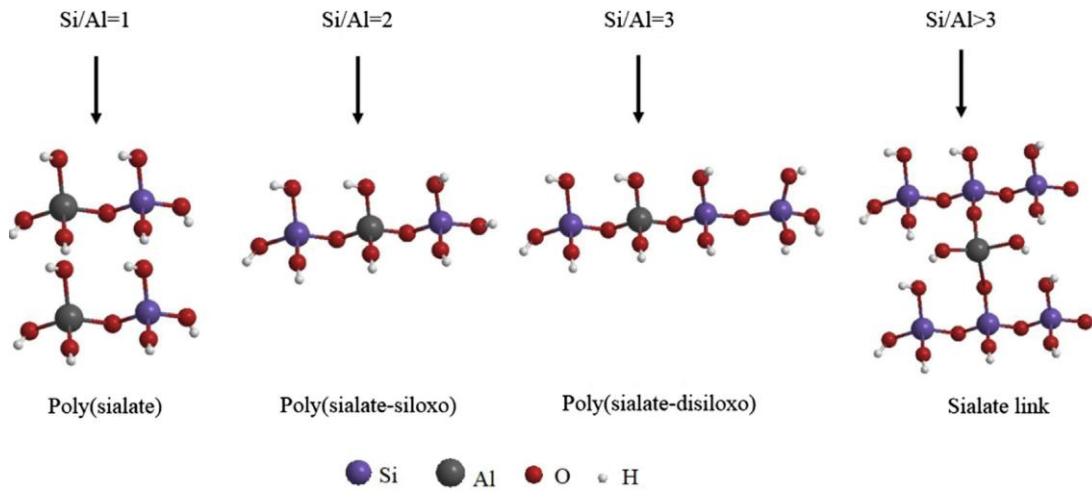


Figure 2.3. Three network forms of geopolimer
(Source: Zhuang et al., 2016)

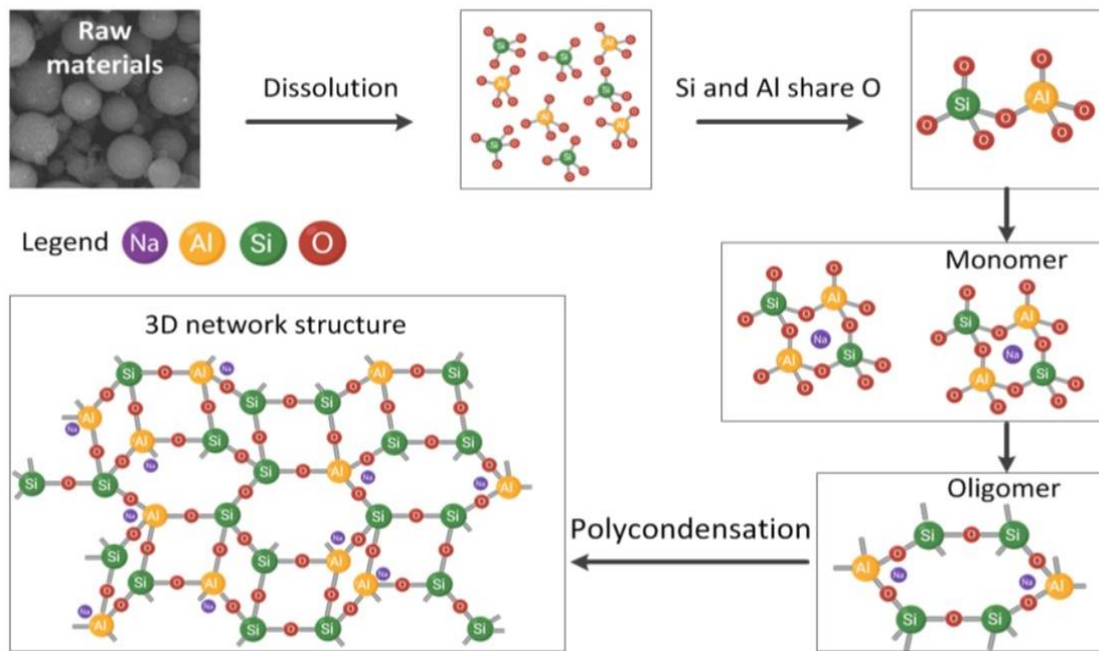


Figure 2.4. Schematic representation of geopolimerization process
(Source: Zhang et al., 2020)

2.3. Geopolymer Cement and Concrete

Silica and alumina are two main precursors for the synthesis of geopolymer cement. Fly ash ³⁹ (FA) and kaolin ³⁶ (KL) or metakaolin (MK) ³ are widely investigated sources of silica and alumina in geopolymer concrete. Moreover, a mixture of sodium hydroxide (NaOH) and sodium silicate (Na₂SiO₃) solution is used as an alkali activation solution for geopolymerization. NaOH acts as an accelerator and Na₂SiO₃ as an inhibitor. The kinetics of geopolymer reaction and the resulting structure are controlled by the ratio of NaOH and Na₂SiO₃ ^{40,41}. Mixing the above raw materials in correct proportions results in an exothermic geopolymerization reaction at room temperature ³⁵. After mixing raw materials, the geopolymer slurry is cured at a temperature usually below 100 °C to set geopolymer cement ³⁹. The geopolymerization reaction may be summarized in five steps as ³

- 1) The dissolution of aluminosilicate starting raw material in an alkaline environment
- 2) The formation of oligomer by the reaction of activator with Si
- 3) The geopolymer gel formation as a result of the supersaturation of the solution with Si
- 4) The growth of geopolymer gel by forming a solid bond with and surrounding insoluble aluminosilicate starting material
- 5) The change of geopolymer gel towards a more regular structure

Geopolymer cement is considered an alternative to OPC ⁴². It provides all necessary properties to concrete, causing less CO₂ emission and requiring less energy for concrete production. In addition, it has more accessible raw materials compared to OPC ³. In geopolymer concrete, the ingredients are rapidly settled by the in-situ formed geopolymer cement ³. Geopolymer concrete has good long-term properties ³⁶, good ability to immobilize toxic metals ³⁷, resistance to acid attacks and high temperature ³⁹, non-flammability ³⁶, and settled at room temperature ⁵. Geopolymer concrete has been used in various places including the nuclear sector, aeronautical engineering, archaeological research ³⁹, architectural sector ⁴³. It is also useful in the construction demanding fire-resistance such as bridges, precast applications including bricks, precast pipes, and slabs for paving ^{3, 5, 43}. Additive manufacturing has also become a preferred

subject in various fields since it produces near-net shaped structures without producing waste material ⁴⁴. Accordingly, efforts recently have been on the additive manufacturing of geopolymer structures ^{43, 44}. The production of 3D geopolymer structures using a powder bed system has been recently investigated ⁴³. The geopolymer was shaped by printing a binder on the powder bed; then, the geopolymer reaction was carried out by dipping the printed powder into an activator solution. In a final step, the printed structure was cured. In a study, 3D structures were created by extruding geopolymer mud with the help of a steel filament nozzle ⁴⁴. A similar method was further explored in another study ⁴⁵.

The use of waste streams instead of the raw materials such as MK and FA in geopolymer is of great importance in terms of saving environment, energy and natural resources ^{46, 47}. Waste glass in this regard has a potential because it contains a high concentration of silica, while alumina source may be needed separately ³⁸. More than 10 million tons of WG are produced annually in the USA alone and this may lead to a shortage in the storage space and disposal of WG ^{38, 47}. In this respect, the consumption of WG as a geopolymer raw material is important. In addition, WG addition was shown to have positive effects on the mechanical properties of geopolymer concrete ³⁸. Nevertheless, there have been only a few studies on the use of WG in geopolymer concrete processing.

In a study conducted in 2019, the use of different proportions of WG powder and FA as aluminosilicate sources were investigated ³⁸ with different concentrations of NaOH (0, 2.5, 5, 7.5, 10 M). The study also focused on the economic benefits of using WG and reported that the mechanical properties of the geopolymer were improved by the WG powder addition after about long curing times. A similar study was conducted in 2019 ⁴⁷. Different amounts of WG powder (0, 5, 10, and 20 wt%) were used together with MK as aluminosilicate sources. The prepared geopolymers were cured at room temperature and 60 °C. The mechanical properties of geopolymers were enhanced by introducing low percentages of glass powder and the glass powder addition further limited the drying shrinkage.

2.4. Geopolymer Foam

Lightweight concretes have many advantages over conventional concretes such as they provide more enhanced insulation properties, easier prefabrication, higher fire resistance, and more debatable construction cost, ⁴⁸. However, geopolymer foams are more preferred types among lightweight concretes since they are produced by a more controllable and energy saving synthesis method that significantly reduces CO₂ emission ^{48, 49}. The important properties of geopolymer foams include high thermal and fire resistance ⁶, low shrinkage, low permeability coefficient ⁷, high compressive strength, durability, low thermal conductivity, good chemical resistance, and good aging feature ⁸. The compressive strengths of geopolymer foams range 0.3-17 MPa and the thermal conductivities 0.15-1.65 W m⁻¹ K⁻¹ at a density range of 430-1800 kg m⁻³ ⁵⁰.

Geopolymer foams are used in different places, while civil engineering applications are among the top ⁸. There are preferred in buildings and bridge constructions due to their lightweight ⁶ and used as a void filling material to repair ⁷ and prevent heat losses of buildings ⁷. They are also used in non-structural construction applications ⁴⁹. Examples include cast-in-situ wall elements, slabs, facades, or as a core for porous sandwich structures ⁴⁹. In addition, they are preferred by chemical and nuclear industries due to their inert attitude towards chemicals ⁸. It can be used as a filter in separation processes, a heat exchanger or catalyst support ⁸, an acoustic absorbent for noise pollution ⁵¹ and a fire-resistance and an adsorbent coating on materials ⁵².

Geopolymer foams are prepared by using chemical and physical foaming, and alternative methods ⁵³. In the physical foaming or pre-foaming method, a large proportion of gas or air bubbles is added directly into a geopolymer slurry by a blowing agent ⁵⁴. Different blowing agents such as a surfactant ⁴⁹, glue resin, detergent, or hydrolyzed protein ⁵⁵ can be used. Then, the gas or air bubbles are distributed by mixing the slurry. These bubbles are thermodynamically unstable; therefore, their control is very difficult ⁵⁰. For this, physical foaming is generally not preferred⁴⁹. In another physical foaming method, sacrificial fillers such polymer fillers are added to geopolymer slurry and after geopolymerization they are removed by thermal or chemical treatment ⁵³. The use of fillers is a challenging considering economic and environmental factors ⁵³. The chemical foaming method uses various chemical foaming agents ³. The reaction of blowing agents with the alkaline medium in the geopolymer slurry creates H₂ gas, and the voids created

by this gas are trapped in the hardened body ^{3, 8, 53}. Hence, a porous structure is obtained. The voids have an irregular shape with an adequate number ⁴⁹. The investigated foaming agents include Al ^{2, 49, 51, 55}, Zn ⁶, silica fume ⁵², H₂O₂ ^{2, 8, 55} and NaOCl ⁵⁵.

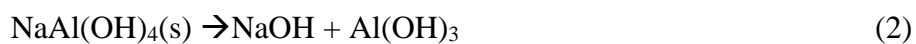
The decomposition reactions of different foaming agents produce different types of gases. The decomposition reactions of various foaming agents are tabulated in Table 2.1. The most commonly used foaming agents are H₂O₂ and Al powder. Although, the use of H₂O₂ induces larger sizes of pores, the pores are not evenly distributed in the structure ². More controllable pore size and pore size distribution are obtained by using Al powder ². Due to environmental and economic reasons, secondary aluminum has been recently investigated as a foaming agent and alumina source in geopolymer foam processing ⁵⁶.

Table 2.1. Foaming agents for geopolymerization and their decomposition reactions
(Source: Singh, N.B.J.M., 2018)

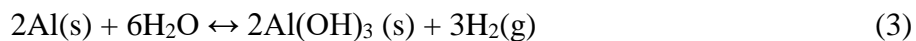
Foaming Agent	Decomposition Reaction
Al	$2\text{Al} + 6\text{H}_2\text{O} + 2\text{NaOH} \rightarrow 2\text{NaAl}(\text{OH})_4 + 3\text{H}_2^{(\text{g})}$ $2\text{NaAl}(\text{OH})_4 \rightarrow \text{NaOH} + \text{Al}(\text{OH})_3$ $2\text{Al} + 6\text{H}_2\text{O} \rightarrow 2\text{Al}(\text{OH})_3 + 3\text{H}_2^{(\text{g})}$
H ₂ O ₂	$\text{H}_2\text{O}_2 + \text{OH}^- \rightarrow \text{HO}_2^- + \text{H}_2\text{O}_{(\text{g})}$ $\text{HO}_2^- + \text{H}_2\text{O}_2 \rightarrow \text{H}_2\text{O}_{(\text{g})} + \text{O}_2 + \text{OH}^-$
NaOCl	$\text{NaOCl} \rightarrow \text{NaCl} + \frac{1}{2}\text{O}_2$ $2\text{NaOCl} + \text{C} \rightarrow 2\text{NaCl} + \text{CO}_2$
Silica Fume	$4\text{H}_2\text{O} + \text{Si} \rightarrow 2\text{H}_2 + \text{Si}(\text{OH})_4$

2.5. Mechanism of Al-based Geopolymer Foaming

The reactions of aluminum with NaOH solution are ⁵⁸



Reaction (1) consumes NaOH by producing H₂ gas. When sodium aluminate hydroxide concentration saturates, it dissociates into crystalline Al(OH)₃ precipitate and regenerates NaOH in the solution. The overall reaction of Al in NaOH solution is, therefore,

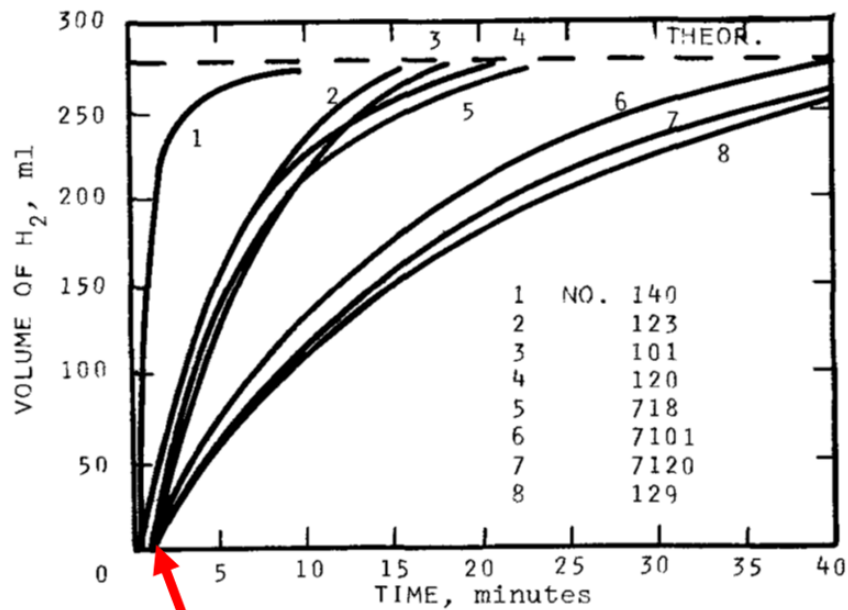


The rates of the first and second reaction can affect the rate of H₂ evolution. One gram of Al consumes 1.48 grams of NaOH in reaction 1. The stoichiometric ratio of NaOH/Al is therefore 1.48. A lower value of this ratio will result in a decrease in the rate of reaction 2 and H₂ evolution.

An early study on the reaction of Al with NaOH solution was conducted by Belitkus in 1970⁵⁸. The hydrogen evolutions of bulk and powder forms of different Al alloys were experimentally investigated in 0.1, 1 and 10M NaOH solutions. The rate of hydrogen evolution of the bulk form of Al was shown relatively slower than that of the powder form. Furthermore, the hydrogen evolution was shown more rapid in smaller size powder particles. The hydrogen evolution was completed in 10 min for 3-6 μm and 20 min for 17-20 μm powder particles in a 0.2 g Al powder 1M 200 ml NaOH solution (Figure 2.5). A delay in the start of the reaction was also reported and the delay increased with increasing particle size: 0.25 min for 3-6 μm and 3 min for 17-20 μm particles in a 0.2 g Al powder 200 ml 1M NaOH solution as marked by an arrow in Figure 2.5. The delay was shown to decrease with increasing the NaOH concentration. The reaction rate was further reported to depend on the density of Al powder pellets inserted into the solution: the lower was the pellet density; the higher was the hydrogen evolution. Finally, the importance of the stoichiometric amounts of Al and NaOH in the solution was emphasized for the rapid rate of the hydrogen evolution.

Hiraki et al.⁵⁹ investigated the hydrogen evolution of a waste Al powder (180-425 μm) in a 5M NaOH solution at different initial temperatures. The gas release rate was shown to increase monotonically until about 540 s, beyond this time the release rate decreased as depicted in Figure 2.6. Both the hydrogen evolution and temperature of the solution increased to maximum values until about the reaction was terminated, while the pH of the solution decreased and afterward increased slightly with increasing time as seen in Figure 2.6. The decrease in the pH of the solution was attributed to the formation of Al(OH)₄⁻ ions in the solution. The increased pH of the solution after about 1000 s was

reported due to the precipitation of $\text{Al}(\text{OH})_3$ (by the decomposition of $\text{Al}(\text{OH})_4^-$ ions which were also confirmed by XRD). The solution was filtered and XRD-analyzed. The analysis was shown the presence of $\text{Al}(\text{OH})_3$ crystal phase. The filtrate was then heated in a furnace to 473 K to remove water. The XRD analysis showed the Na_2AlO_2 phase, which was produced by the following reaction



NO	Powder designation	Nominal average particle diameter, μ
1	140	3-6
2	123	15-19
3	101	17-24
4	120	25-30
5	718	17-20
6	7101	17-24
7	7120	25-30
8	129	-

Figure 2.5. Hydrogen evolution rate of a 0.2 g Al powder (atomized aluminum powder) 200 ml 1M NaOH solution at 25 °C and powder coding used in (Source: Belitskus et al., 1970)

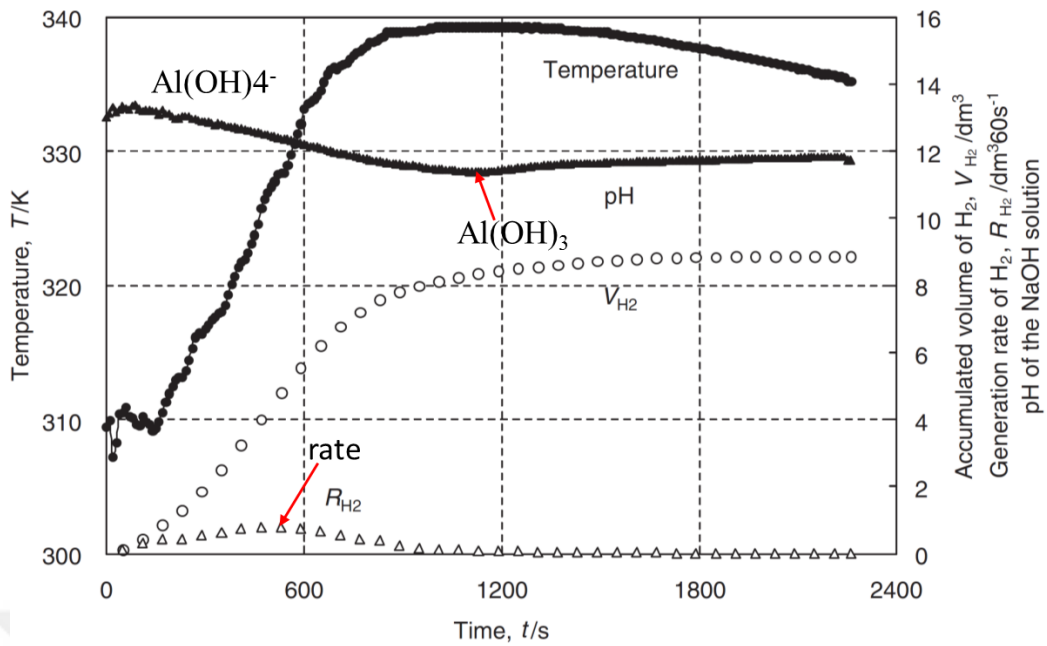


Figure 2.6. Time evolution of the temperature and pH of the NaOH aqueous solution, the accumulated volume and the generation rate of hydrogen (Source: Hiraki et al., 2005)

Martinez et al.⁶⁰ investigated the hydrogen evolution in NaOH solutions at varying NaOH/Al molar ratios, from 1.1 to 1.3. The reaction rate was tripled when the NaOH/Al molar ratio increased from 1.1 to 3 at 60 min as seen in Figure 2.7.

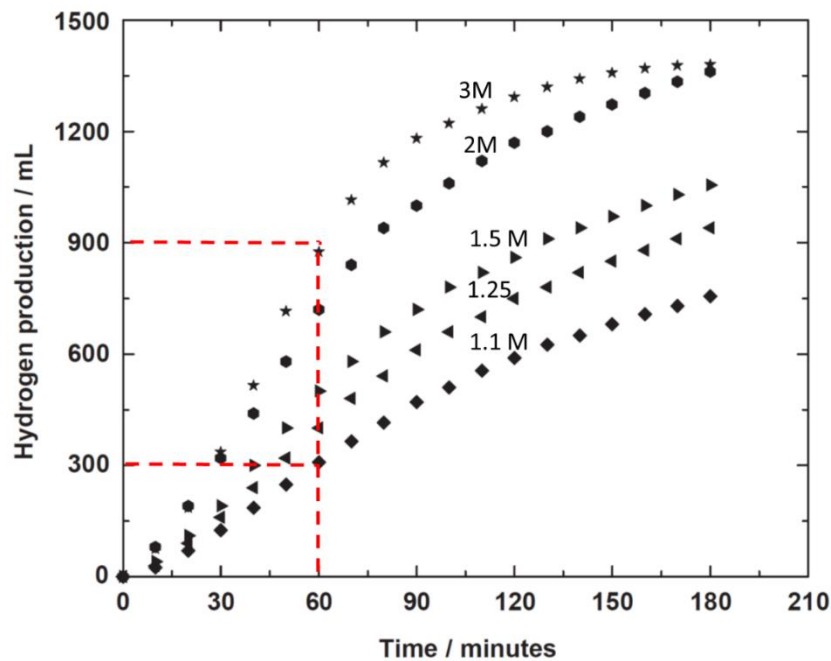


Figure 2.7. Time dependent hydrogen generation giving with different NaOH/Al molar ratio (Source: Martínez et al., 2005)

Hajimohammadi et al. ⁴⁸ prepared geopolymers using 70 wt% FA and 30 wt% NaOH solution without and with 1 wt% Al addition. The prepared geopolymers were characterized by XRD, FTIR, AFM and compression tests. Both samples with and without Al addition showed sodalite ($\text{Na}_8(\text{AlSiO}_4)_6(\text{OH})_2 4\text{H}_2\text{O}$) and thermonatrite ($\text{Na}_2\text{CO}_3 \cdot \text{H}_2\text{O}$) as main crystal phases. While the extent of thermonatrite formation was shown to decline in Al containing geopolymer. Thermonatrite formation was attributed to the atmospheric carbonation of sodium hydroxide and the increase of free alkali in the geopolymer matrix. It was concluded that the presence of Al prevented the extensive carbonation reaction in the geopolymer and increased the hydrogen evolution, leading to better gel connectivity and better compaction of geopolymer.

Bai et al. ⁶¹ investigated the geopolymer foam processing of a raw material containing a high proportion of soda-lime waste glass powder (75 wt% WG-25 wt% MK) using hydrogen peroxide as a foaming agent in 2019. Potassium hydroxide and potassium silicate were used as alkali activator. In addition to 3 wt% H_2O_2 , Triton X-100 was used as a stabilizing agent. The geopolymer slurry was kept at 75 °C for 7 minutes before pre-curing to speed up geopolymerization. Then the obtained wet geopolymer foam was cured at 75 °C for 7 days. The geopolymer foam obtained had a density of $\sim 0.92 \text{ g cm}^{-3}$, a compression strength of 7.3 MPa and thermal conductivity of $0.21 \text{ W m}^{-1} \text{ K}^{-1}$. The produced geopolymer foam samples were sintered at 700, 800 and 900 °C to obtain glass and glass-ceramic foams. The density of the foams decreased after sintering and open porosity was formed. When the sintering temperature increased from 700 to 900 °C, the density decreased from 0.48 g cm^{-3} to 0.27 g cm^{-3} and the compressive strength decreased from 5.5 MPa to 2.5 MPa.

Senff et al. ⁶² used a WG fibre from wind blade production as a reinforcement in a geopolymer foam. Aluminum powder was used as a foaming agent. The inclusion of glass fibre affected the mechanical properties positively and the aluminum powder was reported to have an effect on the physical characteristics of foams.

In a study published in 2019, Kastiukas et al. ⁷ investigated foaming a waste of tungsten mining and WG powder using Al powder. Tungsten mining waste contained 15 wt% Al_2O_3 . A mixture of NaOH and Na_2SiO_3 was used as an alkali activator. The effects of the ratio of Na_2O weight to tungsten mining waste and WG weight (3.1%, 3.3% and 3.5%) and the amount of Al (3, 6 and 9 wt%) on the final density and the compression strength of geopolymer foams were determined. The green foams were cured in a

humidity-controlled (95% humidity) oven between 40 and 100 °C for 24 hours. The ratio of the weight of the alkali activating solution to the weight of tungsten mining waste and WG powder was taken as 0.22. The density of foams did not change in heat treatment. The highest compression strength was found in the foams heat-treated at 80 °C. The effect of the percentage of Na₂O on the density of the foams was shown quite substantial; below 3.1% of Na₂O, no foaming occurred due to the absence of NaOH. The final density of foams decreased with increasing Al percentages. The final densities of foams prepared with 3.3 and 3.5% Na₂O solutions varied 500 to 700 kg m⁻³.

2.6. Motivation of Thesis

The literature review given above has proven an increasing number of investigations on the use of waste and secondary sources in geopolymer foam processing. This trend is mainly driven by both environmental and economic concerns. Waste glass is an abundant, cheap source of silicate. The aim of this thesis was therefore to investigate the possibility of the processing of geopolymer glass foams using WG powder. An Al powder produced by a melt spinning process in an open atmosphere was used as a foaming agent. The powder accommodated a thick oxide skin layer, which was considered as an additional alumina source for geopolymerization reaction. The effects of glass particle size, solid/liquid ratio and the content of Al powder on the expansion behaviour of geopolymer slurries and the compression mechanical behaviour and thermal conductivities of foamed slurries were studied. As stated earlier, glass foams were processed at relatively high temperatures, between 750-950 °C. Few geopolymer foams samples were therefore sintered at 600, 700, 725 and 750 °C in order to investigate the possibility of forming glass foams (out of geopolymer foams) at relatively lower temperatures. The compressive strengths and thermal conductivities of the geopolymer and sintered geopolymer foam samples were finally compared with those of the published in the literature.

CHAPTER 3

EXPERIMENTAL DETAILS

3.1. Materials

Waste glass powders were received in two different average particle sizes and used in the expansion/foaming experiments of geopolymer slurries. The first group of glass powder had an average particle size of 23 μm ($d_{50}= 22.733 \mu\text{m}$), which was a residue of a soda-lime window/flat glass polishing facility, Camex (Bursa, Turkey). The polishing in the facility was accomplished by using an oil-based coolant and the polishing residue was damped in a nearby field. The second group of WG powder had an average particle size of 72 μm and obtained from a local supplier in Turkey. The powder was supplied by a producer after crushing and grinding disposed bottles and window glasses. The first group of powder represented fine particle size and the second coarse particle size.

An aluminum powder was used as an alumina source and also as a foaming agent in the foaming experiments. Nevertheless, initial experiments were performed on Al powders with different particle sizes (Table 3.1) in order to determine the most appropriate powder type and size, which could react with NaOH solution at the slowest rate, leading to a controllable foaming process. In these experiments, one gram of aluminum powder was mixed with a 1M sodium hydroxide solution (NaOH- 97% pellet, ACS reagent, Sigma Aldrich). In the mixture, Al powder reacted with NaOH solution and released H_2 gas. When the gas-release terminated (determined by observing the solutions), the reaction was presumed to be completed.

Table 3.1. Al powders investigated for the reaction in NaOH solution and the resulting reaction time and weight of residue

Brand Name	Particle Size (μm)	Reaction Time (min.)	Residual Weight (mg)
Sigma Aldrich	<77	~20	12.4
Sigma Aldrich	-10+60	~25	10.6
Sigma Aldrich	<75	~20	12
Riedel-De Haén	Fine (~5)	~5	212.3
Industrial Powder	90	~60	17

After the termination of the H₂ evolution, the solutions were filtered using a 1 μm filter paper. The filtrates were then weighed to determine the residual weights after drying them in an oven at 100 °C. The residues had the colors of yellowish, brown hue and blackish as shown in Figure 3.1. The residues of the powders with -10+60 and 90 μm were in brown and blackish color, respectively.



Figure 3.1. The pictures of the filtrates of NaOH and Al powder solution

The reaction times and residual weights of the treated powders are further tabulated in Table 3.1. As is seen, an increase in particle size increases the reaction time. The highest residual weight is measured in the finest powder size, fine (~5 μm). This is followed by 90 μm powder with a residual weight of 17 g, while the rest of the powders have similar weights of residue. The foaming experiments were then decided to be continued by using an industrial-grade Al powder in 90 μm size since it results in the longest time for the reaction completion (60 min) and the cheapest one among others. This powder was produced through a melt spinning process in an open atmosphere.

In the foaming experiments of silicate solutions, Sigma Aldrich NaOH pellets of 97%, ACS reagent and Sigma Aldrich sodium silicate solution (Na₂SiO₃) with ~10.6% Na₂O and ~26.5% SiO₂ also called water glass were used as activators. A Sigma Aldrich carboxymethylcellulose (CMC) with an average molecular weight of ~90,000 was used as a binder to stabilize or modify the glass particles in the geopolymer foam structure.

3.2. Preparation of Slurry and Foaming

The geopolymer foam preparation steps are shown in Figure 3.2 and explained in detail below. However, before preparations, the amount of constituent raw materials corresponding to targeted weight percentages and S/L ratios were calculated.

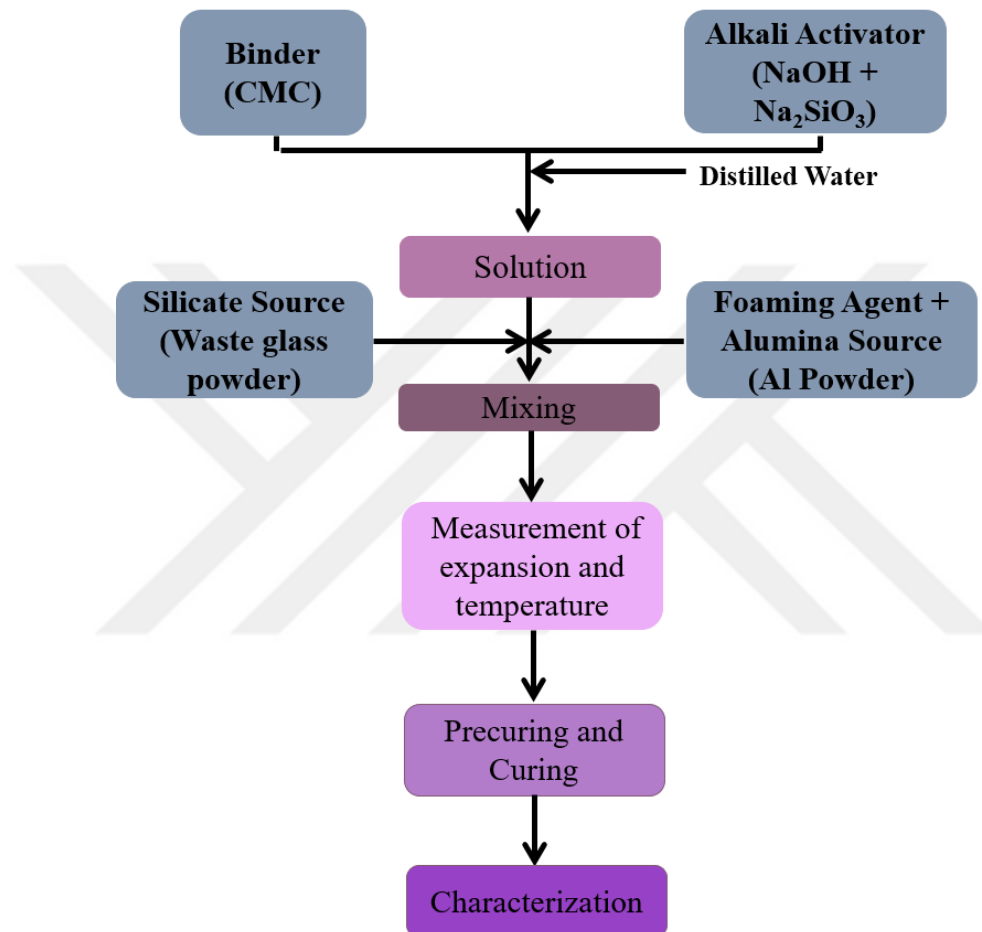


Figure 3.2. The schematic of experimental methods used to prepare geopolymer glass foams

Foamable slurry preparation started with solving carboxymethylcellulose, CMC (with an amount of 3 wt% of slurry) in distilled water at room temperature with the helping of a magnetic stirrer. Sodium hydroxide pellets with an amount that would give an 8M solution were then added into the CMC solution, while the solution was continuously mixed by the magnetic stirrer. Sodium silicate solution was then added to the solution with an amount that would give a solid to liquid (S/L) ratio of 1, 1.5, 2 and the solution was mixed with a high-speed mechanical mixer for one minute. In this study,

since the effects of NaOH and Na₂SiO₃ amounts on mechanical physical and chemical properties were not investigated, they were used at a fixed rate. For all solid-liquid ratios, the activation solution was prepared using the ratio Na₂SiO₃/NaOH=2.5 (gram/gram). Sequentially, appropriate amounts of glass powder and aluminum powder were then added to the solution and the slurry was mixed for 5 and 2 min again using a high-speed mechanical mixer, respectively. The prepared geopolymer slurry was then poured into a transparent Plexiglass foaming tube closed at the bottom, having a diameter of 73 mm and a height of 1500 mm. The slurry expanded inside the foaming tube and the expansion and the temperature of the slurry were measured in-situ. The slurry coding, S/L ratio, Al content and the particle size of the used glass powder are tabulated in Table 3.2.

Table 3.2. The mixture proportion of geopolymer slurries

Sample Name	S/L Ratio	Al Content (wt%)	NaOH/ Al (g- ratio)	Particle Size of Glass Powder (µm)
L0	1	2	5.287	72
L1	1	4	2.643	72
L2	1	8	1.321	72
N0	1.5	2	3.526	72
N1	1.5	4	1.762	72
N2	1.5	8	0.881	72
M0	2	2	2.643	72
M1	2	4	1.321	72
M2	2	8	0.660	72
S0	1	2	5.287	23
S1	1	4	2.643	23
S2	1	8	1.321	23
S3	1	12	0.881	23
S4	1	16	0.660	23
S5	1	20	0.528	23

Figure 3.3 shows the experimental set-up used to measure the expansions and temperatures of foaming slurries. A laser displacement sensor (Micro Epsilon ILR1030-8) clamped by a holder at a distance of 20 cm above the foaming tube was used to measure the expansions of the slurries in-situ as a function of time. The sensor was operated between 4 to 20 mA and calibrated before each experiment by determining the corresponding current difference of a known distance. The temperatures of foaming slurries were measured by using a K-type thermocouple. The simultaneous changes in the expansions and temperatures were then recorded by a Data Taker DT 80 data logger and

then the data were transferred to a computer. The percent volume expansion (V_E) or linear expansion was calculated using the following relation

$$V_E (\%) = \frac{h_f - h_i}{h_i} \times 100 \quad (3.1)$$

where, h_f and h_o are the final and initial height of the slurry, respectively.

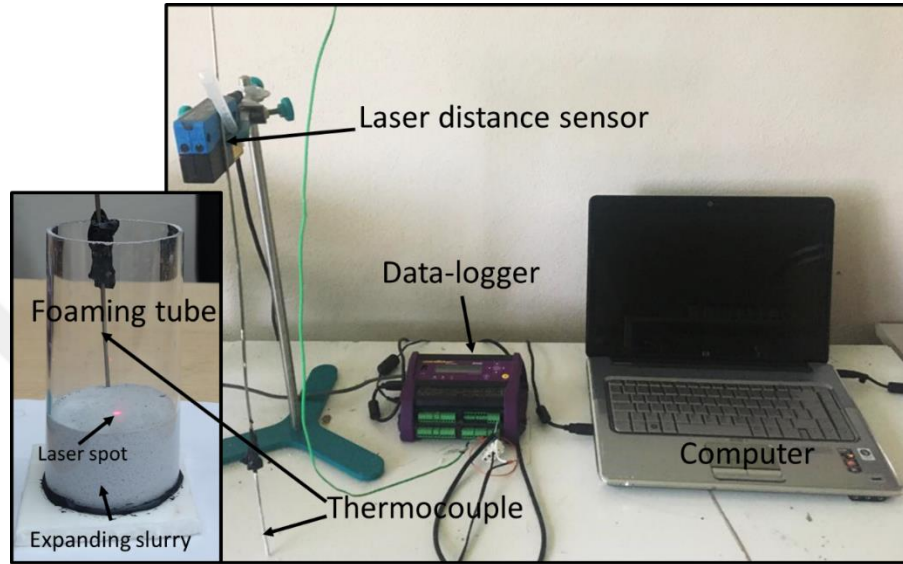


Figure 3.3. The expansion and temperature measurement set-up

The foamed slurries were kept at room temperature for 24 hours inside the foaming tube (pre-curing). The foams were then removed from the foaming tube and then cured in an oven at 60 °C for 24 hours. In order to examine the effect of sintering on the properties of produced geopolymer glass foams, only one or two samples were subjected to sintering at 600, 700, 725 and 750 °C for one hour in a Protherm Laboratory Furnace (Model PLF 130/5). The samples were furnace-cooled after sintering. The foam samples were heated with a heating rate of 10 °C min⁻¹ to the sintering temperature, kept at the sintering temperature for one hour and then furnace-cooled to room temperature.

Producing geopolymer glass foams, finally, was characterized in terms of micro- and nano-structural examination, mechanical and physical properties. Producing geopolymer glass foams, finally, was characterized in terms of micro and nano-structural examination, mechanical and physical properties. These examinations were fulfilled with the helping of X-Ray Diffractometer (XRD), Scanning Electron Microscopy (SEM), Fourier Transform Infrared Spectroscopy (FTIR), Compression Test Device, and Thermal Conductivity Test Device.

3.3. Microstructure Characterization

X-ray Diffraction (XRD) was used to determine the crystal structure of prepared foams. The samples for XRD were prepared by powdering the foam pieces in an agate. X-ray diffractometer analysis was performed in a Philips X'Pert Pro X-Ray Diffractometer using CuK α radiation (1.5418Å) at 40 kV from 5 to 80° with 0.05°/s scanning rate. XRD analysis was carried from 5 to 80° interval at a 0.05° s⁻¹ scanning rate. The elemental composition analysis of raw materials was performed using a Spectra IQ II X-Ray Fluorescence Spectrometer. The foam cellular structure and fracture surfaces were examined by an FEI QUANTA 250 FEG Scanning Electron Microscope (SEM) in Backscattered electron (BSED) mode using an Everhart-Thornley detector (ETD). The chemical compositions of the phases in foam samples were analyzed using an Energy Dispersive X-Ray (EDX) analyzer. ETD ensured high-resolution images from fracture surfaces and EDX provided information about point or regional chemical composition. Two types of samples were prepared for the SEM analysis. The first group was to examine the surface morphology; whereas, the second group to determine the chemical composition and phases. In the first group, the fractured foam pieces were directly observed under the SEM. In the second group, the foam samples were mounted in epoxy inside a mold. The mounted samples were then sequentially grinded using SiC grinding papers between 250 and 2400 mesh and polished using diamond solutions between 9 and 1 μ m. Molecular bond characterization and molecular structure were determined by using Fourier Transform Infrared Spectroscopy (FTIR). The analysis was made in a Digilab Excalibur Series Device with the ATR (Attenuated Total Reflectance) method. The spectra of transmittance were collected from 4000 to 600 cm⁻¹. The samples for FTIR were prepared by powdering the foam pieces in an agate.

3.4. Thermal Conductivity Tests

The thermal conductivities of foam samples were measured in a KEM QTM 500 thermal conductivity meter. This device takes measurements with the aid of a probe and is composed of a thermocouple and heater wire. It gives the heat at constant electrical energy and the temperature is increased exponentially. From the difference between the

temperature of the sample and the given temperature, thermal conductivity was calculated. Rectangular foam samples in 120x60x20 mm size were used for thermal conductivity measurements (Figure 3.4). Foam samples for thermal conductivity measurements were prepared separately. The foamable slurry was poured inside a rectangular plastic mold rather than a foaming tube. After curing and/or sintering, the top and bottom surfaces of these samples were grinded with sandpapers until surfaces were parallel and flat. The surfaces of specimens were cleaned after grinding by using compressed air. The thermal conductivity was measured along the foaming direction. At least three measurements were taken for each group of foam samples and results were averaged.

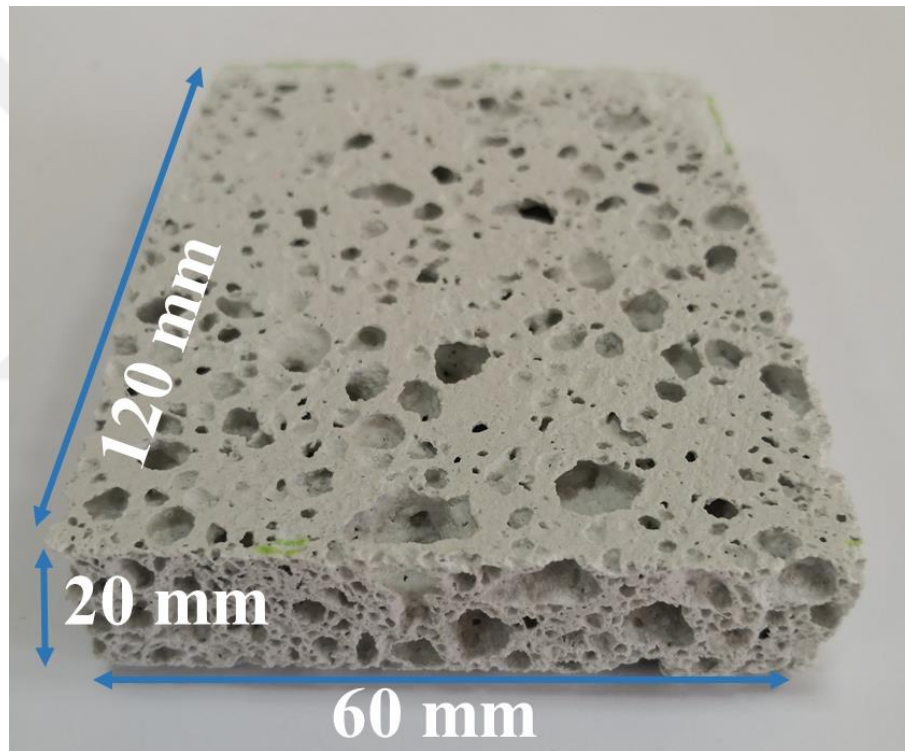


Figure 3.4. The picture of a foam sample for thermal conductivity measurement

3.5. Compression Tests

The density of each cylindrical compression foam sample was measured before testing by dividing the weight by the total volume. The compression tests on the cured and sintered foams were conducted in a SHIMADZU AG-I universal testing machine

using cylindrical test samples 20 mm in diameter and 25 mm in length. The test samples were extracted from the foamed cylinders of slurries or sintered foam cylinders by using a core-drilling machine (Figure 3.5). The top and bottom surfaces of the test samples were made parallel by grinding. Dust accumulated on the samples during core drilling and grinding was removed by applying compressed air. The top and side pictures of a foamed cylinder and foam compression test samples prepared using coarse powder with an S/L ratio of 2 at different aluminum contents are shown in Figure 3.5. Note that the foam expansion direction is the long compression axis of test samples as shown by an arrow in Figure 3.5.

The compression tests were conducted at a strain rate of $1 \times 10^{-3} \text{ s}^{-1}$ at room temperature. A video extensometer was used to measure the displacements during tests and the deformation of samples during the tests was recorded by a video camera. At least 3 tests were performed for each group of foam samples. The nominal strain was calculated by dividing stroke by the length of the long axis and stress by dividing the force by the cross-sectional area.

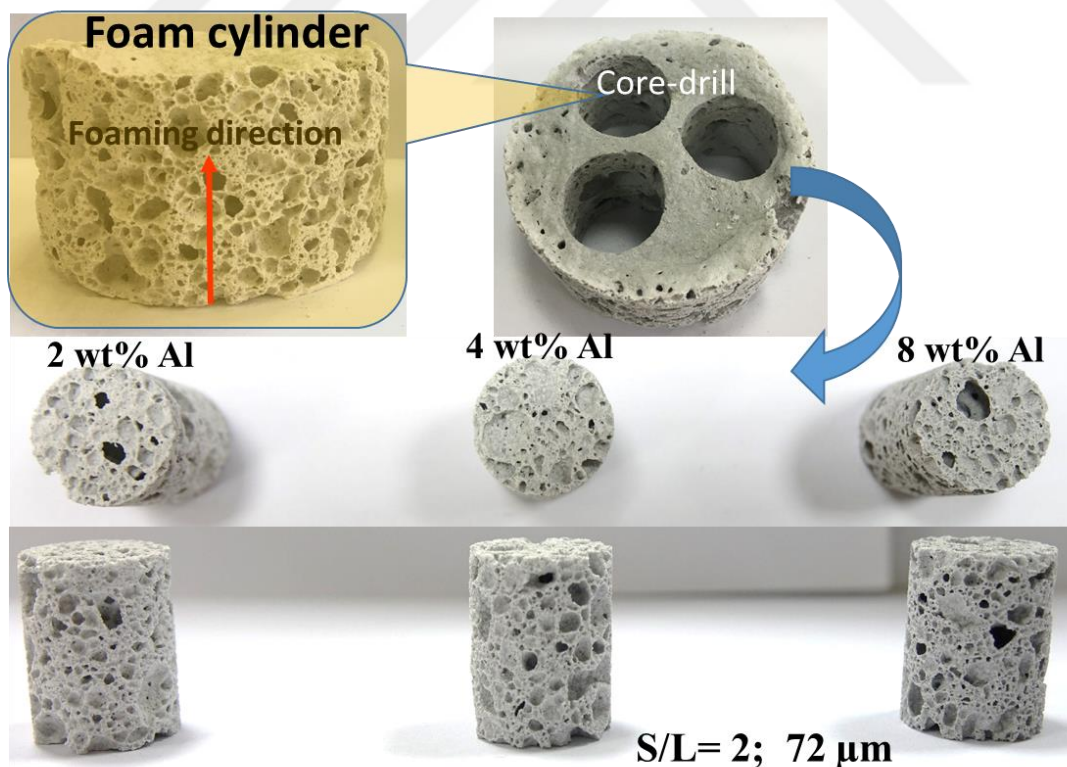


Figure 3.5. The top and side pictures of a foamed cylinder and foam compression test samples prepared using coarse powder with a S/L ratio of 2 at different aluminum contents

CHAPTER 4

RESULTS

4.1. Powder Characterization

The XRF analyses of fine and coarse size glass powders are tabulated in Table 4.1. The used glass powders have similar compositions except the coarse powder contains a slightly higher Al_2O_3 . The used Al foaming agent is essentially an Al-Si alloy powder containing 11% Si as a major element.

Table 4.1. The composition of glass powder

Waste Glass	SiO₂	Al₂O₃	Na₂O	CaO	MgO
Fine powder Weight(%)	73	1.4	12	12	1.6
Coarse powder Weight(%)	73	1.6	12	11.5	1.75

The average particle size of fine powder was previously determined $\sim 23 \mu\text{m}$ ⁶³ and coarse powder $\sim 72 \mu\text{m}$ ⁹. An SEM picture of coarse glass powder is shown in Figure 4.1(a). The particles have angular shapes in small and large sizes. The optical micrograph epoxy mounted and polished Al-powder particles are further shown in Figure 4.1(b). The eutectic Al-Si phases in the same micrograph are differentiable even though no etchant was used. Aluminum particles are irregular in shape and slightly elongated through one axis.

The XRD patterns of glass and aluminum powder are given in Figures 4.2 (a) and (b), respectively. As seen in Figure 4.2(a), as-received coarse glass powder has an amorphous structure. Not shown here, the fine powder had also the same amorphous structure. The XRD pattern of Aluminum powder also shows a good match with the reference pattern of Aluminum-Silicon alloy. The XRD result of aluminium powder is given in Figure 4.2(b).

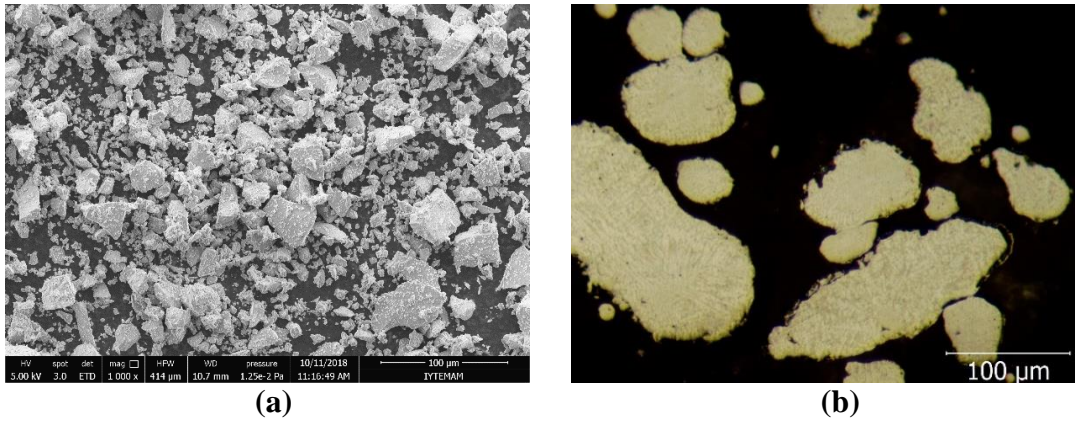


Figure 4.1 (a) SEM picture of glass powder and (b) optical micrograph of the mounted and polished cross-section of Al powder

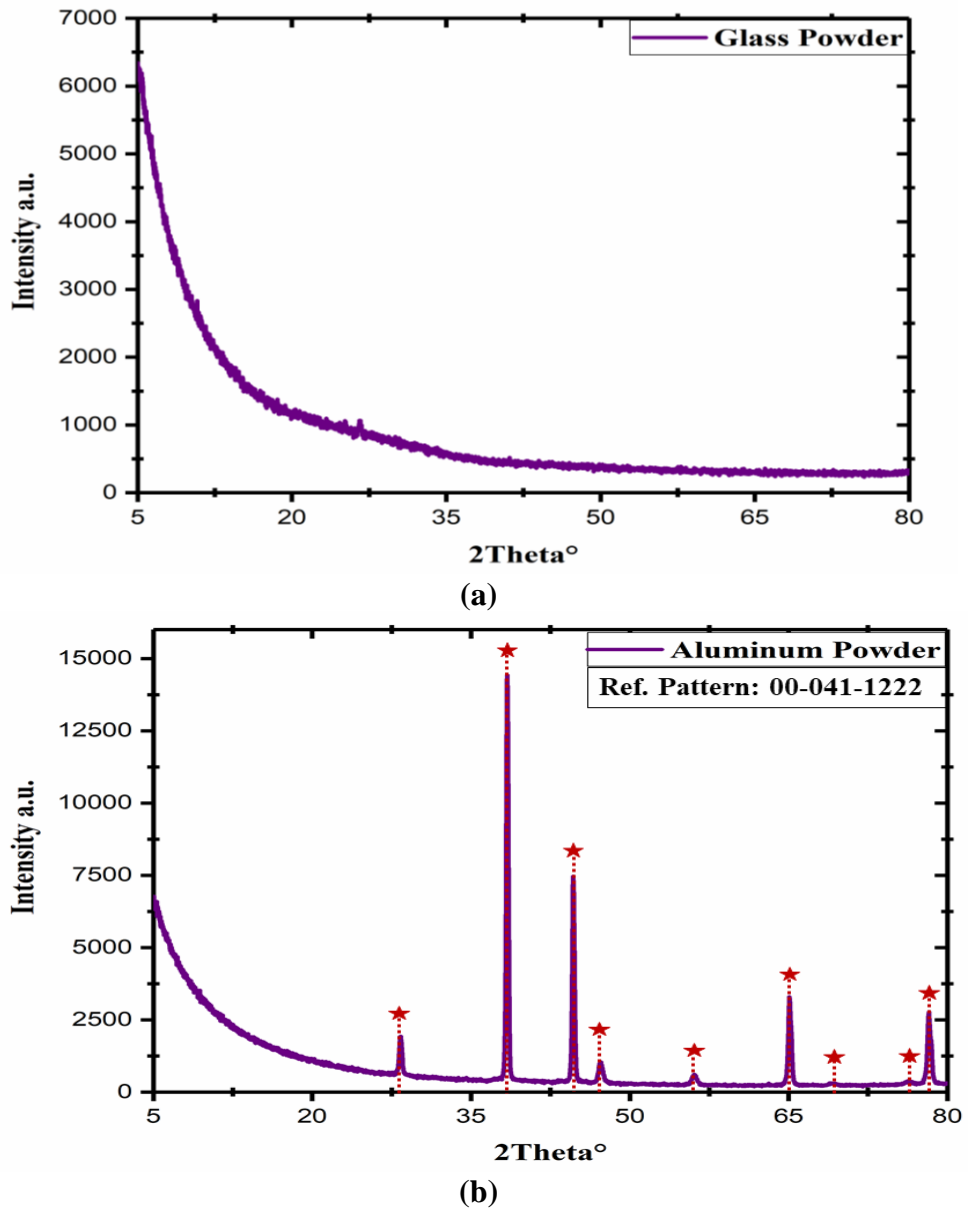


Figure 4.2. The XRD pattern of (a) waste glass and (b) aluminum powder

4.2. Slurry Expansions

The expansion-time and temperature-time curves (two) of fine glass powder slurries with the S/L ratio of 1 and Al content of 4 wt% are shown in Figure 4.3. These curves are representative for the expansion-time and temperature-time curves of all slurries investigated, regardless of the type of powder slurries used. As noted in the same figure, the expansion-time and temperature-time curves of the same slurries are very much similar and hence considered repeatable.

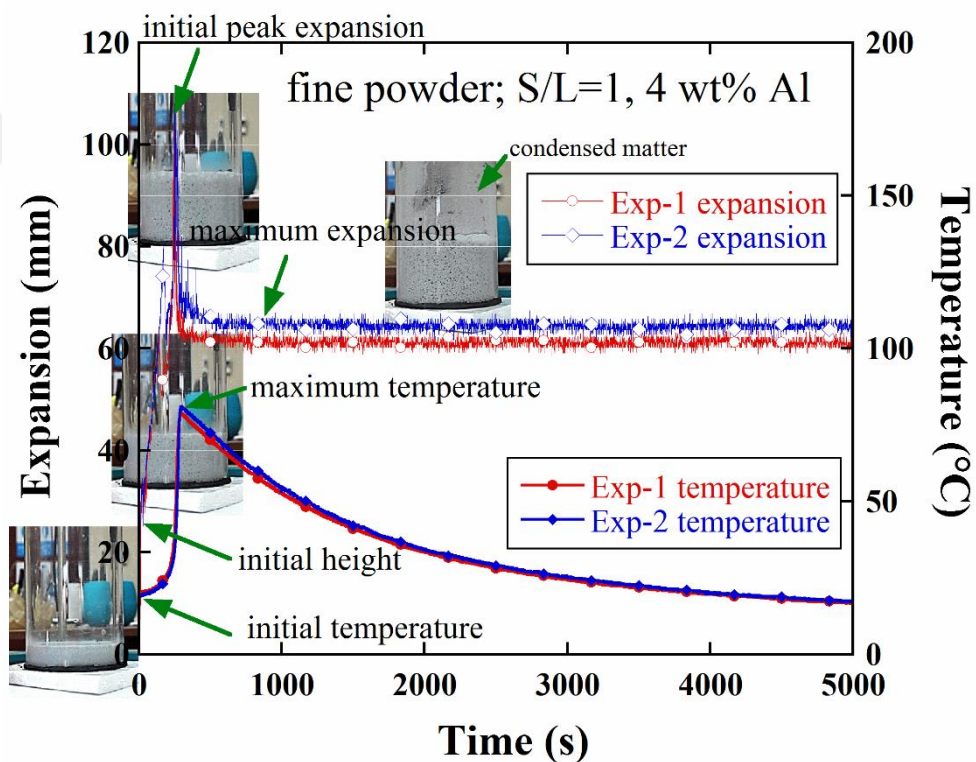


Figure 4.3. The representative expansion-time and temperature-time curves of slurries and the pictures of expanding slurries at various times

The expansion increases rapidly from an initial height as the foaming time increases initially, as shown by the arrows in Figure 4.3. After about an initial peak expansion (see Figure 4.3), the expansion quickly drops off to a constant value; thereafter, it stays nearly constant at increasing foaming times. The expansion in the constant expansion region is considered in the present study as the maximum expansion. The temperature of the slurry also quickly increases from room temperature (see arrow in Figure 4.3) to a maximum value; thereafter, it continuously decreases at increasing times.

The cooling of the foamed slurry to room temperature in Figure 4.3 takes about 5000 s. The maximum temperature in the temperature-time curve is considered as the maximum temperature and it is about 80 °C for the foamed slurry in Figure 4.3. The time to maximum expansion and the time to maximum temperature in Figure 4.3 are also almost the same, ~ 300 s. It is presumed that the gas evolution is terminated after about 300 s. The pictures of the expanding slurries in the foam expansion tube are also shown in Figure 4.3 at various foaming times. The initial rapid expansion of the slurry is also detected in the pictures of expanding slurry. The height of the slurry is about 20 mm at the beginning; then, it increases above 100 mm at the initial peak expansion. The expansion thereafter reduces to 60-65 mm. The initial peak expansions are due to the rapid busting and escape of excessive hydrogen from the surface. The matter in the escaped gas condenses on the foam expansion tube wall interior surface as shown in Figure 4.3.

The representative expansion-time and temperature-time curves of the fine glass powder slurries with the S/L ratio of 1 at increasing wt% of Al are shown in Figure 4.4. Both, the maximum expansion and maximum temperature increase with increasing wt% of Al. The maximum expansions and maximum temperatures of the slurries with 16 and 20 wt% of Al are however very much similar. The maximum temperature in these slurries is about 86 °C. It is noted that the increase in the maximum temperature after about 8 wt% of Al is relatively small as compared with that between 2 and 8 wt% of Al. However, the temperature-time curves of the slurries of different Al contents follow a similar cooling path. The time to maximum expansion and the time to maximum temperature decrease as the wt% of Al increases, showing more rapid foaming of slurries at higher wt% of Al.

The expansion studies on the fine powder slurries with the S/L ratio of 2 were also performed. Nevertheless, the reaction between Al powder and NaOH in these slurries was so quick that the geopolymer reaction already occurred during the mixing Al powder with slurry, except the slurries with 2 wt% of Al. The expansion and temperature curves of the fine powder slurries with the S/L ratio of 2 at 2 wt% Al addition were found very much similar with those of the fine powder slurries with the S/L ratio of 1.

The representative expansion-time and temperature-time curves of the coarse glass powder slurries with the S/L ratio of 1, 1.5 and 2 are sequentially shown in Figures 4.5, 4.6 and 4.7. Common to all S/L ratios, the maximum expansion increases as the content of Al increases from 2 to 8 wt%. Although, the maximum temperature increases

when the Al content increases from 2 to 4 wt%, it almost saturates after about 4 wt% of Al addition.

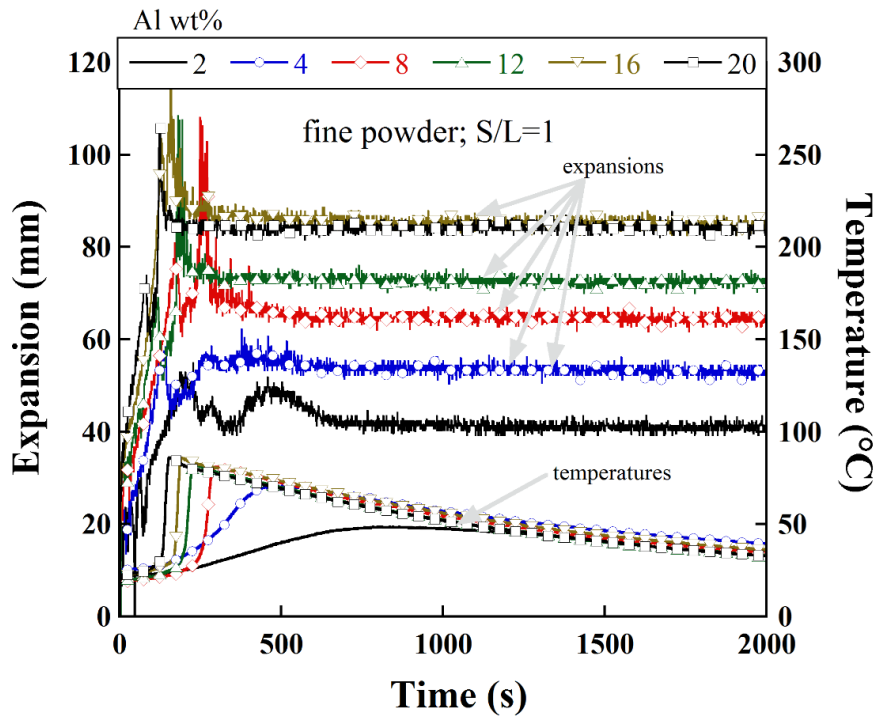


Figure 4.4. The representative expansion-time and temperature-time curves of fine glass powder slurries with the S/L=1 at increasing wt% of Al

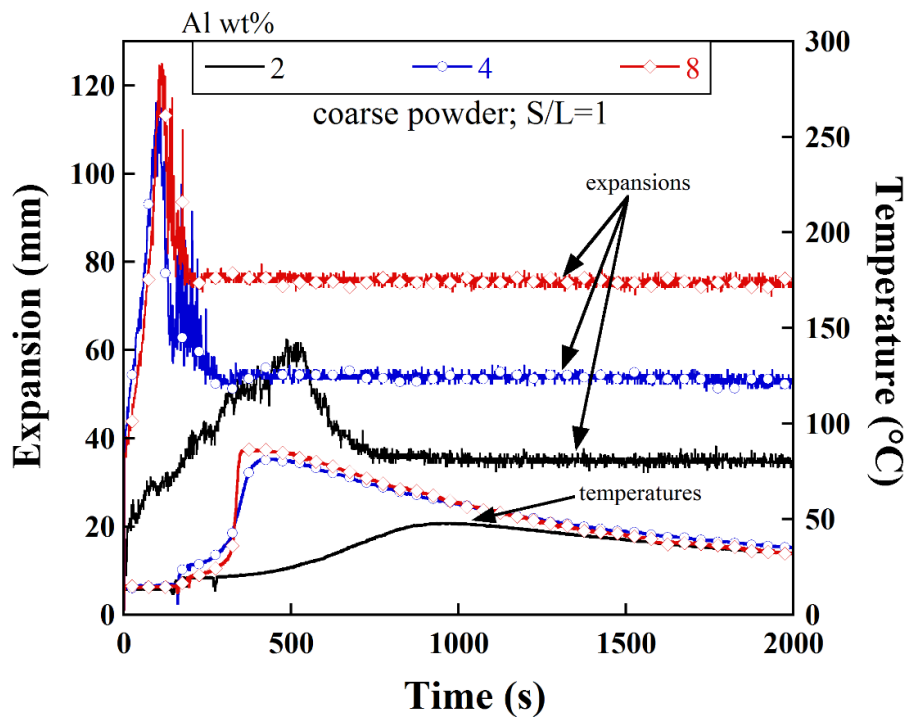


Figure 4.5. The representative expansion-time and temperature-time curves of coarse glass powder slurries with the S/L=1 at increasing wt% of Al

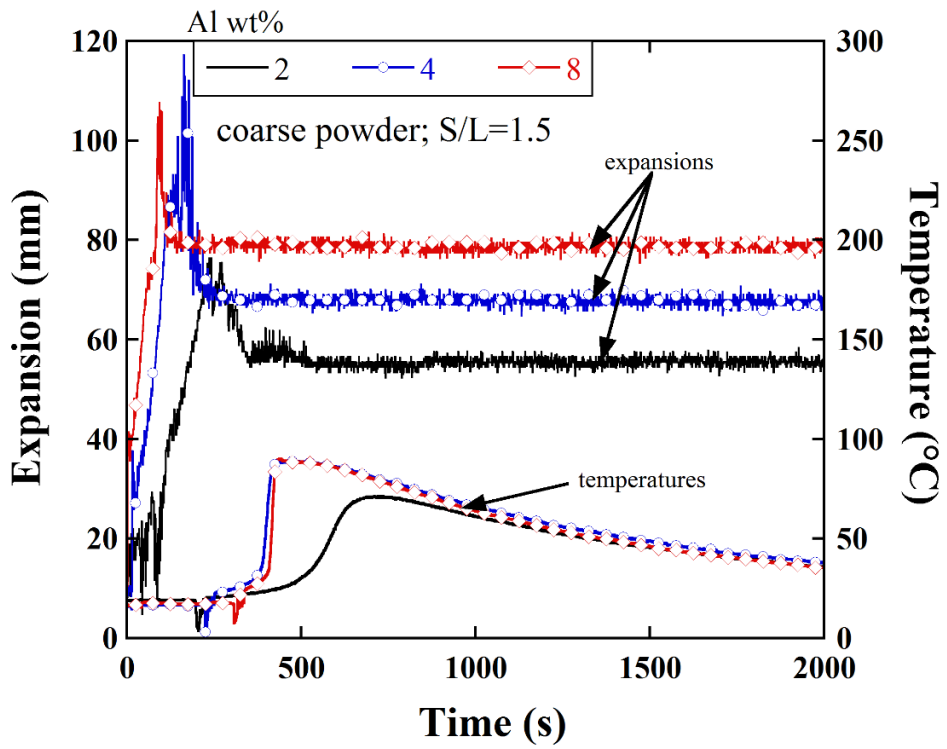


Figure 4.6. The representative expansion-time and temperature-time curves of coarse glass powder slurries with the S/L=1.5 at increasing wt% of Al

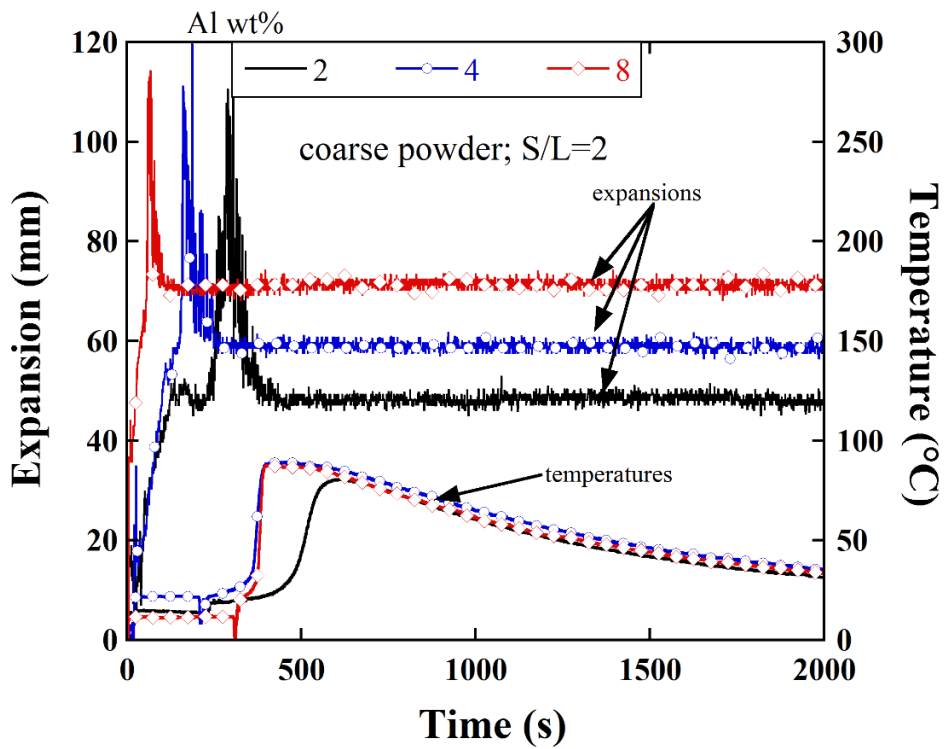
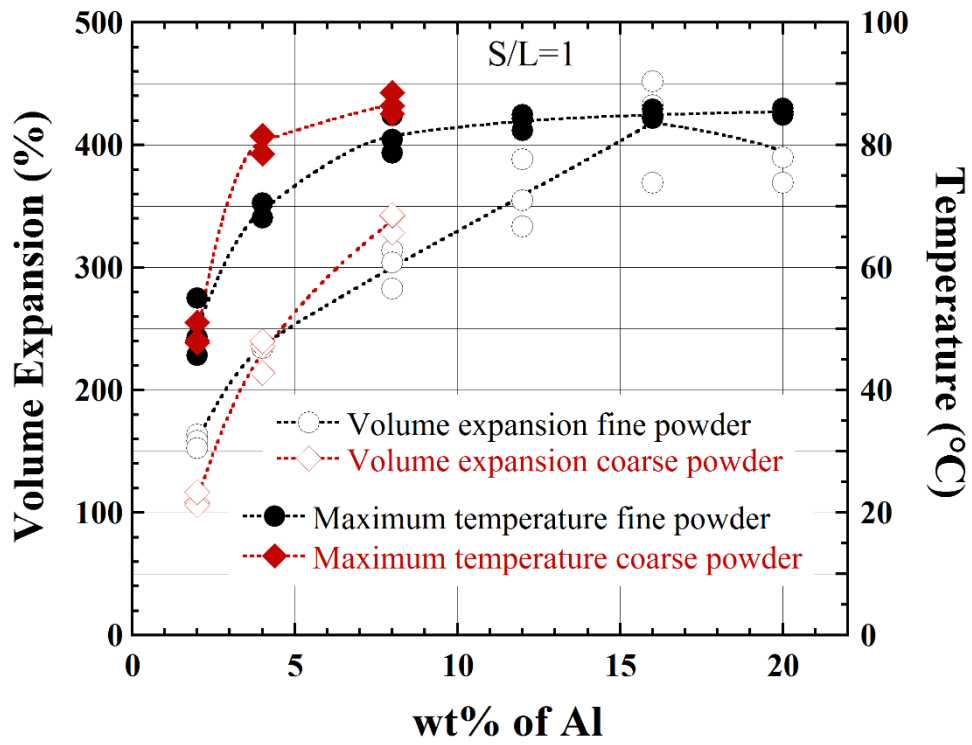


Figure 4.7. The representative expansion-time and temperature-time curves of coarse glass powder slurries with the S/L=2 at increasing wt% of Al

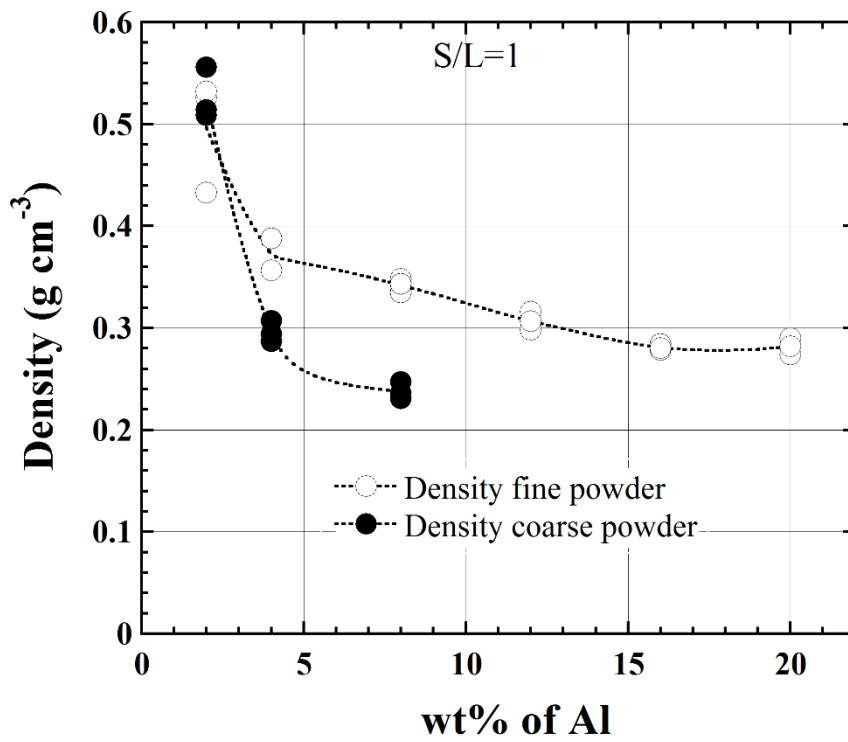
The effect of Al content on the maximum volume expansions and maximum temperatures of the fine and coarse powder slurries with the S/L ratio of 1 is shown in Figure 4.8(a). The maximum volume expansion of the fine powder slurries continuously increases with increasing the Al content until about 16 wt%. A significant increase in the maximum temperature of the fine powder slurries is seen between 2 and 8 wt% Al, while the maximum temperature tends to saturate at about 90 °C after about 12 wt% Al. In general, the coarse powder slurries show very much similar trends in the maximum temperature and volume expansion with the fine powder slurries as seen in Figure 4.8(a). Although, the coarse powder slurries exhibit lower expansions at 2 wt% of Al, they show similar temperatures with the fine powder slurries. When the Al content increases to 8 wt%, both the maximum expansions and temperatures of the coarse powder slurries become higher than those of the fine powder slurries.

The change of cured densities of foams prepared using the fine and coarse powder slurries at the S/L ratio of 1 is shown in Figure 4.8(b). As noted, the final densities of foamed slurries also vary with the Al content. In general, increasing the Al content decreases the final density. The coarse powder slurries however result in lower final densities than the fine powder slurries, 240-530 kg m⁻³ between 2 and 8 wt% Al. The final densities of the fine powder slurries range 280-530 kg m⁻³ between 2 and 16 wt% Al. The final densities of 16 and 20 wt% Al slurries are however almost the same as seen in Figure 4.8(b). In brief, the higher is the expansion; the lower is the final foam density.

Figures 4.9 (a-c) show sequentially the effects of the S/L ratio on the maximum volume expansion, maximum temperature and density of the foamed coarse powder slurries. As is seen in the same figures, the volume expansion increases with increasing the S/L ratio from 1 to 1.5, while increasing the S/L ratio from 1.5 to 2 decreases the expansions. The highest expansion is attained, when S/L=1.5. The maximum temperature is highest when S/L=2 and lowest, when S/L=1 at 2 wt% Al. The maximum temperatures are very similar for the S/L ratio of 1.5 and 2 at 4 wt% Al, while all the coarse powder slurries approach nearly the same maximum temperatures, 85-90 °C, at 8 wt% of Al addition (Figure 4.9(b)). Except for the slurries with the S/L=1 at 2 wt% of Al, the increase of the S/L ratio increases the final densities of foamed slurries as noted in Figure 4.9(c). These further confirm that both the Al content and the S/L ratio are effective in altering the final densities of foamed slurries. The final densities vary between 240 and 350 kg m⁻³ at 8 wt% Al for the slurries with the S/L ratios of 1 and 2.

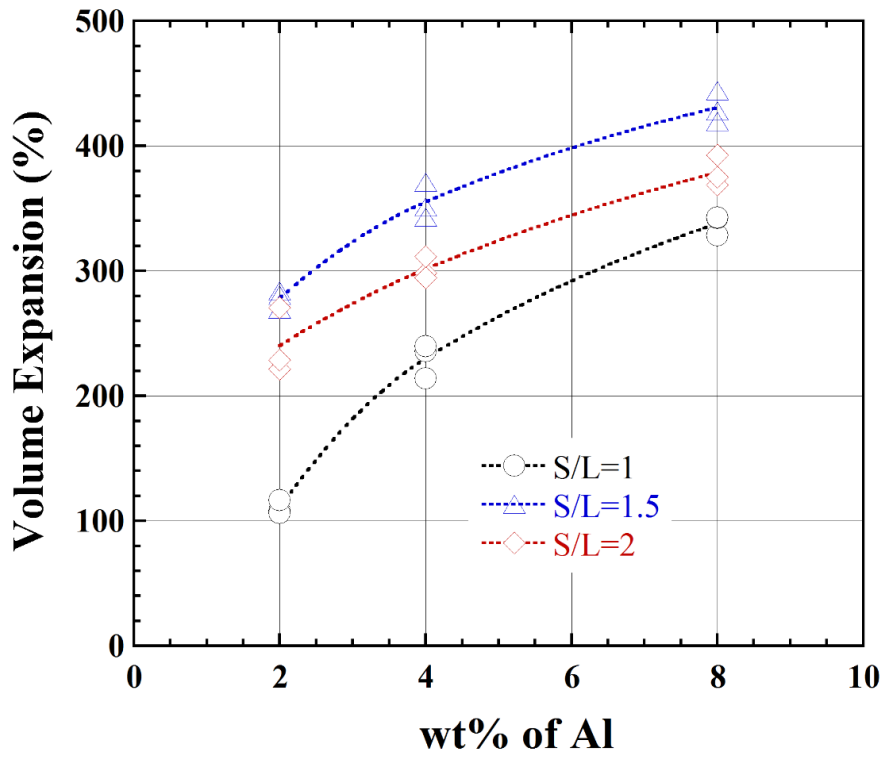


(a)

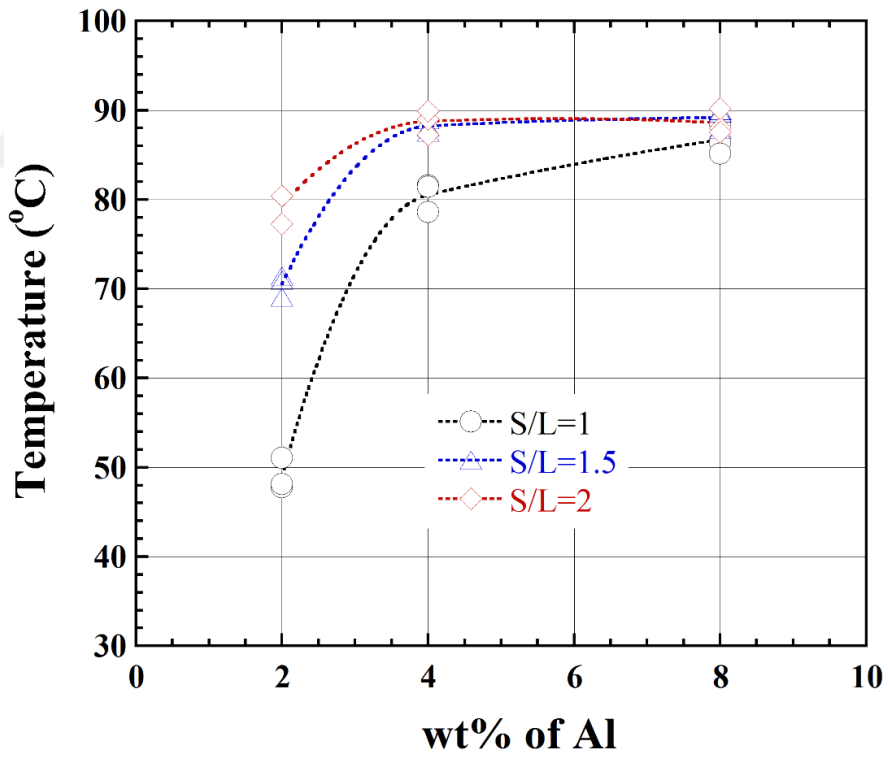


(b)

Figure 4.8. The variation of (a) the maximum expansion and temperature and (b) the foam density with wt% of Al in the fine and coarse powder slurries with the S/L ratio of 1

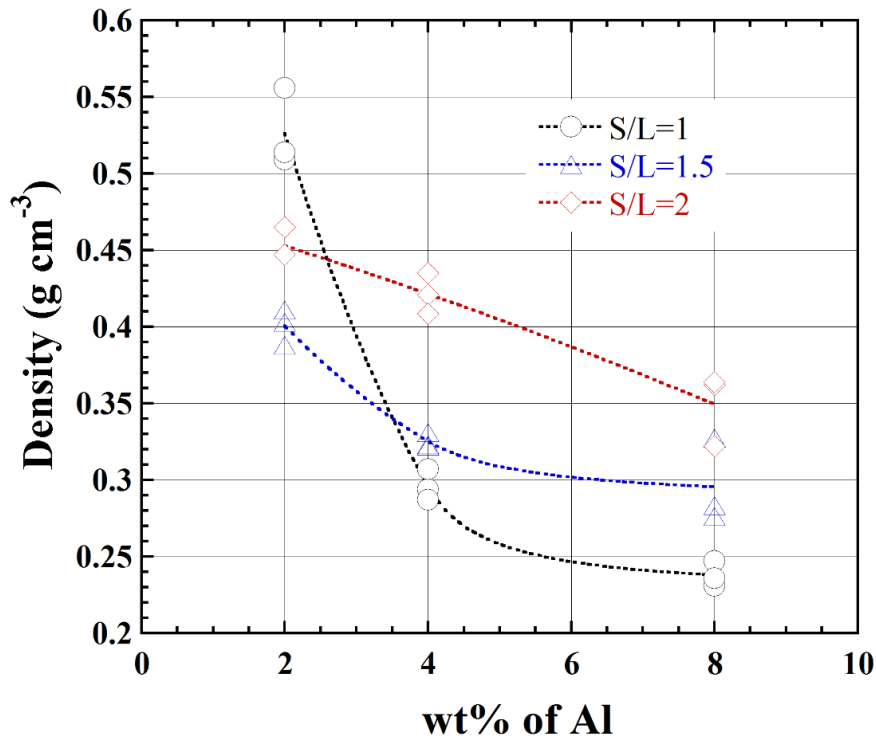


(a)



(b)

(cont. on next page)



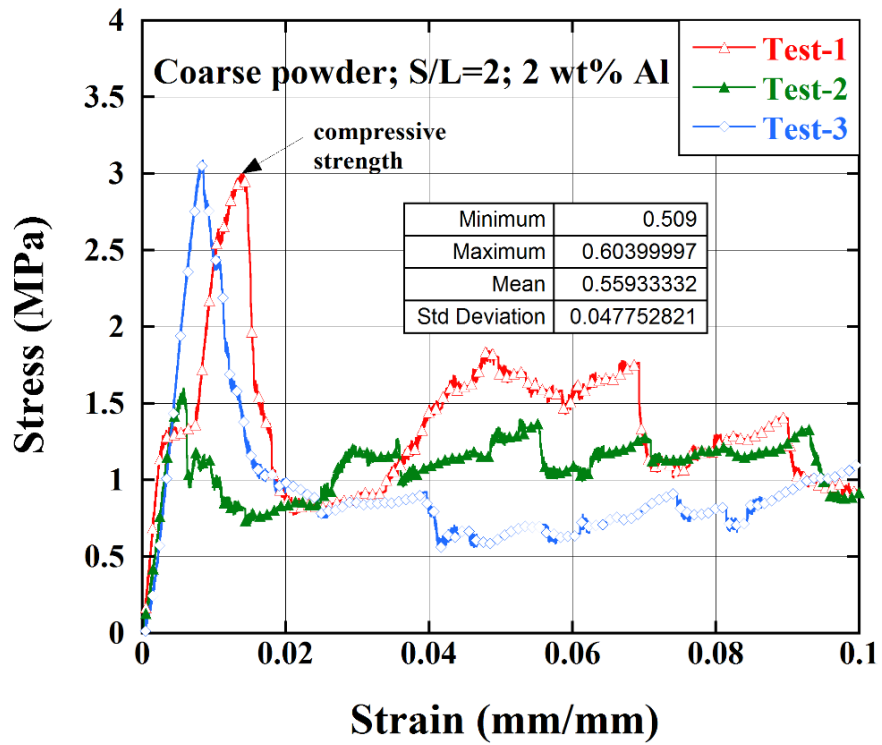
(c)

Figure 4.9. The variation of (a) the maximum expansion, (b) temperature and (c) density with wt% of Al in the coarse powder slurries with the S/L ratios of 1, 1.5 and

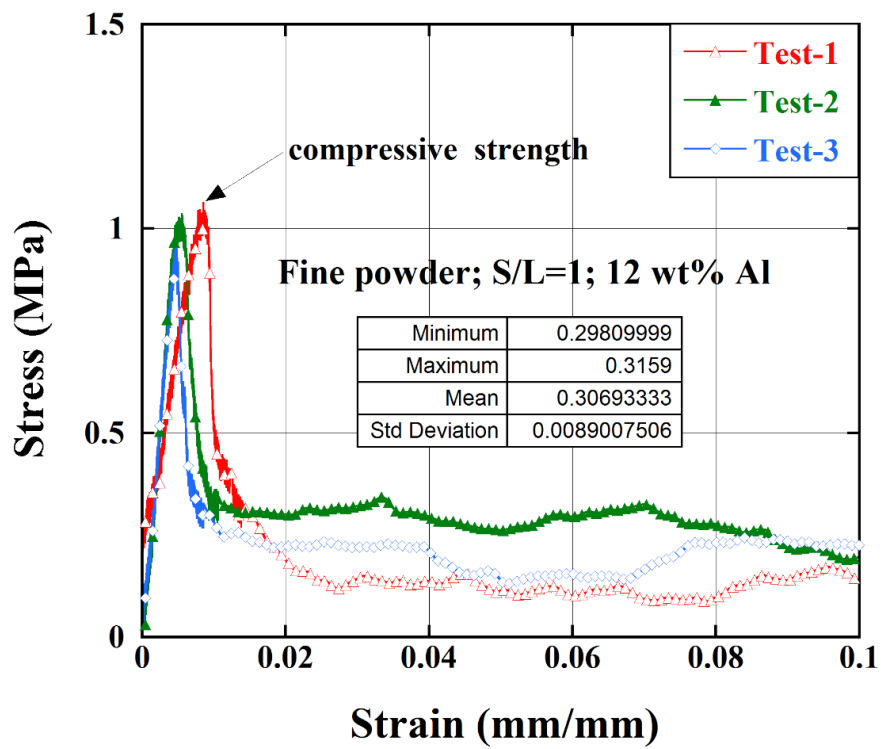
2

4.3. Compression Tests

The compression stress-strain curves of the foamed fine powder slurries with S/L=2 at 2 wt% Al and with S/L=1 at 12, 16 and 20 wt% of Al are shown in Figures 4.10(a-d), respectively. The foam samples prepared using the fine powder slurries were too brittle, fractured in several pieces during core drilling. Therefore, the compression test samples of all foamed powder slurries could not be prepared by core drilling. The maximum, minimum and mean densities (with the corresponding standard deviations) of the tested foamed samples are further tabulated in the inset of Figures 4.10 (a-d). The tested foam samples show typical stress-strain behavior of brittle materials, fracturing following an elastically deformed region after a maximum stress (taken as the compressive strength) as marked in Figures 4.10 (a) and (b). As the mean densities decrease in the same figures from 0.56 to 0.28 g cm⁻³, the compressive strength decreases from about 3 MPa to 0.5 MPa as seen in Figures 4.10 (a-d).



(a)



(b)

(cont. on next page)

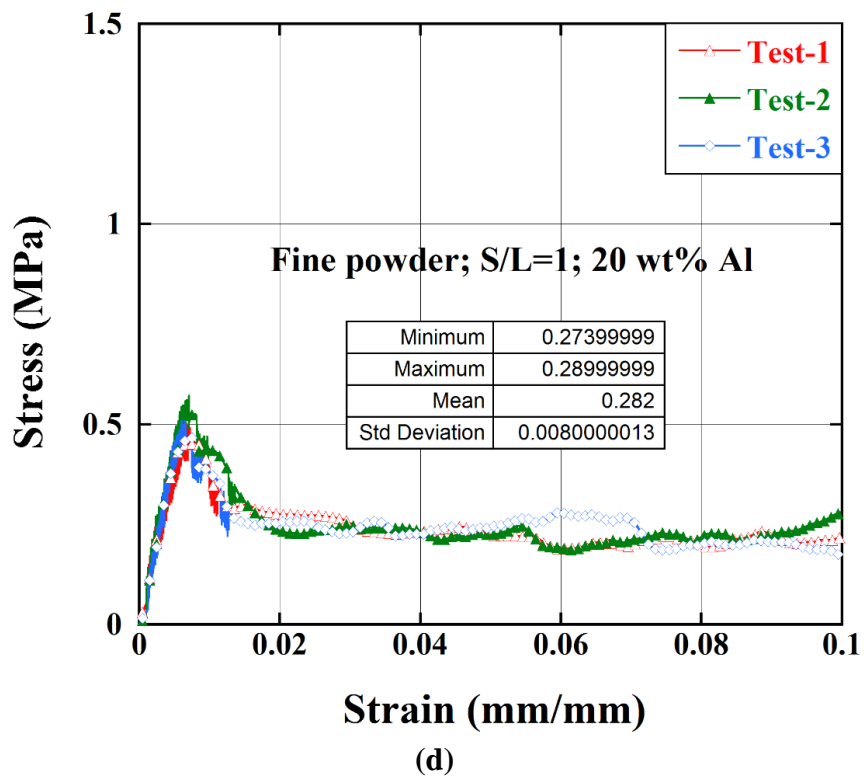
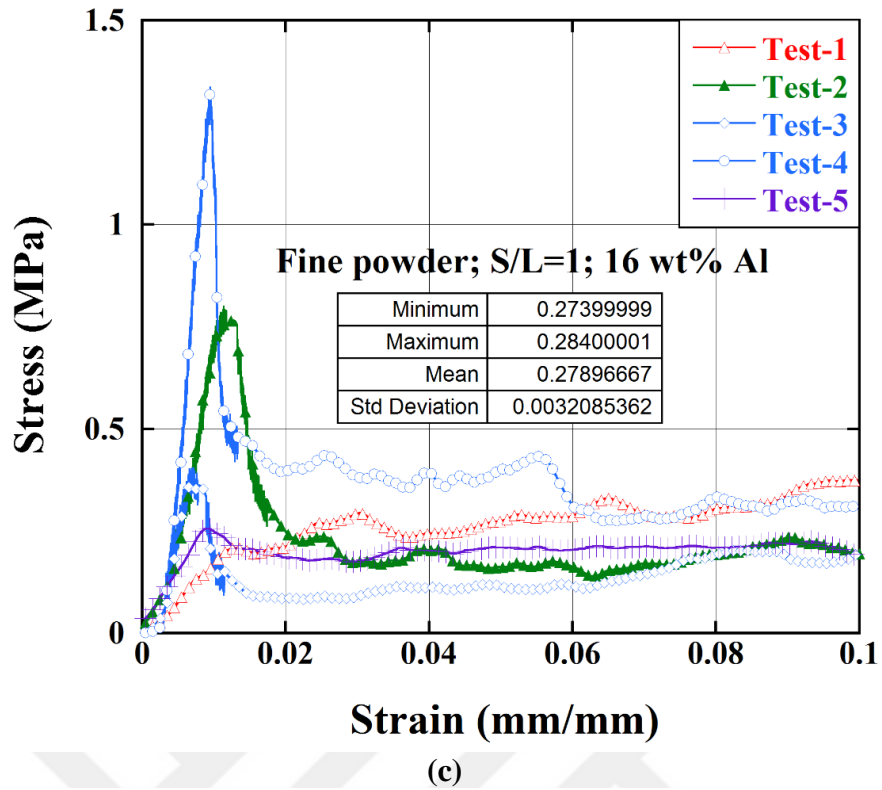
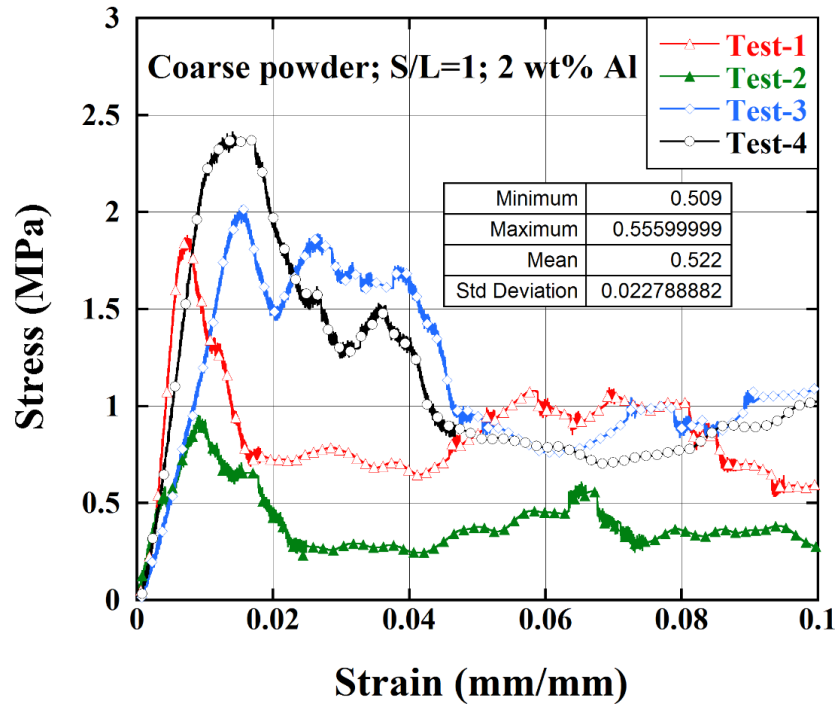


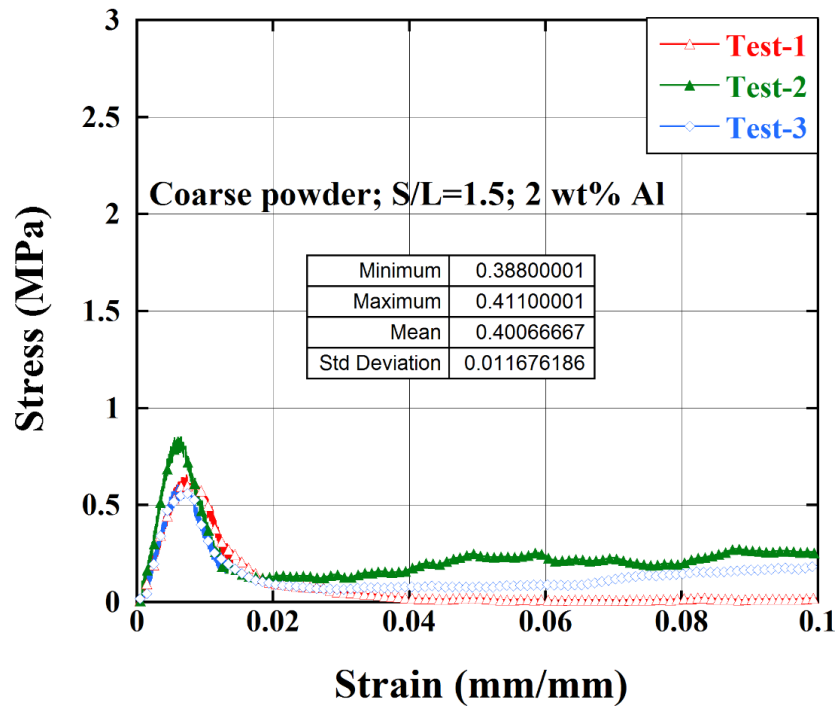
Figure 4.10. The compressive stress-strain curves of the foam samples of fine powder slurries with the S/L=2 at (a) 2 wt% Al and S/L=1 at (b)12, (b) 16 and (d)20 wt% Al

The compression stress-strain curves of the foamed coarse powder slurries with the S/L=1, 1.5 and 2 at 2 wt% Al are shown in Figures 4.11 (a-c), respectively. The

highest compressive strength is seen in the coarse powder foamed slurries with the S/L=1, as these foams have also the highest mean density, 0.55 g cm^{-3} (Figure 4.11(a)). Similarly, the highest compressive strength is found in the coarse powder foamed slurries with the S/L=2 at 8 wt% Al, since these foams have also the highest mean density as seen in Figures 4.12(a-c).

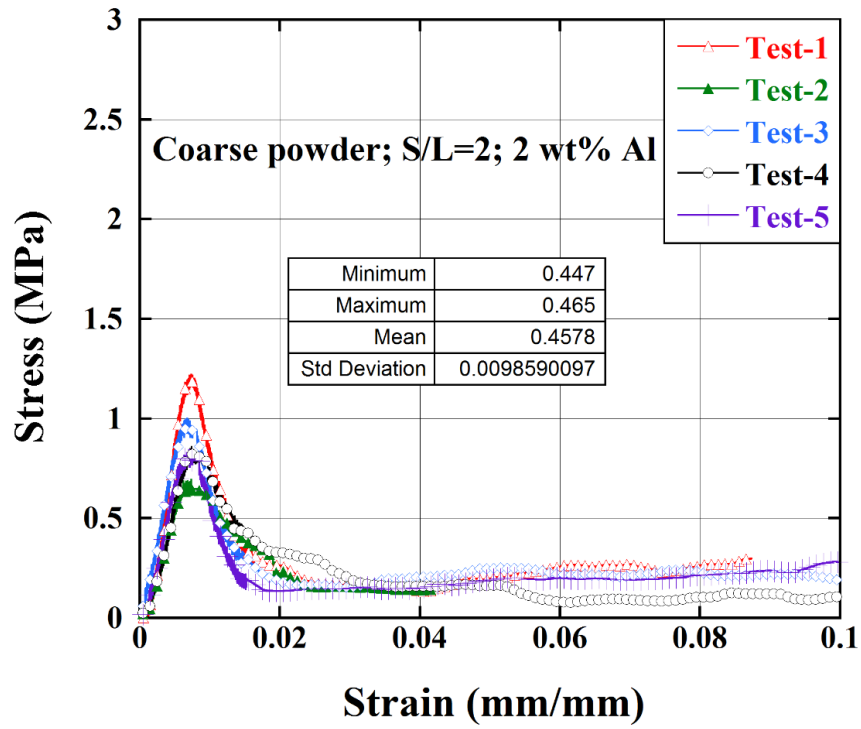


(a)



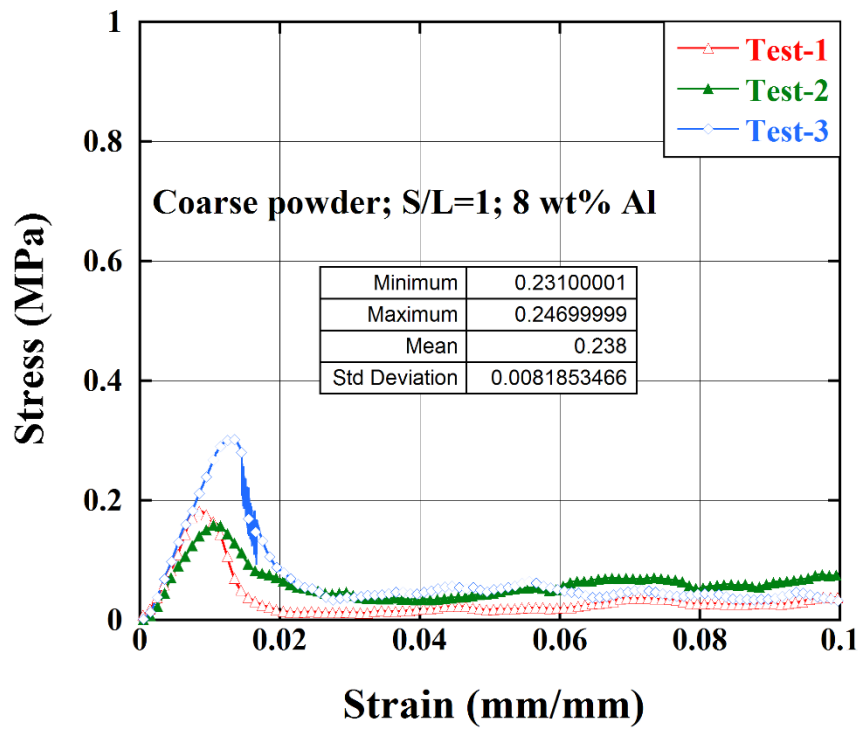
(b)

(cont. on next page)



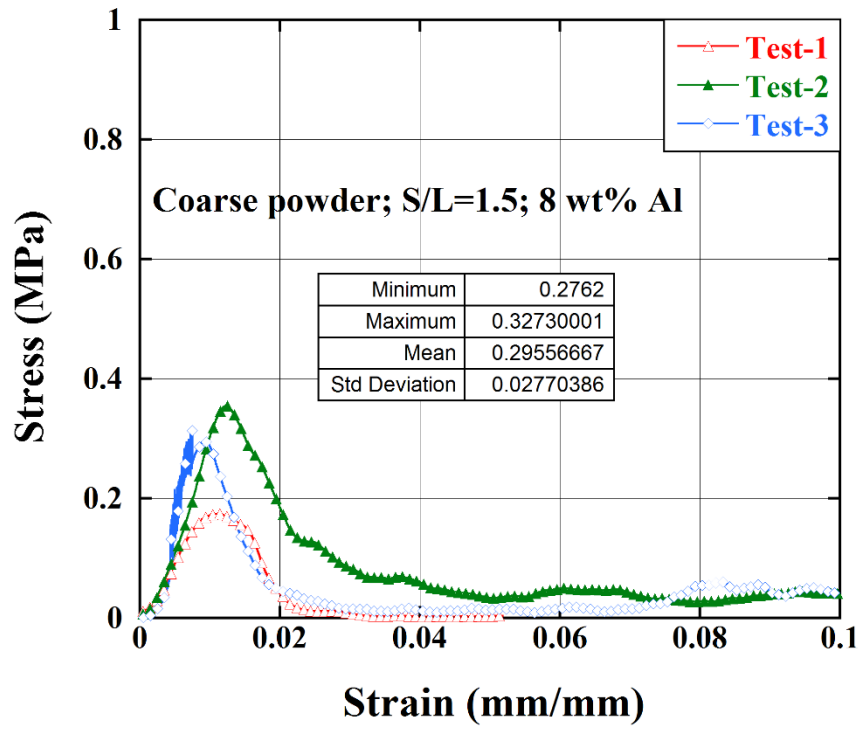
(c)

Figure 4.11. The compressive stress-strain curves of foam samples of fine powder slurries with 2 wt% Al and S/L ratio (a) 1, (b) 2 and (c) 1.5

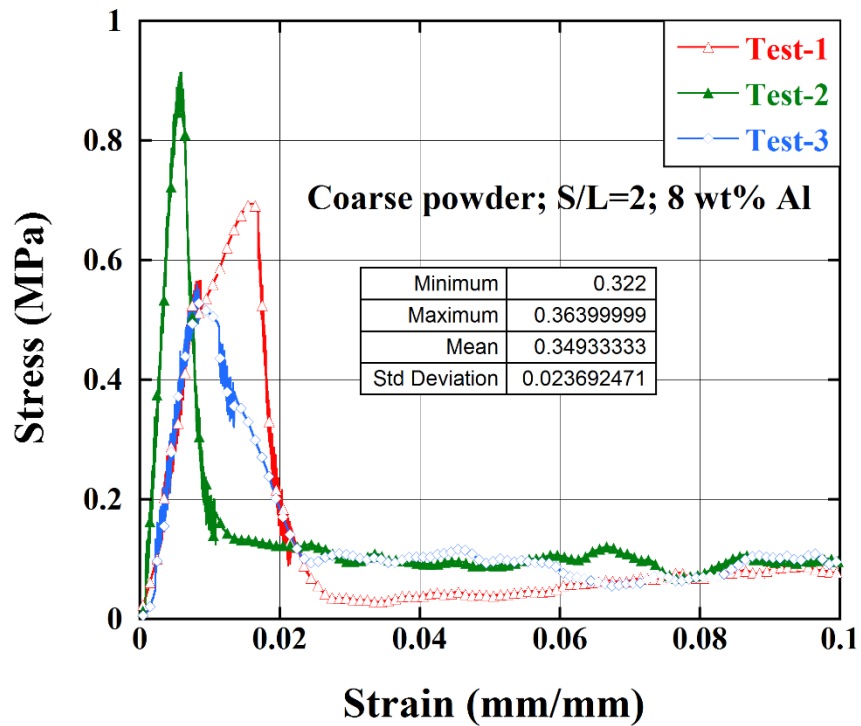


(a)

(cont. on next page)



(b)



(c)

Figure 4.12. The compressive stress-strain curves of foam samples of fine powder slurries with 8 wt% Al and S/L ratio (a) 1, (b) 2 and (c) 1.5

The representative compressive stress-strain curves of geopolymer glass foams sintered at 600, 700, 725 and 750 °C are shown in Figure 4.13. The compression tests on

sintered foams also resulted in repeatable stress-strain curves. The mean densities of tested foams are also shown in the legend of the same figure. Note that the sintering foamed slurry of the coarse powder (S/L=2 and 2 wt% Al) at 600 °C results in a similar density; hence, similar compressive strength with the unsintered foam. The effect of sintering on the compressive strength and density starts at and after 700 °C. The highest increase in compressive strength is seen at 750 °C with a final mean density of 0.380 g cm⁻³. The increase in compressive strength is almost two times that of the unsintered foam sample. In addition, there is a 15% shrinkage after sintering at 750 °C in the foam samples.

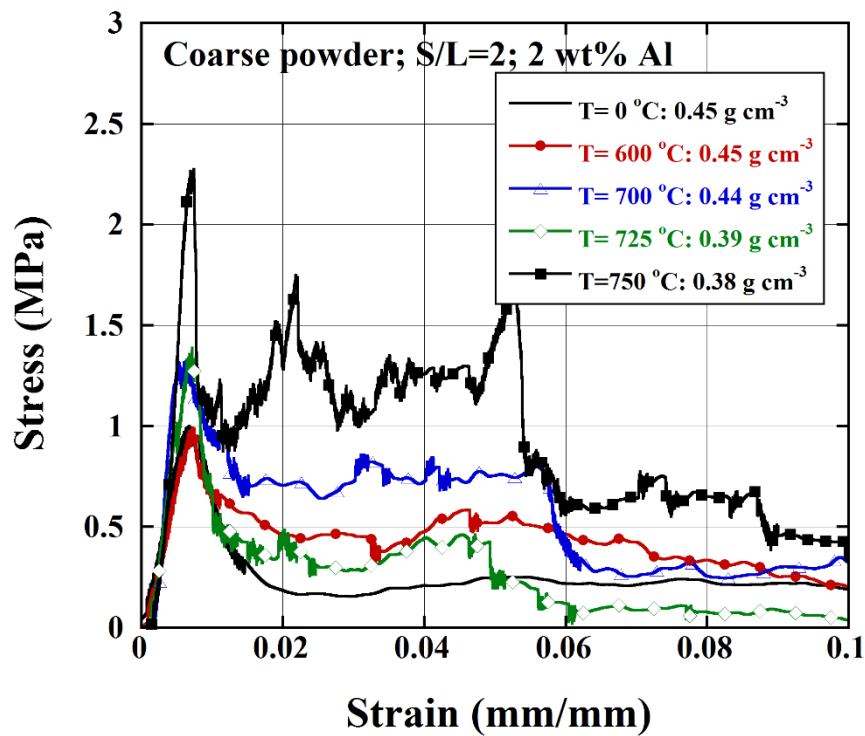


Figure 4.13. The representative compressive stress-strain curves of geopolymer glass foam samples sintered at different temperatures

The mean compressive strength of the geopolymer and sintered geopolymer foams according to the average density for the groups having different amount of Al in all S/L ratios and different glass particle sizes are given in Table 6.1. The variations of the compressive strengths of the foamed fine and coarse powder slurries with the density are shown in Figure 4.14. The compressive strengths of the sintered foams of coarse powder slurries at 600, 725 and 750 °C are also shown for comparison. At low foam densities, shown by a circle and numbered 1 in the same figure, the foams of the fine powder slurries exhibit higher compressive strengths than those of the coarse powder

slurries. Nevertheless, both powder foams show similar compressive strengths at about 0.500 g cm^{-3} as shown in region 2 of the same figure. Note also that sintering the foams at 725 and 750 °C results in higher compressive strengths than the foams of coarse powder slurries at similar densities as shown by circles in Figure 4.14.

Table 4.2 The mean compressive strength for the groups all produced geopolymer and sintered geopolymer foams according to density

Sample Name	S/L Ratio	Density (kg m^{-3})	Compressive Strength (MPa)
L0	1	560	2.41
L1	1	294	0.242
L2	1	230	0.20
N0	1.5	403	0.85
N1	1.5	323	0.67
N2	1.5	295	0.342
M0	2	465	1.1
M1	2	418	0.916
M2	2	342	0.723
S3	1	306	1.04
S4	1	284	0.50
S5	1	282	0.54
M0-600 °C	2	464	0.82
M0-700 °C	2	448	1.81
M0-725 °C	2	386	1.45
M0-750 °C	2	380	2.20

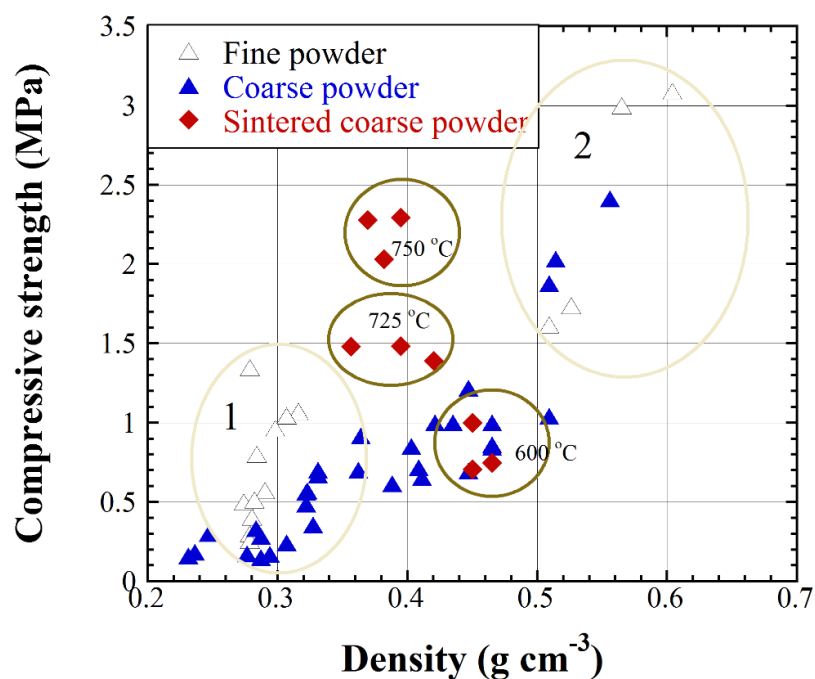


Figure 4.14. Compressive strength versus density of foams

Regardless of the foam density, the geopolymer and sintered geopolymer foams fail by axial cracks starting from either the upper or bottom of compression test platens as shown in Figures 4.15 (a-d). The fracture occurs at relatively low strains, which is lower than 0.01. After the formation of cracks, the deformed foam sample stays in contact with the compression test platens and the un-fractured pieces continuously compressed and fractured, leading to a plateau stress region after the compressive strength in the stress-strain curves.

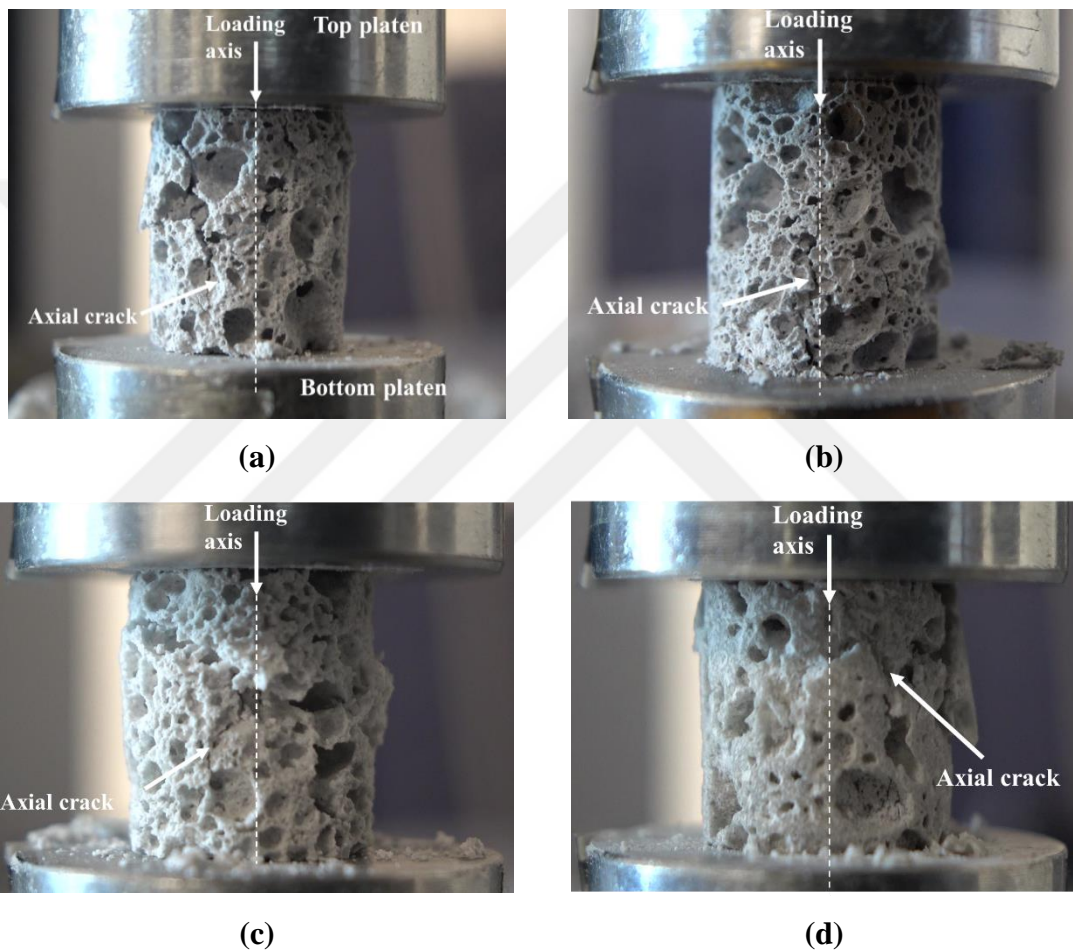


Figure 4.15. The pictures of deformed foam samples of coarse powder slurry at 2 wt% Al and the S/L of (a) 2, (b) 1.5 and (c) 1 and (d) the fine powder slurry at 12 wt% Al and the S/L=1

4.4. Thermal Conductivity

Thermal conductivity measurements were performed on the samples foamed using different S/L ratios at a constant Al addition, 2 wt%. Measurements were also

performed on the samples sintered at 750 °C. The average thermal conductivity (3 measurements) of the foam and sintered foam samples are tabulated together with densities in Table 4.2. The thermal conductivities as seen in the same table decrease as the density of foams decreases. The average thermal conductivity decreases from 0.1808 at 0.585 g cm⁻³ density to 0.078 at 0.368 g cm⁻³.

Table 4.3. The thermal conductivities and the corresponding densities of foam and sintered foams samples with 2 wt% Al addition.

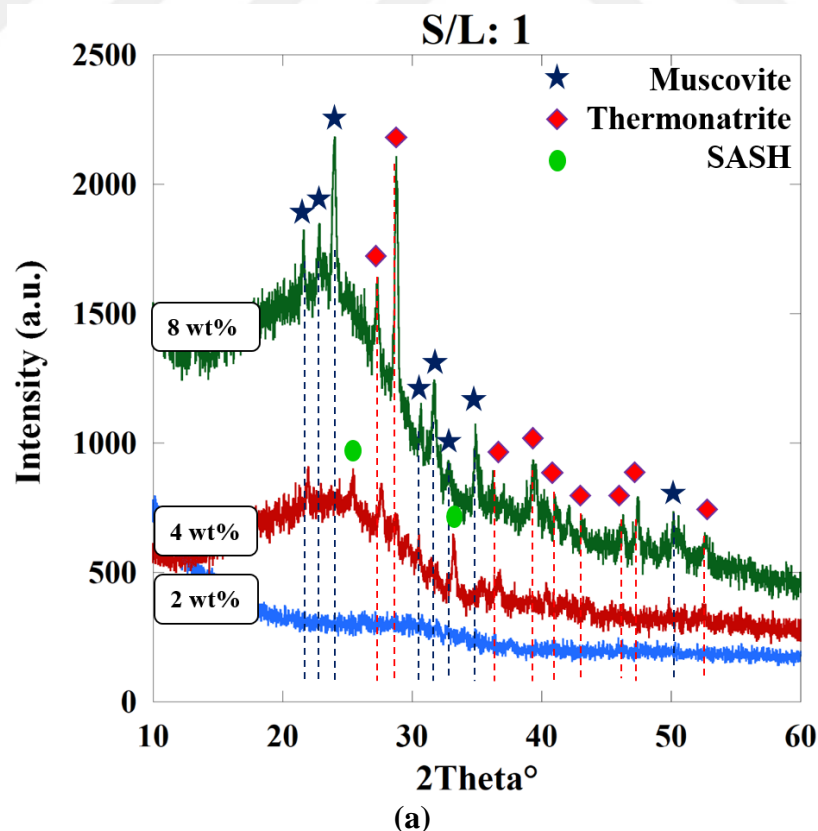
Sample Name	S/L Ratio	Density (g cm ⁻³)	Average Thermal Conductivity (W/mK)
L0	1	0.585	0.1808 (0.1617-0.1985)
N0	1.5	0.535	0.1158 (0.1042-0.1230)
M0	2	0.462	0.1100 (0.0888-0.1289)
M0-750 °C	2	0.368	0.0780 (0.0672-0.0934)

4.5. XRD and FTIR Analysis

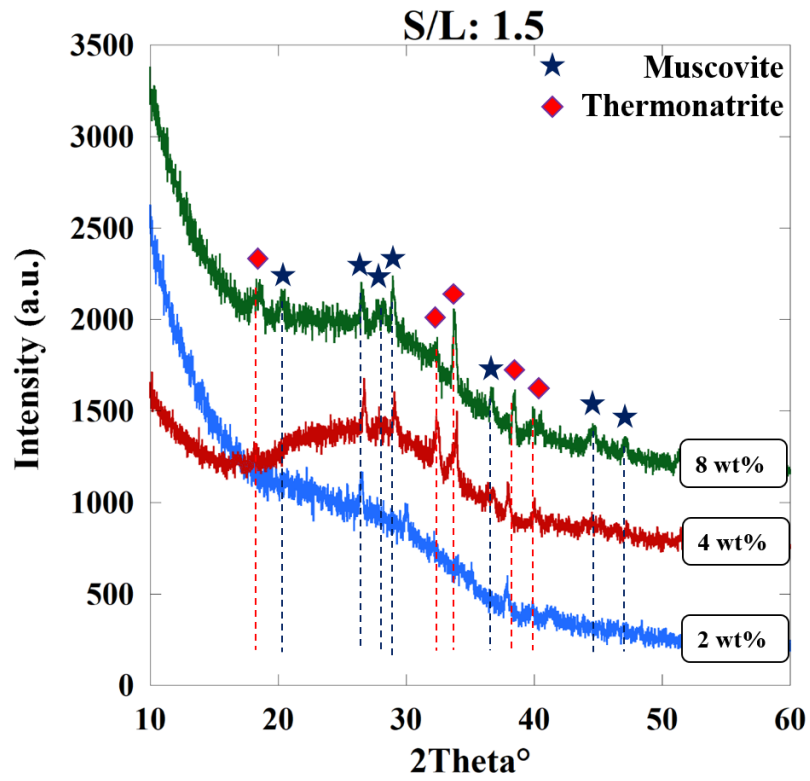
The XRD patterns of the cured geopolymer coarse powder glass foams with the S/L=1, 1.5 and 2 are shown in Figures 4.16 (a-c), respectively and the sintered geopolymer foams in Figure 4.16(d). Foams processed with different S/L ratios show similar crystal phases as seen in Figures 4.16(a-c). These are Thermonitrite (Na₂CO₃·H₂O) (Ref. No: 00-008-0448), Sodium Aluminum Silicate Hydrate (SASH) (Na₂Al₂Si_{17.5}O_{35.4}·8H₂O) (Ref. No: 00-035-0375) and Muscovite (NaAl₂(AlSi₃O₁₀)(OH)₂) (Ref. No. 00-046-1311). Sodium Aluminum Silicate Hydrate is only seen at S/L=1, while Thermonitrite and Muscovite are detected in all S/L ratios. The XRD patterns of the foams processed with the S/L=1 show Muscovite and Thermonite crystal structures at 2 wt% of Al; thereafter, SASH is seen when the Al content increases to 4 wt%. With increasing Al content to 8 wt% SASH disappears and Muscovite and Thermonite are seen again (Figure 4.16(a)). The peak intensities are noted to increase with increasing the Al content. The XRD patterns of the sintered foams show only the peaks Muscovite and SASH as seen in Figure 4.16(d) with significantly reduced peak intensities.

The FTIR analysis of the geopolymer foams of the coarse powder slurries with the S/L ratio of 1, 1.5 and 2 at 2, 4 and 8 wt% Al foaming agent are shown in Figures 4.17 (a-c), respectively. In the same figures, the FTIR analysis of the waste coarse glass

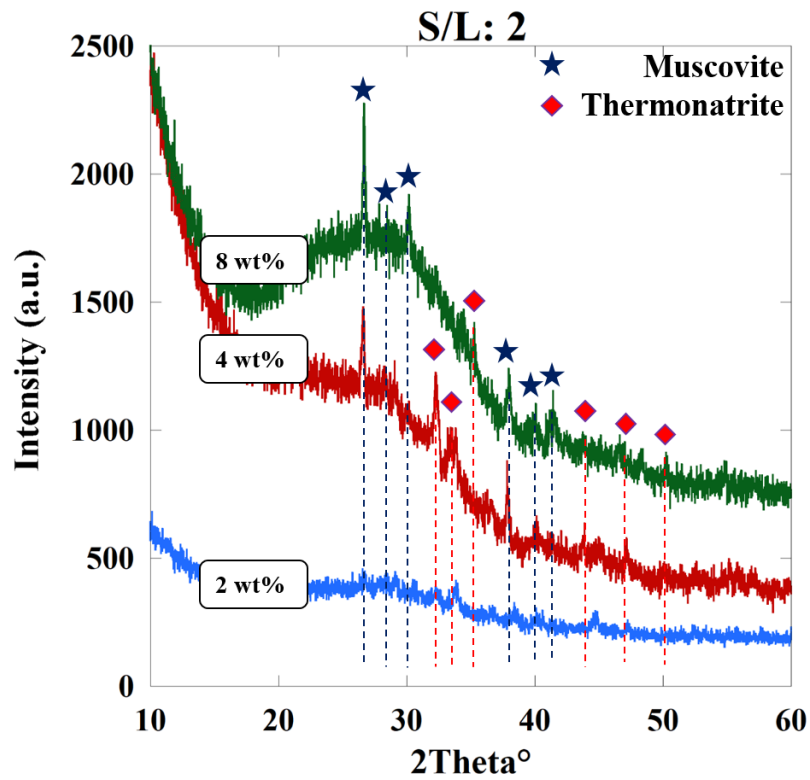
powder is also shown as a reference. Three bond-peak are taken attention (Figures 4.17 (a-c)). The first bond at 771 cm^{-1} is only seen in the WG and refers to the Si-O bond, which is the bond in SiO_4 tetrahedron. The Si-O bond in the SiO_4 tetrahedron is absent in the FTIR graphs of geopolymer foams. The main bond around 975 cm^{-1} is due to the stretching vibration of the Si-O-Si bond. Normally, the Si-O-Si vibration occurs at around $980\text{-}1000\text{ cm}^{-1}$, while the presence of Si-O-Al bond shifts this wave number slightly to lower values as shown in the inset of Figure 4.17(a). The shift is seen in all geopolymer foams processed with different S/L ratios and Al contents. While, the shift seen in the FTIR analysis of WG is due to the alumina content of the glass powder (1.6%). The wavenumber shift is the highest in the foams of slurries with 2 wt% Al and the lowest in the foams of slurries with 8 wt% Al. The peak between 1435 and 1450 cm^{-1} is due to the O-C-O stretching, only seen in geopolymer foams. The O-C-O stretching occurs because of the presence of carbonate. The FTIR analysis of sintered foams of the slurries with S/L=2 and 2 wt% Al at different temperatures are shown in Figure 4.18. The main bonds around 946 cm^{-1} are due to the stretching vibration of the Si-O-Si bond. The carbonate vibration at 1435 cm^{-1} seen in geopolymer foam disappears in the sintered foams.



(cont. on next page)

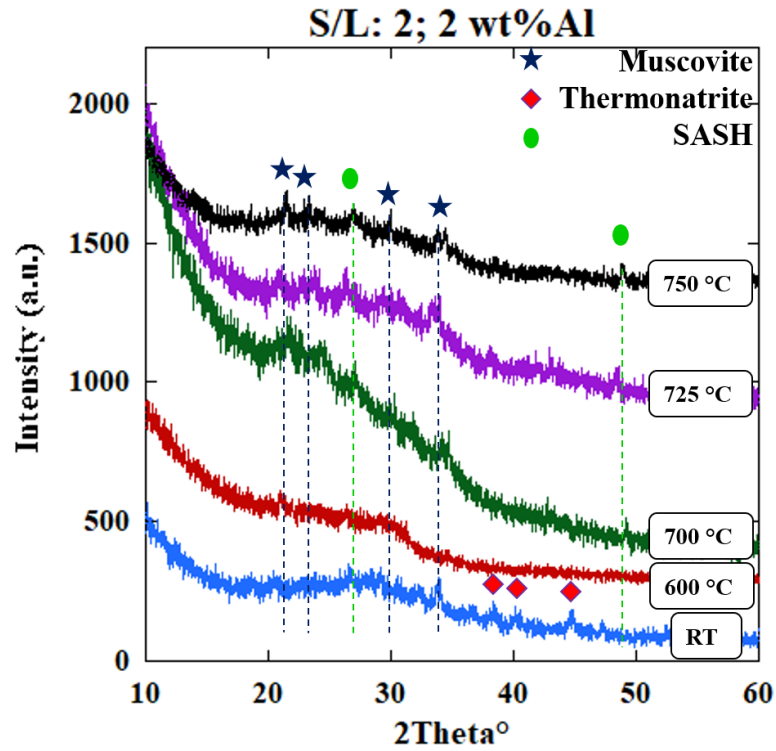


(b)



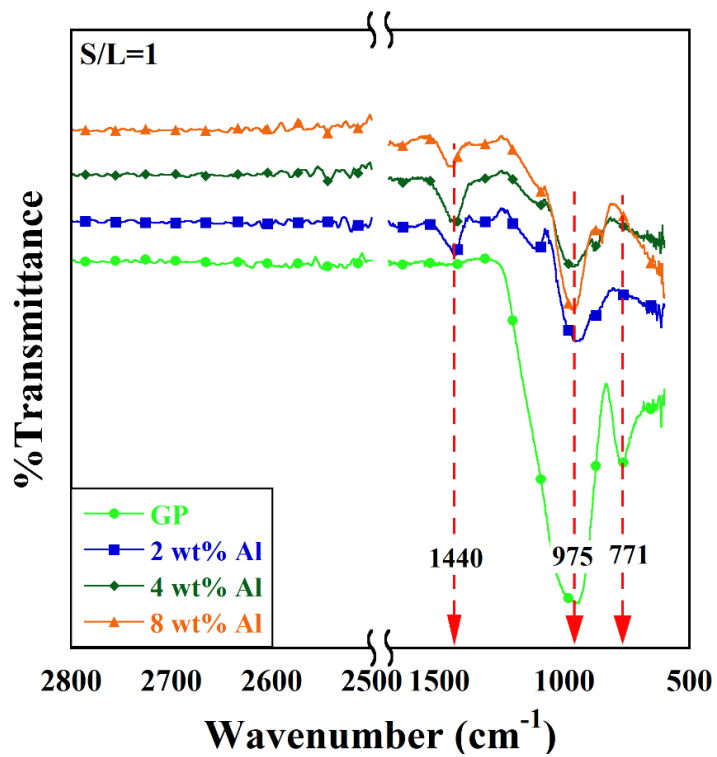
(c)

(cont. on next page)



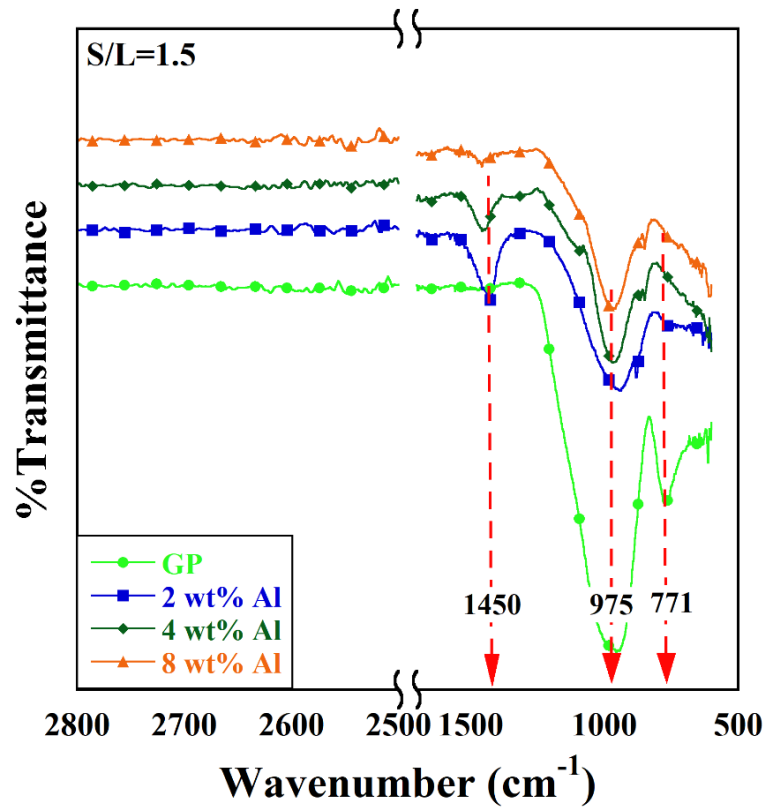
(d)

Figure 4.16. The XRD pattern of geopolymer glass foam samples (a) S/L=1, (b) S/L=1.5 and (c) S/L=2 and (d) sintered geopolymer foams

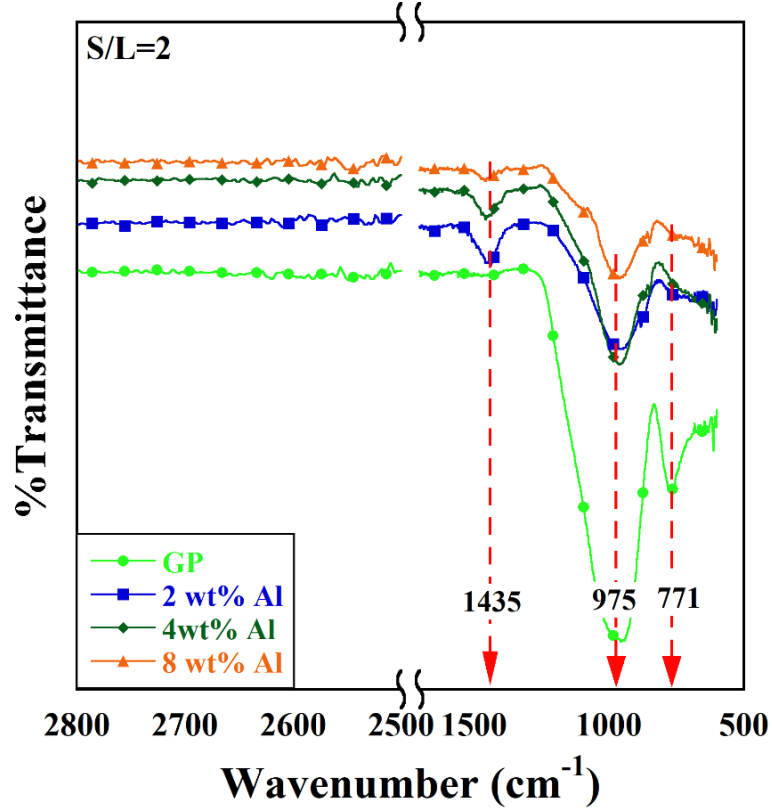


(a)

(cont. on next page)



(b)



(c)

Figure 4.17. The FTIR of geopolymer glass foam samples (a) S/L=1, (b) S/L=1.5 and (c) S/L=2

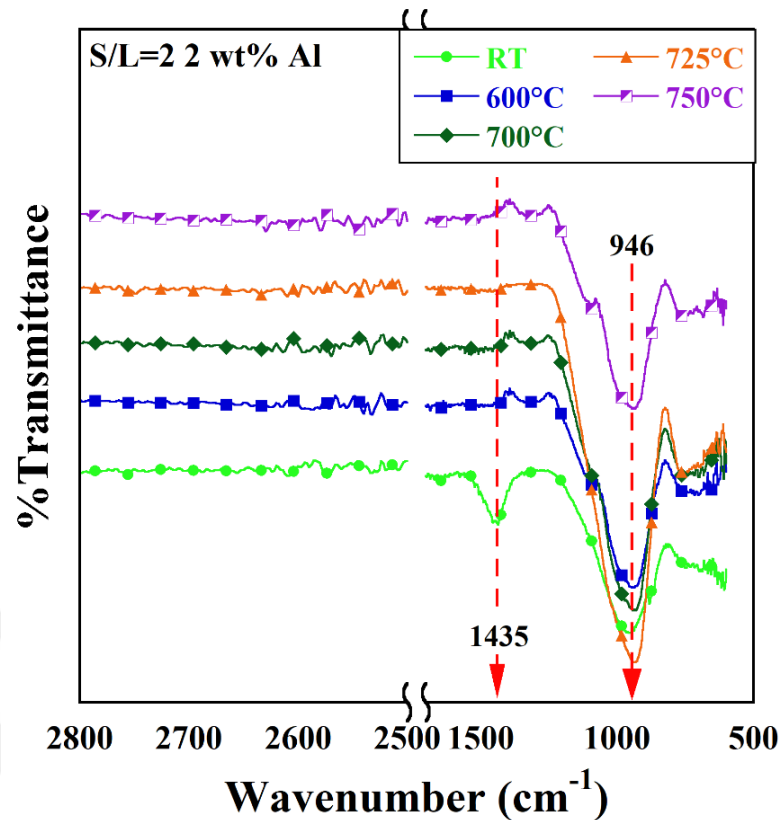


Figure 4.18. The FTIR of sintered geopolymer glass foam samples

4.6. Microscopic Analysis

The SEM micrographs of the polished cross-sections of the foamed slurries with the S/L=1 and 2 at 2 wt% Al are shown in Figures 4.19 (a-d), respectively. Figures 4.19 (a) and (c) show the particles in the foams cells and Figures 4.19 (b) and (d) in the cell walls. The black regions seen in the same micrographs are the epoxy mounting material. The varying cell sizes are clearly seen in Figures 4.19 (a) and (c). On the cell walls, large and small sizes of glass particles are seen in Figures 4.19(b) and (c) and the small glass particles are well dispersed in between large particles. The whole particles are then packed together by the geopolymer gel (Na-Al-Si). The particle packing in the foams processed with S/L=2 (Figure 4.19(d)) is however seen denser than the foams processed with S/L=1 (Figure 4.19(b)).

Higher magnification SEM micrographs of the glass particles on the cell walls are shown in Figures 4.20 (a) and (b). The geopolymer gel formation shown by arrows in the same figures is clearly seen between the glass particles. Extensive glass particle and geopolymer gel cracking are also detected, marked by an arrow in Figure 4.20(b). The

cracking is seen to intensify in the foams with $S/L=1$ and small glass particles. The cracking is due to the differences between the thermal expansion coefficients of geopolymer gel and glass particles and likely to occur during foam preparation and curing. The difference in the thermal expansion coefficients also causes the debonding of the gel as seen in Figure 4.20(a). Figure 4.21 (a) shows the elemental line scan of a glass particle and geopolymer gel around it and Figure 4.21 (b) geopolymer gel between glass particles. As is seen in both figures, the geopolymer gel contains Na, Si and Al. The cps of Na and Si are lower, while the cps of Al are higher in the geopolymer gel than in glass particles.

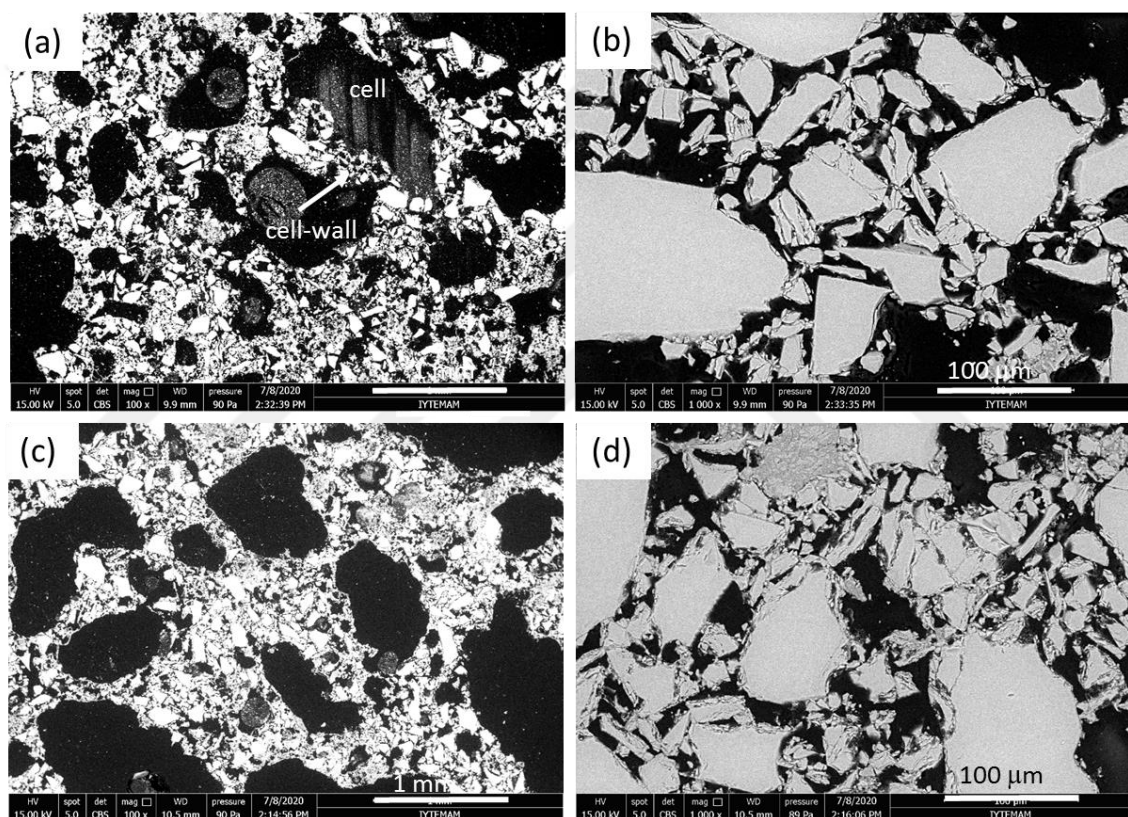


Figure 4.19. The SEM micrographs of the polished geopolymer glass foam samples with 2 wt% Al addition and the S/L ratio of (a) and (b) 1 and (c) and (d) 2 at different magnifications.

The SEM micrographs of geopolymer glass foam samples with 2 wt% Al and the S/L ratio of 1.5 and 2 are shown in Figures 4.22 (a-d) and (e-f) at 100x, 1000x, 5000x and 10000x, respectively. Cell walls and large and small pores are clearly seen at 100x magnification (Figures 4.22(a) and (e)). As the magnification increases, it becomes easier to recognize irregularly dispersed glass particles. As marked by arrows in Figure 4.22 (b)

and (f), the fracture of foams occurs at the cell walls, simply by the separation of the Na-Al-Si geopolymer phase. A close inspection of cell walls also shows that the glass particles are bonded three-dimensionally to each other (Figures 4.22 (d) and (g)). The precipitates of Na-Al-Si form a nearly continuous phase on the surfaces of glass particles (Figures 4.22 (d) and (h)). It is also noted that the particle bonding by the gel intensifies when the solid to liquid ratio is 2. Along with the increase in the growth rate, an intense precipitate formation was observed on the glass particles for both solid to liquid ratios.

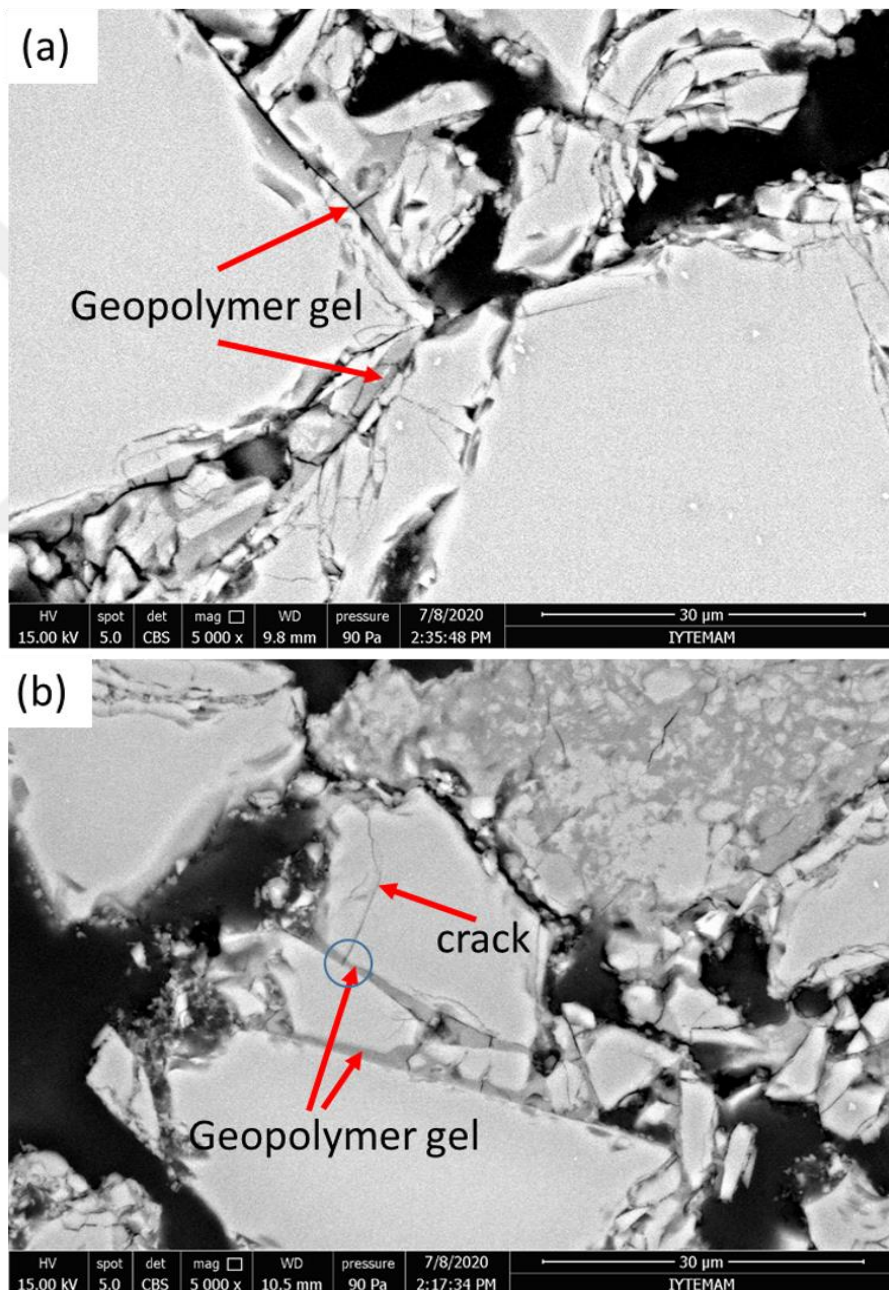


Figure 4.20. The SEM images of polished geopolymer glass foam samples with 2 wt% Al and S/L ratio (a) 1 and (b) 2

The SEM images of the fracture surfaces of the foam samples sintered at 600, 700, 725 and 750 °C are shown in Figures 4.23 (a-h), respectively. Sintering at 600 °C seems to have no effect on the cell structure of foams as seen in Figure 4.23 (a) and (b), while glass particles are seen to be partially sintered at 700 °C, forming nearly a foam cell structure (Figure 4.23 (c) and (d)). As the sintering temperature increases to 725 °C, a typical foam cell structure starts to appear (Figures 4.23 (e) and (f)). At 750 °C, a complete foam structure with a reduced number of pores on the cell walls is observed (Figures 4.23 (g) and (h)). In addition to these, sintering between glass particles is starkly noticeable when the magnification comes 10000x in Figure 4.24 (a), and (b). Acicular structures are found in the samples that are sintered at 725 and 750 °C as shown in Figures 4.24 (c and d).

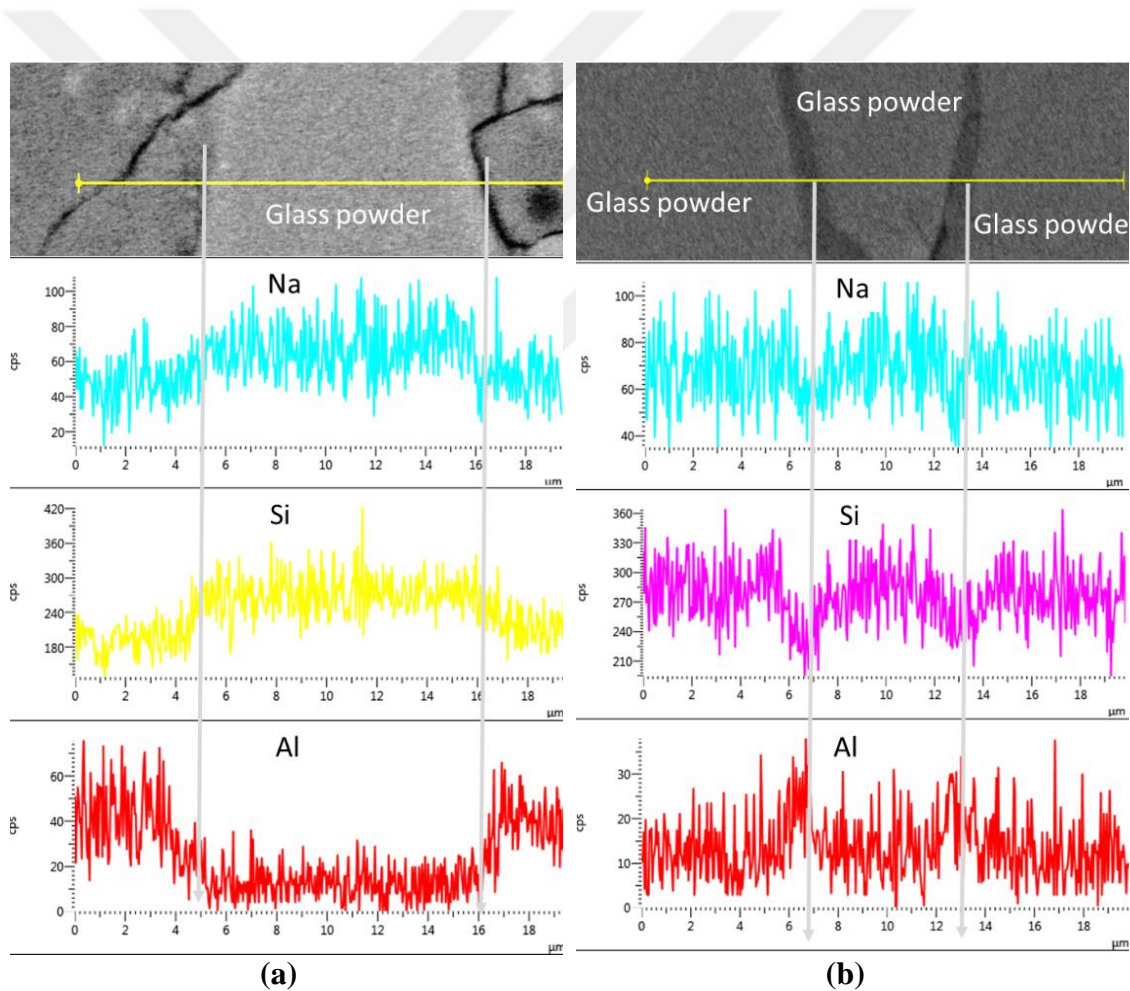


Figure 4.21. The results of EDX Line Scan Analysis of the foams samples with 2 wt% Al and the S/L ratio of (a) 1 and (b) 2.

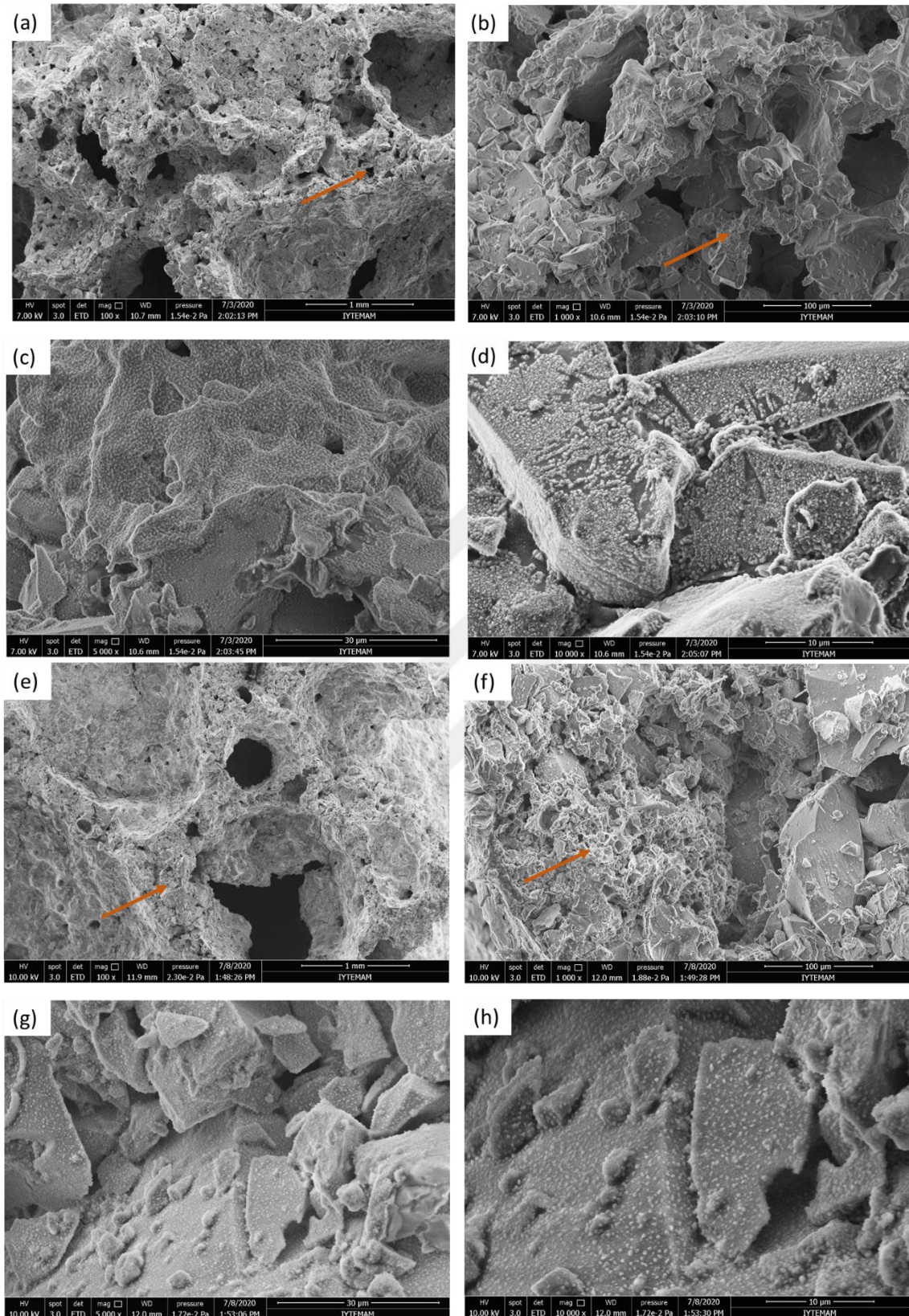


Figure 4.22. The SEM images of geopolymer glass foams' fracture surface with 2 wt% Al and S/L ratio 1.5: the magnification (a) 100x, (b)1000x, (c)5000x and (d)10000X and S/L ratio 2 at e)100x, (f) 1000x, (g) 5000x and (h) 10000x

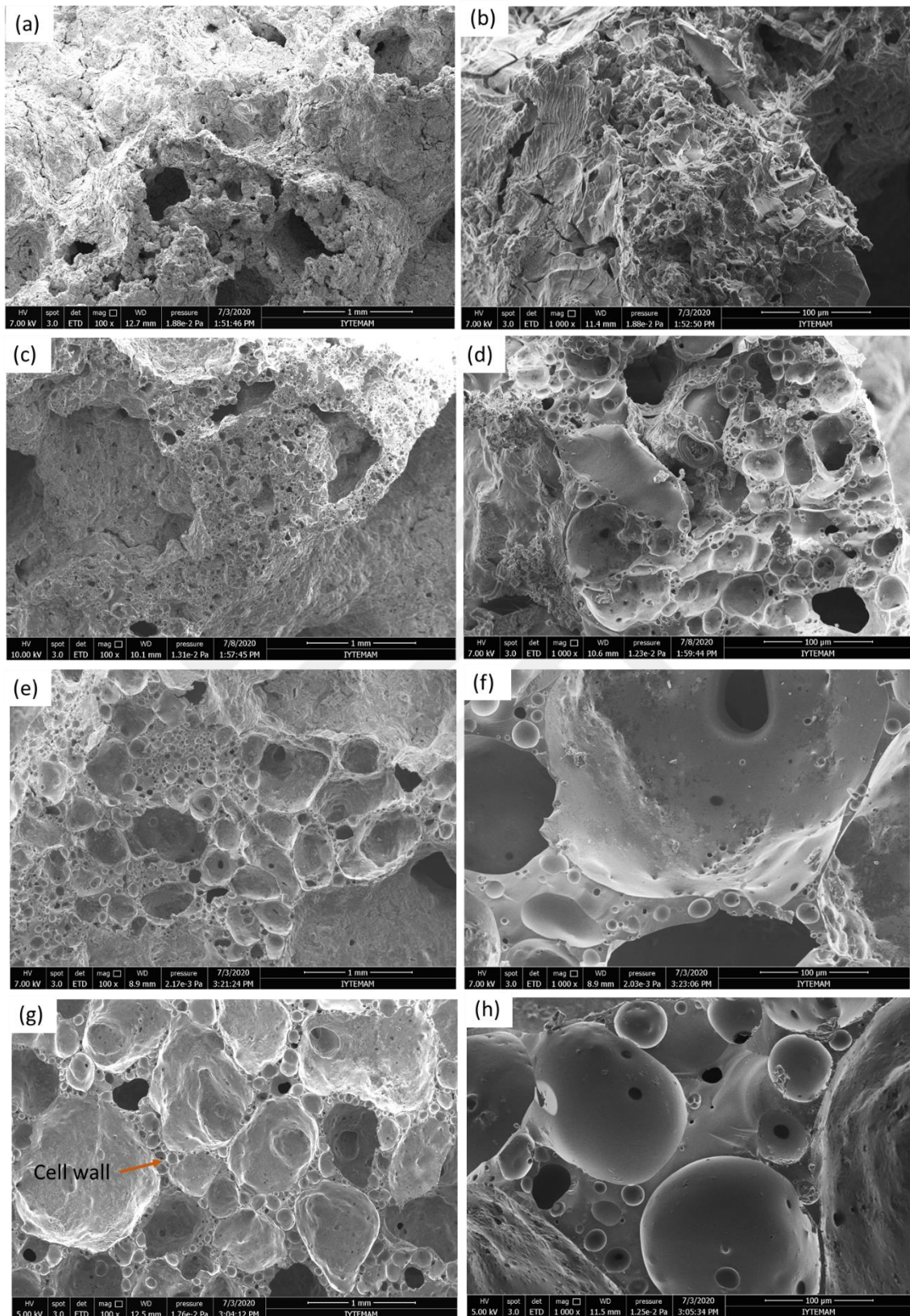


Figure 4.23. The SEM image of fracture surface of geopolymer glass foams sintered at (a) and (b) 600, (c) and (d) 700, (e) and (f) 725, and (g) and (h) 750 °C in 100x and 1000x magnification, respectively.

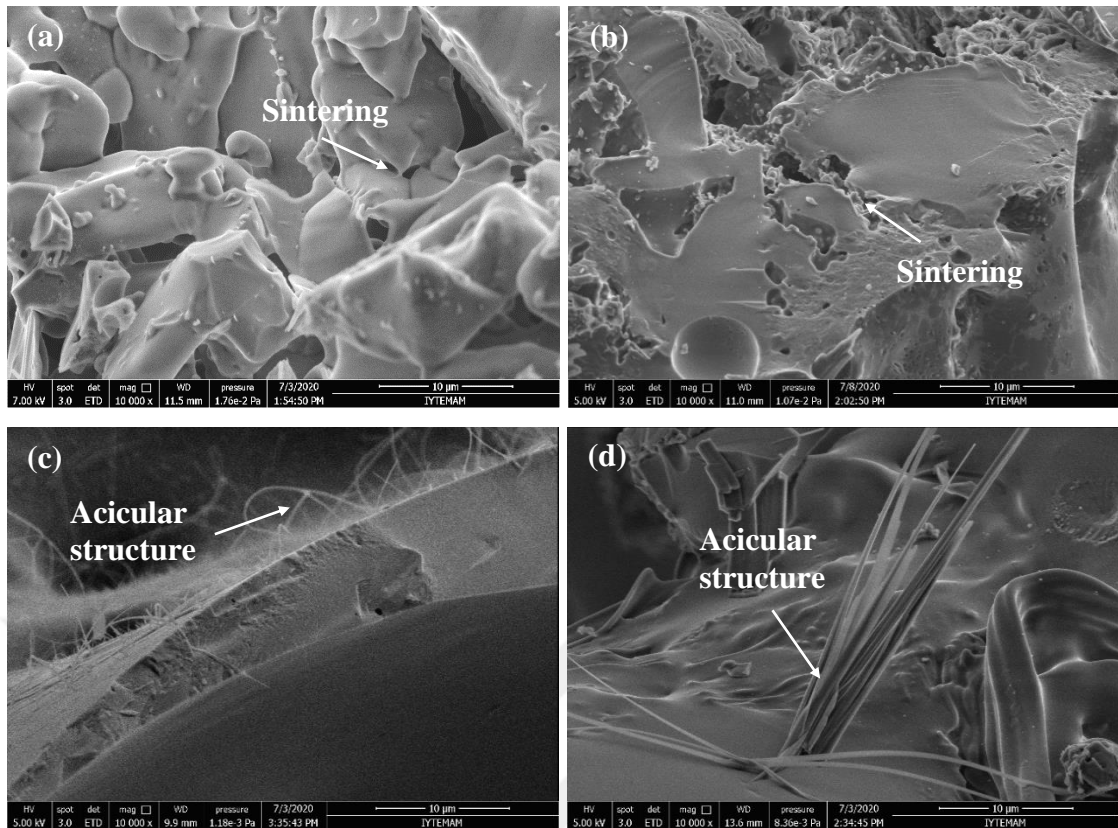


Figure 4.24. The SEM images of the fracture surfaces of geopolymers glass foams sintered at (a) 600, (b) 700, (c) 725, and (d) 750 °C in 10000x magnification.

CHAPTER 5

DISCUSSIONS

5.1. The Expansion of Slurries

The expansion of the geopolymer slurries may be controlled by both the H₂ gas release rate and the geopolymerization reaction rate. The representative expansion-time and temperature-time curve of the studied geopolymer slurries (S/L=1 and 4 wt% Al) are shown in Figure 5.1(a). Three important regions in the same figure are noted. These are (i) a rapid expansion, region 1, (ii) initial peak expansion, region 2 and (iii) constant expansion, region 3 (the maximum expansion). The temperature of the slurry increases gradually at the beginning of region 1; then, rises abruptly to a maximum value at the end of region. Note that after maximum expansion, the temperature of the slurry gradually decreases in region 3. The rapid rise of slurry expansion in region 1 is explained by the following reactions ⁵⁸,

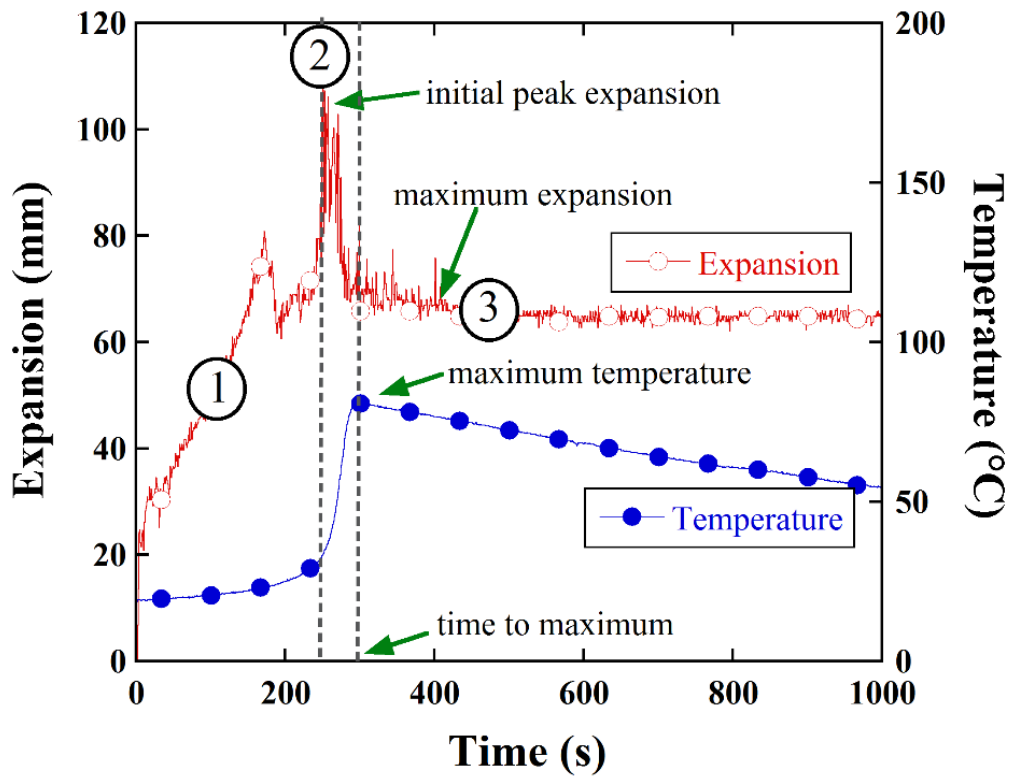


Reaction 1 is exothermic, occurring spontaneously at room temperature with the H₂ generation. The H₂ generation is controlled by the NaOH/Al molar ratio in reaction 1 and 2. If the ratio is lower than the stoichiometric ratio, ~1.5, a slower H₂ generation occurs ⁵⁸. The reaction rate also increases when the initial (starting) temperature of NaOH solution increases ⁵⁹. In the presence of a sufficient amount of NaOH in the environment, the H₂ generation reaction rate is controlled by the amount of Al ⁶⁴. Al reacts with water and releases H₂ bubbles by the nucleation and diffusion. Nucleation is the first step; afterward, bubbles grow with the diffusion of gases. Growing gas bubbles combine with other resulting in coarsening. The high pressure in the bubbles during the nucleation stage results in a sudden expansion of slurries, which corresponds to the initial peak expansion in Figure 5.1(a). After that, coarser gas bubbles are broken down by the combined effect of hydrodynamic forces and the gas and liquid pressures at a certain bubble radius ^{65, 66}.

Balancing occurs with an increase in the viscosity of slurries. The geopolymerization reaction takes place almost simultaneously with the H₂ generation reaction. Aluminates form as a result of a reaction (1) and (2) and combine with the existing silicates (Si-O) to form the geopolymer gel. The gel formation further increases the viscosity. The final structure of geopolymer foam is obtained as a result of the reorganization of this gel³⁶. A constant expansion seen in region 3 is presumed to be due to the completion of the geopolymerization reaction. The temperature of geopolymer slurry is likely to be related to the amount of Al added. Since hydrogen generation reaction is exothermic⁵⁸, the temperature of the slurry is expected to increase with increasing the Al content. As is shown by a dotted line in Figure 5.1(a), the temperature reaches a maximum just after the drop of the expansion from an initial peak expansion to a constant (maximum expansion) expansion. After the maximum temperature, no expansion occurs and the slurry begins to cool down to room temperature. This confirms that Al reaction with NaOH terminates near the maximum temperature. The temperature rise was also reported with increasing Al addition in a constant amount of NaOH solution⁶⁴. A similar result was obtained; increasing Al content increased the temperature of the geopolymer slurries until about a saturation temperature between 95-100 °C. The maximum temperature of the slurries with the maximum Al addition is about 90 °C in (Figures 4.4, 4.5, 4.6 and 4.7). The difference between the literature and the present study may be due to the fact that the temperature of the slurry in the present study was measured at the bottom of the foaming cylinder. The temperature at the top is expected to be higher than the bottom as gases move upward. The condensed matter at the surface of the foaming cylinder also confirms the evaporation of water in the slurry during rapid expansion. An increase in the temperature increases both the rate evaporation of water and the geopolymerization reaction. The first results in an increase of S/L ratio and the second an increase of viscosity of the slurry. Both cause the solidification of the slurry. The geopolymer reaction is therefore presumed to terminate at the beginning of the constant expansion region. Figure 5.1(b) shows the variation of the time to maximum temperature and maximum temperature as a function of Al content at different S/L ratios. As is seen in the same figure, the time to maximum temperature saturates when the slurry temperature reaches ~90 °C for coarse powder slurries at about 8 wt% Al. For fine powder slurries, the maximum temperature reaches 85 °C, and the time to expansion saturates at about 16 wt% Al. The time to maximum temperature is however should be approached carefully as the hydrogen evolution is very

rapid in the slurries with a high amount of Al addition. Even in the mixing stage, the foaming maybe therefore started. Nonetheless, Figure 5.1 (b) shows a general trend of the solidification time of the geopolymer foam. The solidification occurs at about 400 s at Al contents of 8 wt% regardless of the S/L content for coarse powder slurries.

Coarser particles with a low the S/L ratio result in lower viscosities due to lesser inter-particle interaction^{67,68}, leading to higher slurry expansion as seen in Figure 4.8(b). On other hand, a negligible effect of particle size is seen on the maximum temperature in Figure 4.8(a) because the temperature is merely related to the H₂ evolution reaction.



(a)

(cont. on next page)

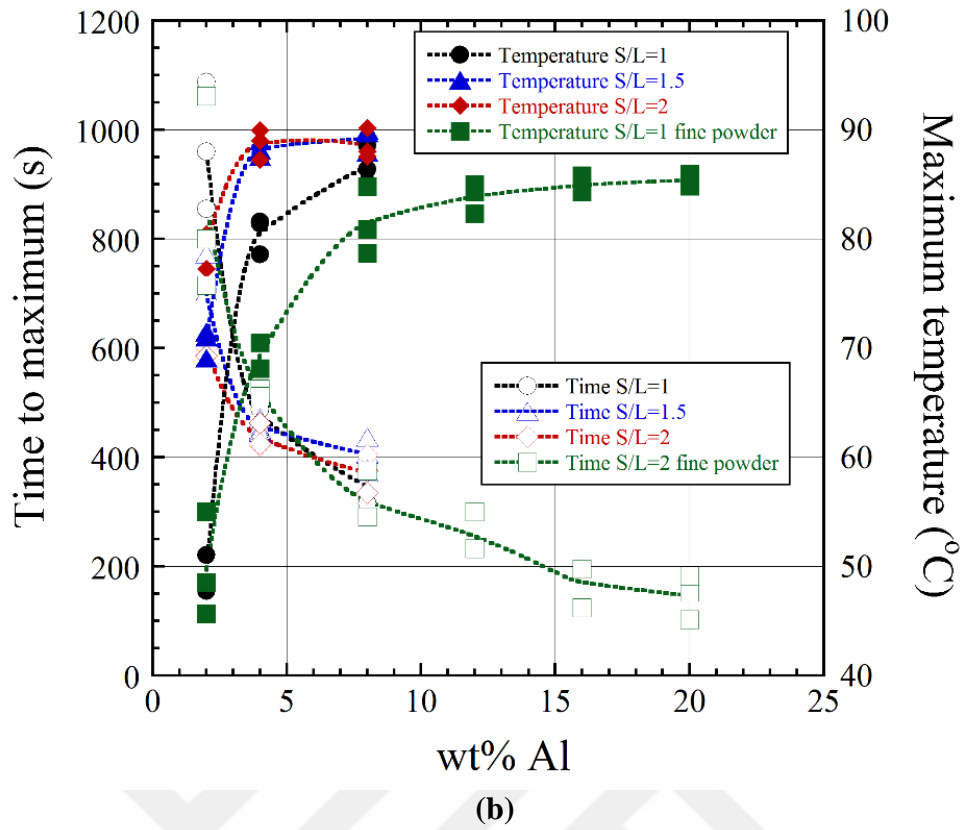
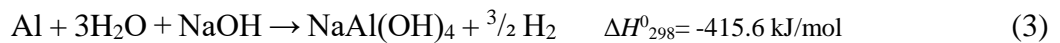


Figure 5.1. (a) Typical expansion-time and temperature-time curves of geopolymers slurries and (b) time to maximum temperature and maximum temperature

The temperatures of the slurries are altered by the solid/liquid ratio. As the S/L ratio increases, the amount of NaOH in the slurry decreases proportionally in Table 3.2. As the amount of NaOH decreases, the temperature increases (Figure 4.9(b)). The reactions relating the hydrogen evolution are as follows⁶⁹,



The NaOH in the slurry is consumed by the reaction 3, while the reaction 4 is triggered when the amount of NaAl(OH)₄ reaches a super saturation in an environment with a small amount of NaOH. The reaction 5 is the net reaction. An increase in the Al content is therefore expected to increase the temperature of the slurry at a constant amount of

NaOH and S/L ratio based on the reaction 5. However, the opposite happens when NaOH is supplied to the environment in a sufficient amount. In that case, the reaction 4 is not triggered because $\text{NaAl}(\text{OH})_4$ does not reach the saturation concentration⁶⁹. In this circumstance, the Al content has a limiting effect and the reaction finishes at lower temperatures. Although increasing the amount of Al increases the temperature at a constant S/L ratio, the boiling point of water has a limiting effect on the temperature of slurries (Figure 4.9 (b)).

The volume expansion is also affected by the S/L ratio. The change of the S/L ratios causes a change in the relative viscosity, as the solid fraction of the slurry increases relative viscosity⁶⁸. At the lowest S/L ratio (S/L=1), the viscosity is not sufficient to form a stable foamy structure. The slurries with S/L = 1 and 2 wt% of Al collapse for this reason (Figure 4.9 (a)). At the highest S/L ratio (S/L=2), the slurry is too thick for foaming. Excessive increase in the viscosity makes the flow of the slurry difficult. This adversely affects slurry expansion because the gas/liquid ratio is distorted due to pressure inequality. As the internal pressure increases, bubbles diameter increases. And, therefore the increase in internal pressure should be balanced by an external force^{65, 70, 71}. This is also seen in the present study, the slurries with the S/L ratio of 2 display less expansion than the slurries with the S/L ratio of 1.5 (Figure 4.9 (a)). The final density of foams generally behaves inversely with volume expansion, which is also valid for S/L=1.5 and 2 slurries. On the other hand, an outlier behavior was found when S/L=1 (Figure 4.9 (c)). A higher extent of foam collapse after the initial peak expansion occurs when S/L=1 because of low viscosity affecting the foam stabilization adversely.

Contrary to the previous studies in which the foam density increased as the sintering temperature increased⁵², the present study showed a reverse effect. The geopolymer foams processed with S/L=2 and 2 wt% Al has a mean density of 456 kg m^{-3} , while the mean densities of the geopolymer foams are 513, 445, and 381 kg m^{-3} after being sintered at 600, 700, and 750 °C, respectively. This indicated that the partial melting of glass particles started after about 700 °C. The geopolymer foam sample dimensions changed during sintering after 700 °C. Although the diameter and height of geopolymer foam stay almost the same with the unsintered one when sintered at 600 °C, the diameter of foams increases and the height decreases when sintered at 700 and 750 °C as seen in Figures 5.3 (a-c). When the sintering temperature is 600 °C, strong bonds are not formed between the glass particles⁹, so despite its high density, it shows lower strength as shown

in Figure 4.14. When the sintering temperature is 750 ° C, the glass particles are semi-melted and diffuse each other (Figure 5.3 (d)). The sintering of glass particles provides compactness. The reduction of foam density with sintering is due to the following reaction



Above reaction releases CO₂ which results in small bubble formation on the cell edges when glass particles are in a semi-melt state (see Figure 5.2). The above reaction is caused by the decomposition of thermonitrite and CMC. Na₂CO₃ is especially used as a foaming agent at high temperatures based on the reaction 6⁷². The sintering, therefore, provides both compactnesses by bonding glass particles and reduced the density by the formation of small pores on the cell edges. Therefore, while sintered geopolymer foam at 750 °C has the lowest density, this foam also has a relatively higher strength than other sintered geopolymer foam.

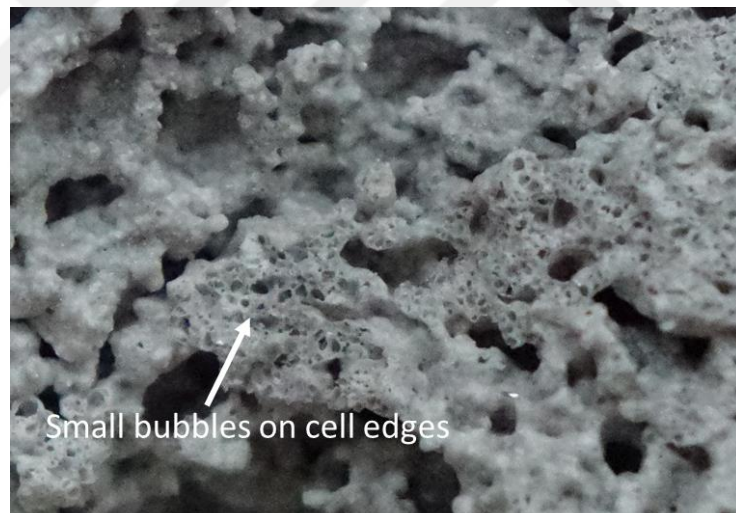


Figure 5.2. The image of geopolymer foam cells after sintering

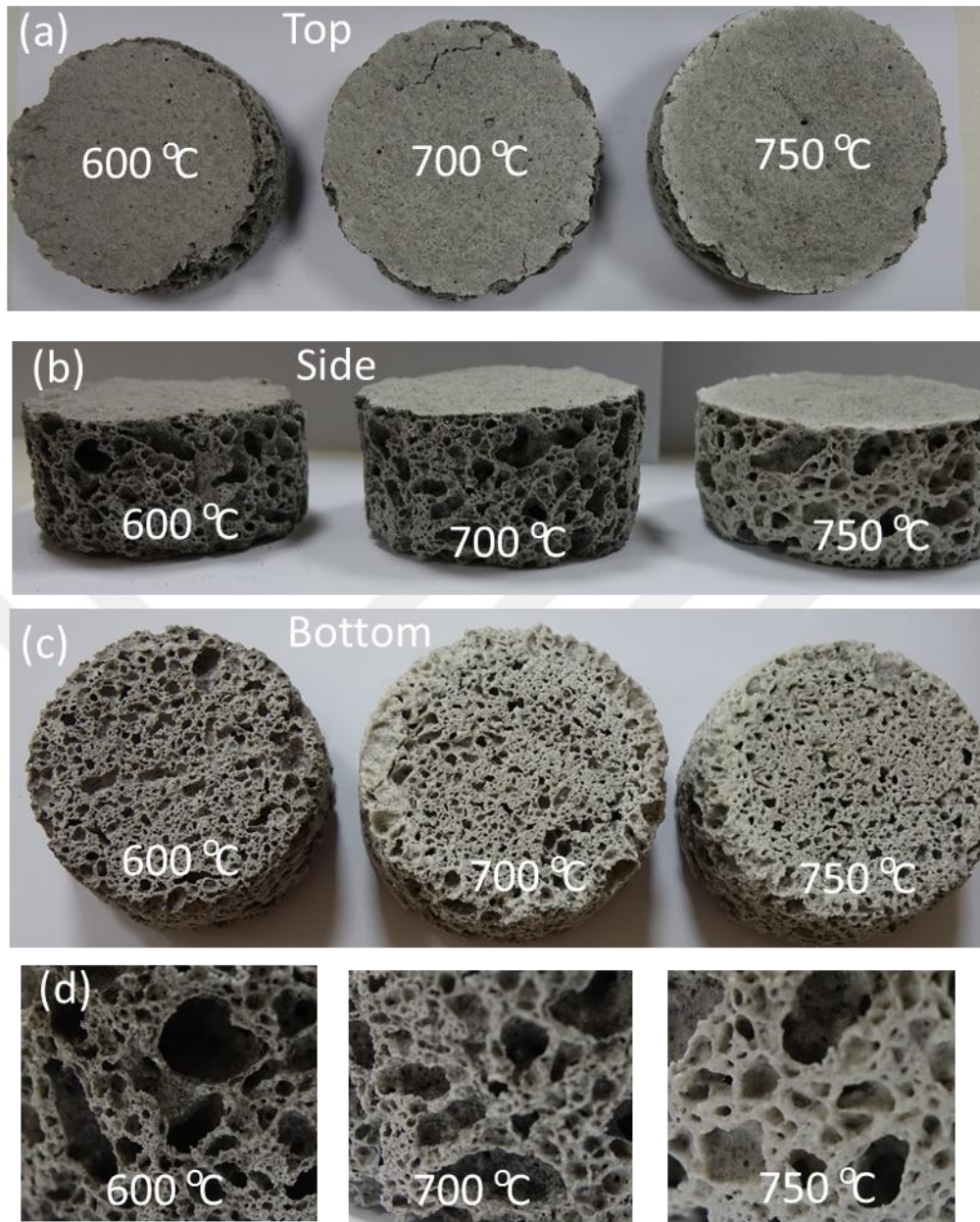


Figure 5.3. The images of sintered geopolymer foams at different temperature (a) top, (b) side, (c) bottom and (d) magnified image showing cell structure

5.2 Compressive Strength

Brittle foams crush under compressive forces by a mechanism merely involving cell (edge or wall) fracture⁷³. A cubic close cell foam structure is shown in Figure 5.4. The applied force induces two fracture sides on a cell edge (beam). Based on the fracture

of beams, the compressive fracture strength of brittle foams (σ_f) was proposed to follow the following equation⁷³

$$\sigma_f = \sigma_s [C(\varphi \rho_{rel})^{\frac{3}{2}} + (1 - \varphi) \rho_{rel}] \quad (1)$$

where σ_s is the strength of cell wall material and the fracture strength of glass is given 70 MPa in present study³¹. C is a constant (0.2⁷³) and ρ_{rel} is the relative density of foam ($\frac{\bar{\rho}}{\rho_s}$, where $\bar{\rho}$ is the density of the foam and ρ_s is the density of the solid) and φ is the volume fraction of the solids contained on plateau borders (see inset of Figure 5.4). The first term in Eqn.1 is due to the bending of cell edges and the second term is due to the membrane stretching of cell walls. Eqn. 1 predicts the compressive strengths of open-cell foams when φ equals to 1 and the compressive strengths of closed-cell foams when φ equals to 0. The value of φ is given as⁷³

$$\varphi = 1 - \frac{3t(l - 2W_p)^2 + 6t\sqrt{3}(l - (2/\sqrt{3})W_p)^2}{11.31l^3\rho_{rel}} \quad (2)$$

where l , W_p , and t are the cell wall length, plateau border thickness and cell wall thickness, respectively (Figure 5.4).

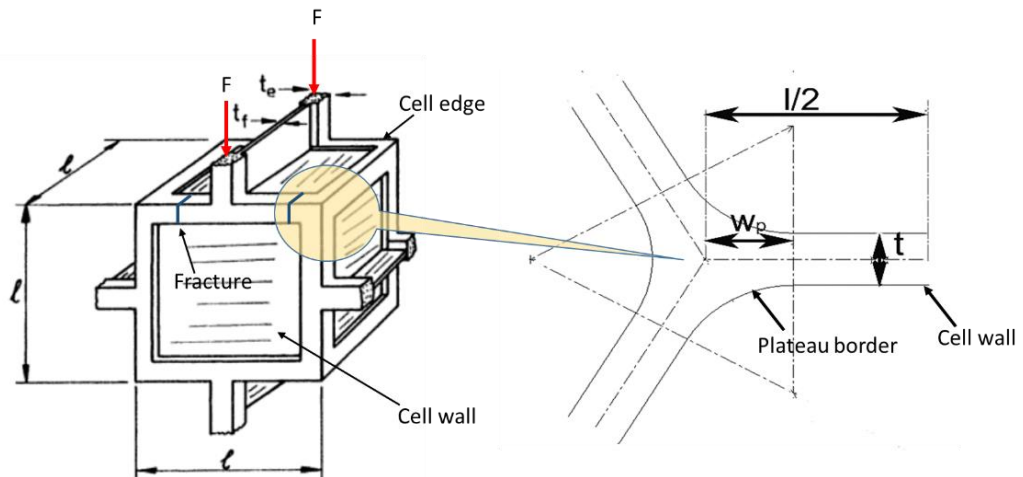


Figure 5.4. The cubic closed cell foam structure showing the fracture sides on the cell edge and the geometry of the cross-section of a tetrakaidecahedral cell edge with plateau borders.

(Source: Gibson et al., 1997)

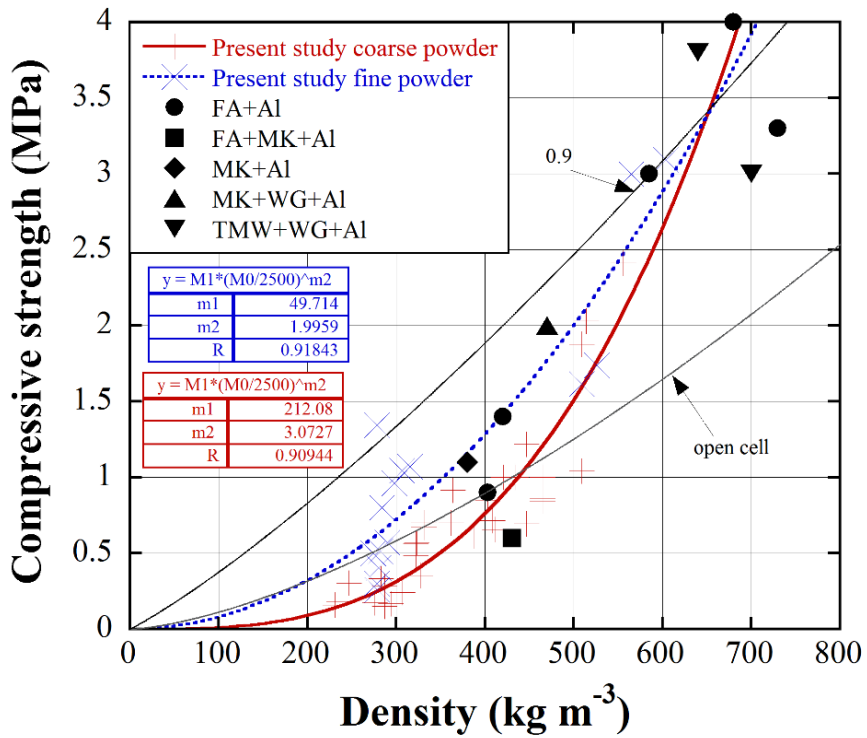
Both the geopolymer and sintered geopolymer foams investigated in the present study failed by a brittle fracture mode (Figures 4.15(a-d)). For comparison, the compressive strengths of the prepared geopolymer foams and the compressive strengths of previously investigated geopolymer foams processed using Al^{2, 6, 46, 49, 51, 55, 56, 62, 74-77} and H₂O₂^{8, 54, 55, 61, 78-84} foaming agents are shown, as a function of foam density in Figure 5.5 (a) and (b), respectively. In the same figure, the compressive strength predictions are based on Eqn.1 for $\varphi = 1$ and $\varphi = 0.9$ are also shown for comparison. The compressive strengths of geopolymer foams are clearly seen in Figures 5.5 (a) and (b) approach the compressive strengths of open-cell glass foams. The compressive strength of the prepared geopolymer foams is also comparable with those of previous studies. As it is noted in Figure 5.5 (b) after about 500 kg m⁻³, the compressive strengths of geopolymer foams display a different tendency with density. In order to account for this trend, the compressive strength fine and coarse powder geopolymer foams are fitted with the following power-law relation,

$$\sigma_f = A\rho_{rel}^n \quad (3)$$

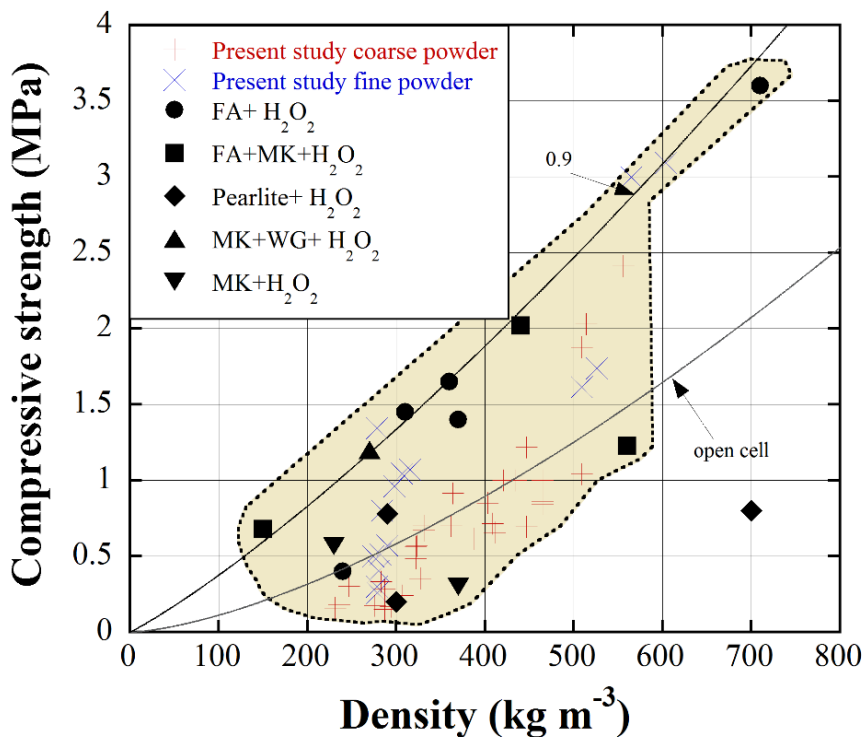
where A is a constant and n is the exponential term which relates relative density to strength. The results of fitting Eqn. 2 with the compressive strengths of the present geopolymer foams are shown in the inset of Figure 5.5(a). The value of n is found 2 and 3 for fine and coarse powder geopolymer foams, respectively. Also, Eqn. 2 fits well with the experimental compressive strength of the prepared coarse powder geopolymer foams.

By comparing Figure 5.5 (a) with Figure 5.5 (b), one can also tend to conclude that the foams prepared using H₂O₂ foaming agent exhibit higher compressive strengths than the foams prepared using Al foaming agent at the densities around 400 kg m⁻³. The compressive strengths of the present and previous geopolymer foams in Figures 5.5 (a) and (b) approximately range 0.2-4 MPa between 150 and 800 kg m⁻³. The compressive strengths of the geopolymer and sintered geopolymer foams are shown as a function of density, together with the previously investigated glass foams^{16, 22, 28, 63, 85-96} in Figure 5.6. The compressive strengths of the reported glass foams are well fitted with φ values between 0.7 and 1 for the foam densities up to 300 kg m⁻³ and φ values between 0.7 and 0.9 for the foam densities between 300 and 600 kg m⁻³ (Figure 5.6). The glass foams also tend to show open cell glass foam behaviour at low densities. The compressive strengths

of geopolymer foams sintered at 750 °C fall on the lower range of compressive strengths of previous studies at about 400 kg m⁻³.



(a)



(b)

Figure 5.5. The variations of the compressive strength with the density for (a) present study and (b) the previous glass foam study and present study

The tested present geopolymer foam samples show however lower compressive strength than those of previously studied glass foams. One of the reasons for that is that the cell edges and walls in geopolymer foams contain pores in between the glass powder particles (Figures 4.19(a-d)). The pores in the cell edges and walls tend to weaken the compressive strength by forming high-stress concentration sites.

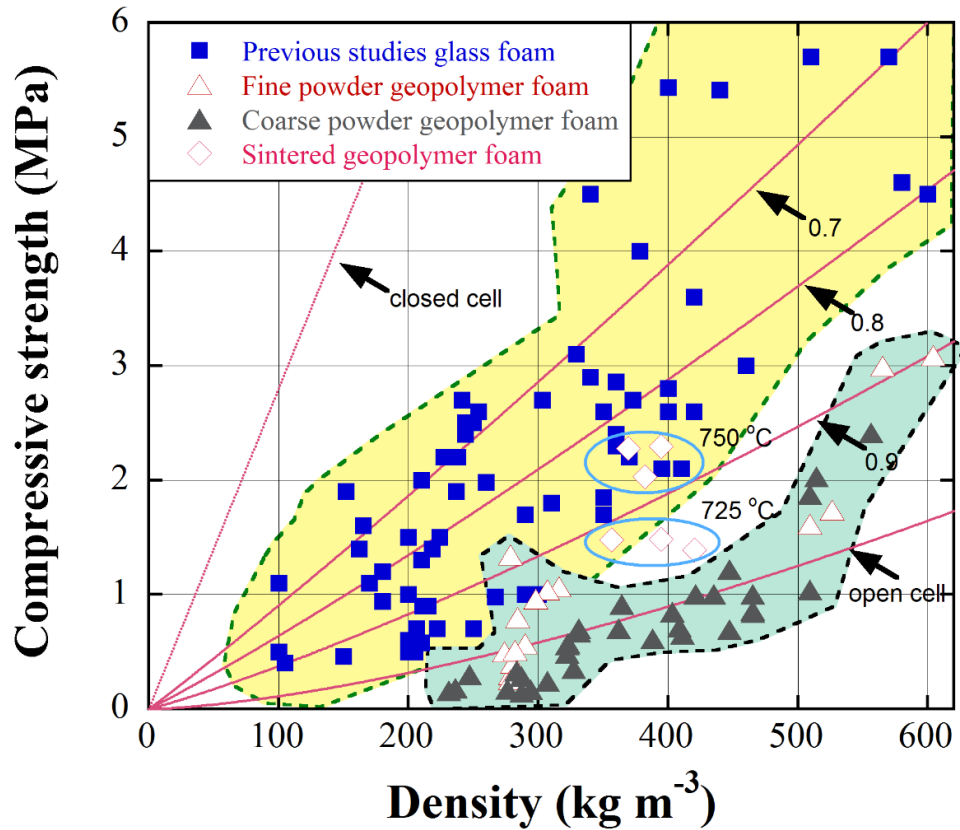


Figure 5.6. The variations of the compressive strengths of geopolymer and sintered foams and the compressive strength of previously investigated glass foams

5.3. Thermal Conductivity

The variations of the thermal conductivities of the prepared geopolymer and sintered geopolymers at 750 °C with density are shown in Figure 5.7 together with those of previously investigated geopolymer foams and glass foams ^{16, 88, 94, 97-99}. The thermal conductivities of the prepared geopolymer and sintered geopolymer foams are comparable with reported values of the thermal conductivities of similar foams. However, glass foams exhibit higher thermal conductivities than geopolymer foams at high densities. It is also seen that the starting silica raw material has an effect on the thermal

conductivities. The slurries containing WG, basically, show lower thermal conductivity as seen in Figure 5.7.

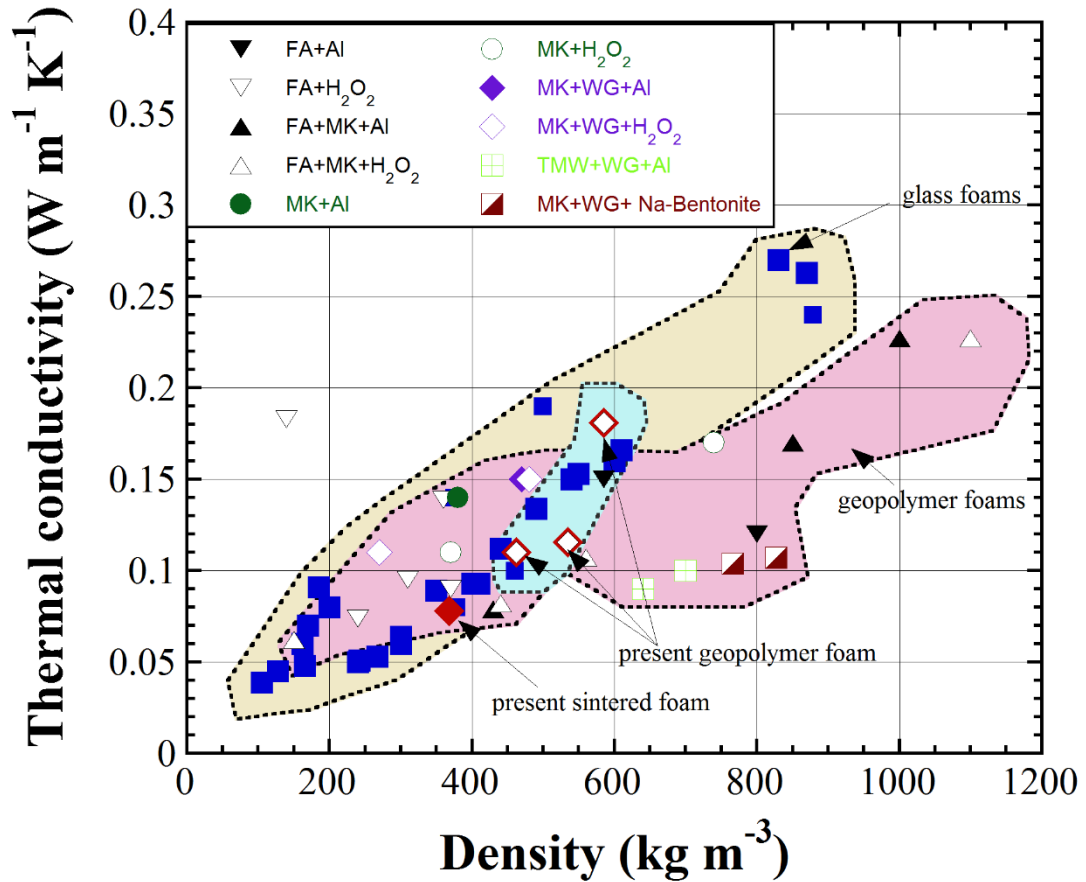


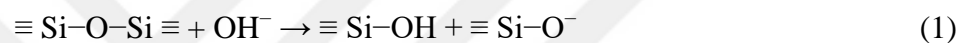
Figure 5.7. The variations of the thermal conductivity with the density of the geopolymer glass foams of previous and present study

5.4. XRD and FTIR Analysis

Although the used WG powder has an amorphous structure, the prepared geopolymer foams have crystalline phases. This is expected as geopolymer crystallization takes place below 100 °C, even in the foaming stage³⁵. Geopolymer foams may have amorphous or semi-crystalline structure, depending on the network between Si-Al formed during the geopolymerization reaction⁵². In Figure 4.16 (a-d), the peak intensity is quite low for all S/L ratios, showing low crystallinity⁴⁹. Thermonitrite formation is detected at all S/L ratios (Figures 4.16 (a-c)). Thermonitrite is generally formed by the atmospheric carbonation of NaOH⁴⁸. The use of a carbonate-based binder (CMC) in the present study

further intensified the formation of thermonitrite. Sintering at a high temperature however resulted in the decomposition of thermonitrite. Muscovite and sodium aluminum silicate hydrate (SASH) are low-intensity geopolymer crystalline phases. The appearance of these two different crystalline phases depends on the amount of oxygen³⁵. The appearance of SASH peaks in low S/L ratio foams is due to the lower oxygen content of these slurries. At the same time, sintering in an open atmosphere promotes the muscovite formation (Figure 4.16 (d)).

The FTIR spectra provide much information regarding geopolymerization reactions (Figure 4.17(a-c) and Figure 4.18). The characteristic bonds of WG powder are located at 975 and 771 cm⁻¹. After the geopolymerization reaction and formation of a gel network, the Si-O bond at 771 cm⁻¹ disappears. The bonds that exist in these two wavenumbers are decomposed by the reactions in the alkaline medium¹⁰⁰ as



Thereafter, Si-O-Al band formation with Al occurs at around 1000 cm⁻¹⁵². Due to the formation of aluminosilicate gel, Si-O-Al bond formation shifts to around 975 cm⁻¹ at all S/L ratios and Al amounts. This indicates that the FTIR spectra do not change depending on S/L ratio². The intensity of the band is related to the participation of water in a reaction which means non-bridging oxygen enhancement⁴⁸. As the alkaline amount increases, the main bond shifts towards smaller wavenumbers. This is due to the increase in the number of silicon sides with non-bridging oxygen balanced by sodium cations. In addition, the increase of alumina in the structure reduces the wavenumber because of enhancing the silicate network containing tetrahedral Al⁴⁹.

The highest shift seen in the geopolymer foams containing 2 wt% Al (Figures 4.17 (a-c)) is explained by the shift of wavenumber back to higher wavenumber with the increase of Si participating in the geopolymerization reaction⁴⁸. The increment Si in the reaction may have been higher as the amount of reacted Al increased. When Figure 4.18 is examined, it is seen that the wavenumber shifts up to 946 cm⁻¹ in the sintered geopolymer foams. In these cases, the participation of Al in geopolymerization has increased. In addition, there is an extra peak that is not seen in glass powder but seen in all geopolymer foams in Figure 4.17 (a-c). This peak seen at 1440 cm⁻¹ is the result of the carbonation reaction. It is formed as a result of the reaction between CO₂ and geopolymer,

which is generally called atmospheric carbonation ^{52, 101}. It is also formed as a result of the reaction of CMC used as a binder in this study with an alkaline solution in the geopolymer. These bonds disappear in the sintered geopolymer foams. This situation is thought to be for the same reason as the expansion of sintered geopolymer foams. In other words, it is decomposed by the effect of temperature and released as CO₂ gas.



CHAPTER 6

CONCLUSIONS

The effect of WG powder size (23 and 72 μm), solid/liquid ratio ($S/L=1, 1.5$ and 2) and Al foaming agent content (2-20 wt%) on the linear expansion and temperature of the geopolymer slurries was investigated. In addition, the compression mechanical behavior, thermal conductivities and microstructure of the foamed glass powder slurries were determined. Geopolymer glass foams were prepared at room temperature using a solution of NaOH (8M), sodium silicate (10% NaOH and 27% SiO_2) and CMC (3 wt%). The linear expansions and temperatures of the foaming slurries were measured in-situ using a laser distance meter and thermocouple, respectively. Geopolymer glass foams containing $S/L=2$ and 2 wt% Al were further sintered at 600, 700, 725 and 750 $^\circ\text{C}$ in order to investigate the possibility of forming a glass foam structure at the temperatures lower than the foaming temperatures (750-950 $^\circ\text{C}$) of conventional glass foam processing.

The expansions and temperatures of the foaming slurries initially increased sharply; thereafter, the expansion reached a constant value after an initial peak expansion, while the temperature showed a maximum (maximum temperature). The constant slurry expansion after about the maximum temperature confirmed the termination of the reaction between Al and NaOH in the geopolymer solution. The maximum temperature increased with increasing Al addition up to a saturation temperature. The saturation temperature was determined ~ 90 $^\circ\text{C}$ for the coarse powder slurries at 8 wt% Al and ~ 85 $^\circ\text{C}$ for the fine powder slurries at 16 wt% Al. The time to maximum temperature correlated with the solidification time of the geopolymer foam. The higher the maximum temperature, the higher the geopolymerization reaction rate due to the increase of viscosity. The maximum temperature was also found to be related with the S/L ratios. The maximum temperature increased from 50 to 80 $^\circ\text{C}$ in 2 wt% Al containing slurries when the S/L ratio increased from 1 to 2. Both, the evaporation of water at the saturation temperature and the increase of the S/L ratios of the slurries caused the solidification of the slurry.

In general, as the Al content increased, the final density of the geopolymer foams decreased. The coarse powder slurries resulted in lower final densities than the fine powder slurries, 240 and 530 kg m^{-3} between 2 and 8 wt% Al. The final densities of the

fine powder slurries were 280 and 530 kg m⁻³ between 2 and 20 wt% Al, respectively. The partial melting of glass particles was determined to start after about 700 °C and sintering above this temperature resulted in a reduction in the density of the sintered foams. The reduced density of the sintered foams above 700 °C was ascribed to the CO₂ release by the decomposition reaction of thermonitrite, which was also confirmed by the XRD and FTIR analysis. The sintering provided both compactness by bonding glass particles and lightness by forming additional pores on the cell edges. Because of this, the geopolymer foams sintered at 750 °C had the lowest density and the highest strength.

Muscovite and sodium aluminum silicate hydrate (SASH) were found as low-intensity geopolymer crystalline phases in addition to thermonitrite in the present geopolymer foams. The increased S/L ratio and sintering promoted the presence of muscovite. These were also confirmed by XRD and FTIR analysis.

Both the compressive strengths and thermal conductivities of geopolymer foams varied with the final density. The compressive strength was found between 0.2 and 2.4 MPa, between 230 and 560 kg m⁻³. The foams prepared by using fine powder slurries showed higher compressive strength than the foams prepared by using coarse powder slurries. Geopolymer coarse glass powder foams sintered at 750 °C (381 kg m⁻³) had an average compressive strength of 2.2 MPa, which was fallen on the lower range of compressive strengths of previous studies foam glass. Present geopolymer foam samples showed comparable compressive strengths with those of previously studied foams. The thermal conductivity of geopolymer (447 kg m⁻³) and sintered geopolymer foams (368 kg m⁻³) was also comparable with previous studies and 0.11 and 0.078 W m⁻¹K⁻¹, respectively.

9.1 Recommendations of Future Studies

- 1) The Na₂SiO₃/NaOH ratio kept constant, 2.5. The effect of this ratio and NaOH amount on the expansion behaviour, mechanical and physical properties should be investigated as future study.
- 2) Although it was known that there were different sizes and shapes of pores in the geopolymer foam, the average pore size measurement was not made. In addition, the effects of pore size on the mechanical and physical properties and control of this size should be investigated in future studies.

- 3) Industrial type of aluminum powder was used as a foaming agent and an alumina source in this study. However, using secondary aluminum powder as a foaming agent and an alumina source should be examined in the future.
- 4) Although it was known that there was hydrogen gas releasing while producing the geopolymer foam, the amount of hydrogen gas released was not measured. In future studies, the amount of hydrogen gas released should be determined to learn how much damage to the environment.



REFERENCES

1. Abdollahnejad, Z.; Pacheco-Torgal, F.; Félix, T.; Tahri, W.; Barroso Aguiar, J., Mix design, properties and cost analysis of fly ash-based geopolymer foam. *Construction and Building Materials* **2015**, *80*, 18-30.
2. Novais, R. M.; Ascensão, G.; Ferreira, N.; Seabra, M. P.; Labrincha, J. A., Influence of water and aluminium powder content on the properties of waste-containing geopolymer foams. *Ceramics International* **2018**, *44* (6), 6242-6249.
3. Zhang, Z.; Provis, J. L.; Reid, A.; Wang, H., Geopolymer foam concrete: An emerging material for sustainable construction. *Construction and Building Materials* **2014**, *56*, 113-127.
4. Masi, G.; Rickard, W. D. A.; Vickers, L.; Bignozzi, M. C.; van Riessen, A., A comparison between different foaming methods for the synthesis of light weight geopolymers. *Ceramics International* **2014**, *40* (9, Part A), 13891-13902.
5. Aleem, M. I. A.; Arumairaj, P. D., Geopolymer Concrete- a Review. *International Journal of Engineering Sciences & Emerging Technologies* **2012**, *1* (2), 118-122.
6. Sanjayan, J. G.; Nazari, A.; Chen, L.; Nguyen, G. H., Physical and mechanical properties of lightweight aerated geopolymer. *Construction and Building Materials* **2015**, *79*, 236-244.
7. Kastiukas, G.; Zhou, X.; Wan, K. T.; Castro Gomes, J. J. J. o. M. i. C. E., Lightweight Alkali-Activated Material from Mining and Glass Waste by Chemical and Physical Foaming. **2018**, *31* (3), 04018397.
8. Petlitckaia, S.; Poulesquen, A., Design of lightweight metakaolin based geopolymer foamed with hydrogen peroxide. *Ceramics International* **2019**, *45* (1), 1322-1330.
9. Zeren, D.; Şentürk, U.; Güden, M., The expansion behavior of slurries containing recycled glass powder carboxymethyl cellulose, lime and aluminum powder. *Construction and Building Materials* **2020**, *240*, 117898.
10. Long, B. Glass product and method of manufacturing sponge-like glass. 1934.
11. Games, S. Method of making a vitreous material. 1932, 1932.

12. Jones, G. D.; McMillan, W. J.; Williams, C. N., FOAMED GLASS AND VITREOUS SILICA PELLETS. *Industrial & Engineering Chemistry Product Research and Development* **1979**, *18* (1), 64-69.
13. Long, B. Process for the manufacture of multicellular glass. 1938.
14. Ivanov, S. É.; Belyakov, A. V., Diatomite and its applications. *Glass and Ceramics* **2008**, *65* (1), 48-51.
15. Hamid Hojaji, D. M. P. M. B., Theodore Aaron Litovitz Method and composition for making foam glass from diatomaceous earth and fly ash. EP0091473A4, 1981.
16. Wrap, www.wrap.org.uk.
17. Bernardo, E.; Albertini, F., Glass foams from dismantled cathode ray tubes. *Ceramics International* **2006**, *32* (6), 603-608.
18. Petersen, R. R.; König, J.; Smedskjaer, M. M.; Yue, Y., Foaming of CRT panel glass powder using Na₂CO₃. *Glass Technology - European Journal of Glass Science and Technology Part A* **2014**, *55* (1), 1-6.
19. Femandes, H. R.; Tulyaganov, D. U.; Ferreira, J. M. F., Preparation and characterization of foams from sheet glass and fly ash using carbonates as foaming agents. *Ceramics International* **2009**, *35* (1), 229-235.
20. Chen, B.; Luo, Z. W.; Lu, A. X., Preparation of sintered foam glass with high fly ash content. *Materials Letters* **2011**, *65* (23-24), 3555-3558.
21. Chakartnarodom, P.; Ineure, P., Foam Glass Development Using Glass Cullet and Fly Ash or Rice Husk Ash as the Raw Materials. *Key Engineering Materials* **2014**, *608*, 73-78.
22. Fernandes, H. R.; Tulyaganov, D. U.; Ferreira, J. M. F., Production and characterisation of glass ceramic foams from recycled raw materials. *Advances in Applied Ceramics* **2009**, *108* (1), 9-13.
23. Chen, B.; Wang, K. Q.; Chen, X. J.; Lu, A. X., Study of Foam Glass with High Content of Fly Ash Using Calcium Carbonate as Foaming Agent. *Materials Letters* **2012**, *79*, 263-265.
24. Liao, Y. C.; Huang, C. Y., Glass foam from the mixture of reservoir sediment and Na₂CO₃. *Ceramics International* **2012**, *38* (5), 4415-4420.

25. Petersen, R. R.; König, J.; Yue, Y., The mechanism of foaming and thermal conductivity of glasses foamed with MnO₂. *Journal of Non-Crystalline Solids* **2015**, *425*, 74-82.
26. König, J.; Petersen, R. R.; Yue, Y. Z.; Suvorov, D., Gas-releasing reactions in foam-glass formation using carbon and Mn_xO_y as the foaming agents. *Ceramics International* **2017**, *43* (5), 4638-4646.
27. Shutov, A. I.; Yashurkaeva, L. I.; Alekseev, S. V.; Yashurkaev, T. V., Study of the structure of foam glass with different characteristics. *Glass and Ceramics* **2007**, *64* (9-10), 297-299.
28. Garcia-Ten, J.; Saburit, A.; Orts, M. J.; Bernardo, E.; Colombo, P., Glass foams from oxidation/reduction reactions using SiC, Si₃N₄ and AlN powders. *Glass Technology-European Journal of Glass Science and Technology Part A* **2011**, *52* (4), 103-110.
29. Mear, F.; Yot, P.; Ribes, M., Effects of temperature, reaction time and reducing agent content on the synthesis of macroporous foam glasses from waste funnel glasses. *Materials Letters* **2006**, *60* (7), 929-934.
30. Zeren, D. Processing Foam-Like Porous Glass Structure Using A Combined Process Of Glass Powder Expansion In Aqueous Environment And Sintering Process. Izmir Institute of Technology, 2019.
31. Bernardo, E.; Cedro, R.; Florean, M.; Hreglich, S., Reutilization and stabilization of wastes by the production of glass foams. *Ceramics International* **2007**, *33* (6), 963-968.
32. Petersen, R. R.; König, J.; Yue, Y. Z., The viscosity window of the silicate glass foam production. *Journal of Non-Crystalline Solids* **2017**, *456*, 49-54.
33. Spiridonov, Y. A.; Orlova, L. A., Problems of Foam Glass Production. *Glass and Ceramics* **2003**, *60* (9-10), 313-314.
34. Manevich, V. E.; Subbotin, K. Y., Mechanism of foam-glass formation. *Glass and Ceramics* **2008**, *65* (5-6), 154-156.
35. Davidovits, J., GEOPOLYMERS Inorganic polymerie new materials. *Journal of Thermal Analysis and calorimetry* **1991**, *Vol. 37* (1991), 1633-1656.
36. Deventer, J. L. P. a. J. S. J. v., *Geopolymers: Structure, processing, properties and industrial applications*. Woodhead Publishing Limited and CRC Press LLC: Woodhead Publishing Limited, Abington Hall, Granta Park, Great Abington, Cambridge CB21 6AH, UK, 2009.

37. Zhuang, X. Y.; Chen, L.; Komarneni, S.; Zhou, C. H.; Tong, D. S.; Yang, H. M.; Yu, W. H.; Wang, H., Fly ash-based geopolymer: clean production, properties and applications. *Journal of Cleaner Production* **2016**, *125*, 253-267.
38. Xiao, R.; Ma, Y.; Jiang, X.; Zhang, M.; Zhang, Y.; Wang, Y.; Huang, B.; He, Q., Strength, microstructure, efflorescence behavior and environmental impacts of waste glass geopolymers cured at ambient temperature. *Journal of Cleaner Production* **2020**, *252*, 119610.
39. Zhang, P.; Wang, K.; Li, Q.; Wang, J.; Ling, Y., Fabrication and engineering properties of concretes based on geopolymers/alkali-activated binders - A review. *Journal of Cleaner Production* **2020**, *258*, 120896.
40. Nematollahi, B.; Sanjayan, J., Effect of different superplasticizers and activator combinations on workability and strength of fly ash based geopolymer. *Materials & Design* **2014**, *57*, 667-672.
41. Hajimohammadi, A.; van Deventer, J. S. J., Dissolution behaviour of source materials for synthesis of geopolymer binders: A kinetic approach. *International Journal of Mineral Processing* **2016**, *153*, 80-86.
42. Singh, N. B., Foamed geopolymer concrete. *Materials Today: Proceedings* **2018**, *5* (7, Part 2), 15243-15252.
43. Xia, M.; Nematollahi, B.; Sanjayan, J., Printability, accuracy and strength of geopolymer made using powder-based 3D printing for construction applications. *Automation in Construction* **2019**, *101*, 179-189.
44. Ma, G.; Li, Z.; Wang, L.; Bai, G., Micro-cable reinforced geopolymer composite for extrusion-based 3D printing. *Materials Letters* **2019**, *235*, 144-147.
45. Panda, B.; Unluer, C.; Tan, M. J., Investigation of the rheology and strength of geopolymer mixtures for extrusion-based 3D printing. *Cem. Concr. Compos.* **2018**, *94*, 307-314.
46. Novais, R. M.; Ascensão, G.; Seabra, M. P.; Labrincha, J. A., Waste glass from end-of-life fluorescent lamps as raw material in geopolymers. *Waste Management* **2016**, *52*, 245-255.
47. Si, R.; Dai, Q.; Guo, S.; Wang, J., Mechanical property, nanopore structure and drying shrinkage of metakaolin-based geopolymer with waste glass powder. *Journal of Cleaner Production* **2020**, *242*, 118502.

48. Hajimohammadi, A.; Ngo, T.; Mendis, P., How does aluminium foaming agent impact the geopolymer formation mechanism? *Cement and Concrete Composites* **2017**, *80*, 277-286.
49. Hajimohammadi, A.; Ngo, T.; Mendis, P.; Sanjayan, J., Regulating the chemical foaming reaction to control the porosity of geopolymer foams. *Materials & Design* **2017**, *120*, 255-265.
50. Yang, Y.; Jiang, J.; Hou, L.; Lu, Z.; Li, J.; Wang, J., Pore structure and properties of porous geopolymer based on pre-swelled bentonite. *Construction and Building Materials* **2020**, 254.
51. Leiva, C.; Luna-Galiano, Y.; Arenas, C.; Alonso-Fariñas, B.; Fernández-Pereira, C., A porous geopolymer based on aluminum-waste with acoustic properties. *Waste Management* **2019**, *95*, 504-512.
52. Abo Sawan, S. E.; Zawrah, M. F.; Khattab, R. M.; Abdel-Shafi, A. A., In-situ formation of geopolymer foams through addition of silica fume: Preparation and sinterability. *Materials Chemistry and Physics* **2020**, 239.
53. Novais, R. M.; Pullar, R. C.; Labrincha, J. A., Geopolymer foams: An overview of recent advancements. *Progress in Materials Science* **2020**, 109.
54. Wu, J.; Zhang, Z.; Zhang, Y.; Li, D., Preparation and characterization of ultra-lightweight foamed geopolymer (UFG) based on fly ash-metakaolin blends. *Construction and Building Materials* **2018**, *168*, 771-779.
55. Ducman, V.; Korat, L., Characterization of geopolymer fly-ash based foams obtained with the addition of Al powder or H₂O₂ as foaming agents. *Materials Characterization* **2016**, *113*, 207-213.
56. Eliche-Quesada, D.; Ruiz-Molina, S.; Pérez-Villarejo, L.; Castro, E.; Sánchez-Soto, P. J., Dust filter of secondary aluminium industry as raw material of geopolymer foams. *Journal of Building Engineering* **2020**.
57. Singh, N. B. J. M., Fly ash-based geopolymer binder: A future construction material. **2018**, *8* (7), 299.
58. Belitskus, D., Reaction of Aluminum with Sodium Hydroxide Solution as a Source of Hydrogen. *Journal of The Electrochemical Society* **1970**, *117* (8), 1097.
59. Hiraki, T.; Takeuchi, M.; Hisa, M.; Akiyama, T., Hydrogen production from waste aluminum at different temperatures, with LCA. *Materials Transactions* **2005**, *46* (5), 1052-1057.

60. Martínez, S. S.; López Benítez, W.; Álvarez Gallegos, A. A.; Sebastián, P. J., Recycling of aluminum to produce green energy. *Solar Energy Materials and Solar Cells* **2005**, *88* (2), 237-243.
61. Bai, C.; Li, H.; Bernardo, E.; Colombo, P., Waste-to-resource preparation of glass-containing foams from geopolymers. *Ceramics International* **2019**, *45* (6), 7196-7202.
62. Senff, L.; Novais, R. M.; Carvalheiras, J.; Labrincha, J. A., Eco-friendly approach to enhance the mechanical performance of geopolymer foams: Using glass fibre waste coming from wind blade production. *Construction and Building Materials* **2020**, 239.
63. Attila, Y.; Guden, M.; Tasdemirci, A., Foam glass processing using a polishing glass powder residue. *Ceramics International* **2013**, *39* (5), 5869-5877.
64. Andersen, E. R.; Andersen, E. J., Method for producing hydrogen. Google Patents: 2003.
65. Koerner, C., Physics of Foaming. In *Integral Foam Molding of Light Metals*, Springer Berlin Heidelberg: 2008; pp 77-102.
66. Daoud, A., Effect of fly ash addition on the structure and compressive properties of 4032-fly ash particle composite foams. *Journal of Alloys and Compounds* **2009**, *487* (1), 618-625.
67. Bergstrom, L., *Surface and Colloid Chemistry in Advanced Ceramics Processing*. CRC Press: 2017.
68. Konijn, B. J.; Sanderink, O. B. J.; Kruyt, N. P., Experimental study of the viscosity of suspensions: Effect of solid fraction, particle size and suspending liquid. *Powder Technology* **2014**, *266*, 61-69.
69. Deng, Z.-Y.; Ferreira, J. M. F.; Sakka, Y., Hydrogen-Generation Materials for Portable Applications. *J. Am. Ceram. Soc.* **2008**, *91* (12), 3825-3834.
70. Kroezen, A. B. J.; Wassink, J. G.; Schipper, C. A. C., The flow properties of foam. **1988**, *104* (10), 393-400.
71. Hilgenfeldt, S.; Koehler, S. A.; Stone, H. A., Dynamics of Coarsening Foams: Accelerated and Self-Limiting Drainage. *Physical Review Letters* **2001**, *86* (20), 4704-4707.
72. Niu, Y.-H.; Fan, X.-Y.; Ren, D.; Wang, W.; Li, Y.; Yang, Z.; Cui, L., Effect of Na₂CO₃ content on thermal properties of foam-glass ceramics prepared from smelting slag. *Materials Chemistry and Physics* **2020**, *256*, 123610.

73. Gibson, L. J.; Ashby, M. F., *Cellular Solids: Structure and Properties*. 2 ed.; Cambridge University Press: Cambridge, 1997.
74. Dembovska, L.; Bajare, D.; Ducman, V.; Korat, L.; Bumanis, G., The use of different by-products in the production of lightweight alkali activated building materials. *Construction and Building Materials* **2017**, *135*, 315-322.
75. Zhang, Z.; Provis, J. L.; Reid, A.; Wang, H., Mechanical, thermal insulation, thermal resistance and acoustic absorption properties of geopolymer foam concrete. *Cement and Concrete Composites* **2015**, *62*, 97-105.
76. Liu, M. Y. J.; Alengaram, U. J.; Jumaat, M. Z.; Mo, K. H., Evaluation of thermal conductivity, mechanical and transport properties of lightweight aggregate foamed geopolymer concrete. *Energy and Buildings* **2014**, *72*, 238-245.
77. Kastiukas, G.; Zhou, X.; Wan, K. T.; Castro Gomes, J. J. J. o. M. i. C. E., Lightweight Alkali-Activated Material from Mining and Glass Waste by Chemical and Physical Foaming. **2019**, *31* (3), 04018397.
78. Novais, R. M.; Ascensão, G.; Buruberri, L. H.; Senff, L.; Labrincha, J. A., Influence of blowing agent on the fresh- and hardened-state properties of lightweight geopolymers. *Materials & Design* **2016**, *108*, 551-559.
79. Novais, R. M.; Buruberri, L. H.; Ascensão, G.; Seabra, M. P.; Labrincha, J. A., Porous biomass fly ash-based geopolymers with tailored thermal conductivity. *Journal of Cleaner Production* **2016**, *119*, 99-107.
80. Vaou, V.; Pantias, D., Thermal insulating foamy geopolymers from perlite. *Minerals Engineering* **2010**, *23* (14), 1146-1151.
81. Cui, Y.; Wang, D.; Zhao, J.; Li, D.; Ng, S.; Rui, Y., Effect of calcium stearate based foam stabilizer on pore characteristics and thermal conductivity of geopolymer foam material. *Journal of Building Engineering* **2018**, *20*, 21-29.
82. Feng, J.; Zhang, R.; Gong, L.; Li, Y.; Cao, W.; Cheng, X. J. M.; Design, Development of porous fly ash-based geopolymer with low thermal conductivity. **2015**, *65*, 529-533.
83. Bai, C.; Ni, T.; Wang, Q.; Li, H.; Colombo, P., Porosity, mechanical and insulating properties of geopolymer foams using vegetable oil as the stabilizing agent. *Journal of the European Ceramic Society* **2018**, *38* (2), 799-805.
84. Xu, F.; Gu, G.; Zhang, W.; Wang, H.; Huang, X.; Zhu, J., Pore structure analysis and properties evaluations of fly ash-based geopolymer foams by chemical foaming method. *Ceramics International* **2018**, *44* (16), 19989-19997.

85. Wu, J. P.; Boccaccini, A. R.; Lee, P. D.; Kershaw, M. J.; Rawlings, R. D., Glass ceramic foams from coal ash and waste glass: production and characterisation. *Advances in Applied Ceramics* **2006**, *105* (1), 32-39.
86. Llaudis, A. S.; Tari, M. J. O.; Ten, F. J. G.; Bernardo, E.; Colombo, P., Foaming of flat glass cullet using Si₃N₄ and MnO₂ powders. *Ceramics International* **2009**, *35* (5), 1953-1959.
87. Shutov, A. I.; Yashurkaeva, L. I.; Alekseev, S. V.; Yashurkaev, T. V., Modeling of the structure of heat-insulating foam glass. *Glass and Ceramics* **2007**, *64* (11-12), 397-399.
88. Kaz'mina, O. V.; Vereshchagin, V. I.; Abiyaka, A. N., PROSPECTS FOR USE OF FINELY DISPERSE QUARTZ SANDS IN PRODUCTION OF FOAM-GLASS CRYSTALLINE MATERIALS. *Glass and Ceramics* **2008**, *65* (9-10), 319-321.
89. Kaz'mina, O. V.; Vereshchagin, V. I.; Abiyaka, A. N., Assessment of the compositions and components for obtaining foam-glass-crystalline materials from aluminosilicate initial materials. *Glass and Ceramics* **2009**, *66* (3-4), 82-85.
90. Bernardo, E.; Scarinci, G.; Bertuzzi, P.; Ercole, P.; Ramon, L., Recycling of waste glasses into partially crystallized glass foams. *Journal of Porous Materials* **2010**, *17* (3), 359-365.
91. Garkavi, M. S.; Mel'chaeva, O. K.; Nazarova, A. I., EFFECT OF THE PROCESS PARAMETERS OF MIX PREPARATION ON THE PROPERTIES OF FOAM GLASS. *Glass and Ceramics* **2011**, *68* (1-2), 44-46.
92. Bai, J. G.; Yang, X. H.; Xu, S. C.; Jing, W. J.; Yang, J. F., Preparation of foam glass from waste glass and fly ash. *Materials Letters* **2014**, *136*, 52-54.
93. Bian, J. L.; Cao, W. L.; Yang, L.; Xiong, C. Q., Experimental Research on the Mechanical Properties of Tailing Microcrystalline Foam Glass. *Materials* **2018**, *11* (10), 19.
94. Xi, C. P.; Zheng, F.; Xu, J. H.; Yang, W. G.; Peng, Y. Q.; Li, Y.; Li, P.; Zhen, Q.; Bashir, S.; Liu, J. L., Preparation of glass-ceramic foams using extracted titanium tailing and glass waste as raw materials. *Construction and Building Materials* **2018**, *190*, 896-909.
95. Semukhin, B. S.; Kazmina, O. V.; Volkova, A. Y.; Suslyayev, V. I., Physical Characteristics of Foam Glass Modified with Zirconium Dioxide. *Russ. Phys. J.* **2017**, *59* (12), 2130-2136.

96. Huo, W. L.; Yan, S.; Wu, J. M.; Liu, J. J.; Chen, Y. G.; Qu, Y. N.; Tang, X. Y.; Yang, J. L., A novel fabrication method for glass foams with small pore size and controllable pore structure. *J. Am. Ceram. Soc.* **2017**, *100* (12), 5502-5511.
97. Mear, F.; Yot, P.; Viennois, R.; Ribes, M., Mechanical behaviour and thermal and electrical properties of foam glass. *Ceramics International* **2007**, *33* (4), 543-550.
98. Bobkova, N. M.; Barantseva, S. E.; Trusova, E. E., Production of foam glass with granite siftings from the Mikashevichi deposit. *Glass and Ceramics* **2007**, *64* (1), 47-50.
99. König, J.; Petersen, R. R.; Iversen, N.; Yue, Y., Suppressing the effect of cullet composition on the formation and properties of foamed glass. *Ceramics International* **2018**, *44* (10), 11143-11150.
100. Torres-Carrasco, M.; Palomo, J. G.; Puertas, F., Sodium silicate solutions from dissolution of glasswastes. Statistical analysis. *Materiales de Construcción* **2014**, *64* (314).
101. Finocchiaro, C.; Barone, G.; Mazzoleni, P.; Leonelli, C.; Gharzouni, A.; Rossignol, S., FT-IR study of early stages of alkali activated materials based on pyroclastic deposits (Mt. Etna, Sicily, Italy) using two different alkaline solutions. *Construction and Building Materials* **2020**, *262*, 120095.